Diplomarbeit

Masterthesis

Electron scattering in graphene by accurately modeled lattice defects

Lukas Linhart

supervised by
Dr. Florian Libisch
Prof. Dr. Joachim Burgdörfer

Institute for Theoretical Physics

November 16, 2016

Contents

Abstract

Defects strongly influence the electronic properties of graphene. It is of importance to get a deeper insight into the influence that defects have on electron transport. In this work we accurately model defect structures with density functional theory. We obtain tight-binding parameters via transforming the results into the basis of maximally localized Wannier orbitals. We can then treat large-scale structures with defects using a highly efficient tight-binding approach. To combine the defect structure calculations with the surrounding lattice, we present a new embedding technique that is applicable to a wide range of zero-dimensional defects. This technique defines a transition region between the tight-binding parameters of the bulk lattice and those obtained for the defect structure. To test our technique we model an experimental setup currently investigated at the University of Vienna.

Our approach turns out to be applicable to a broad range of defects. Calculations were conducted for Stone-Wales defects, flower defects, double vacancies and silicon substitutes. The scattering at these defects could be investigated in detail for a wide range of energies. We find robust backscattering signatures of the defect symmetries that can be explained by the band structure of graphene.

v

1   Introduction

The first discovery of graphene by Novoselov and Geim in 2004 [1] opened a new field of physics, the field of 2D materials. The past twelve years of ever growing intense research have led to a profound understanding of the extraordinary properties of graphene [2]. Graphene consists of a single layer of carbon atoms arranged in a hexagonal honeycomb lattice with properties such as the manifestation of an anomalous quantum Hall effect, extremely high electron mobility, extraordinary mechanical strength and extreme thinness being just the most prominent [2, 3]. Of special interest is the nearly linear band structure of graphene around the Fermi energy. In this range the band structure mimics a relativistic dispersion that can be described by the Dirac equation for massless particles.

The good theoretical understanding and the progress made in graphene synthesis and processing have led to a development stage where application ready graphene based devices are within reach [4]. Possible new devices based on graphene cover a broad range from spintronics [5] and highly accurate sensors to terahertz clocked field effect transistors or stacked 2D material photovoltaics [6].

To further push the development of such devices and to be able to think of other new applications, an even better theoretical understanding of graphene is of critical importance. The change in properties of graphene due to imperfections is crucial for the performance and functionality of future devices and therefore the understanding of such changes is a keystone in the path towards graphene based devices.

While graphene in general is of high crystalline purity every real lattice in a real device intrinsically features imperfections due to defects and the finite size of the lattice. Defects as well as boundary effects can strongly affect the extraordinary properties of graphene. A variety of defect structures were already observed and also theoretically predicted, eg. topological defects (Stone-Wales and flower defects) [7, 8, 10, 15, 11, 12, 13, 14, 15, 16]. In this thesis we are searching for new ways to describe changes in transport properties when introducing such defects into a large lattice structure.

As density functional theory (DFT) and other highly accurate methods are not directly applicable to mesoscopic systems, a simpler approach demanding less computational effort is chosen: the tight-binding method. To simulate defects we combine DFT and tight-binding calculations. This is done by first calculating a supercell containing one defect via DFT which is then embedded into a large lattice described by tight-binding. A technique of embedding these rather small structures calculated by DFT into the large tight-binding lattice is developed and tested on a variety of defects.

In the first chapter we revisit some theoretical background. We then discuss the properties of graphene and how we include them in our calculations in chapter two. In the third chapter we argue why an embedding technique has to be used, how we realize it and what limitations for this technique exist. The following chapter discusses the DFT calculations of the embedded structures and in the last chapter we test and apply the embedding technique to a structure that resembles an experimental setup currently performed at the University of Vienna [17].

2 Concepts

In this section we introduce the main concepts used for developing the results of this master's thesis. Due to the wide range and relative complexity of some of the concepts we only provide an overview. For a detailed discussion please see the corresponding references.

2.1 Density Functional Theory (DFT)

Solving the quantum mechanical many body problem analytically is an impossible task already for as few as three electrons. Even direct numerical approaches fail, due to the factorial scaling of the problem with the number of electrons. Quantum mechanically treating many-electron systems requires approximations. A very common example is the Hartree-Fock-approximation where the key idea is to approximate the electron-electron interaction by a mean field.

In 1998 Walter Kohn, an Austrian born American physicist received the Nobel prize in chemistry for developing the - up to today - most popular method, Density Functional Theory (DFT) [18].

The foundation of DFT are the Hohenberg-Kohn-Sham-theorems.

- For any system of interacting particles in an external potential the ground state density is uniquely determined.
- A universal functional for the energy can be defined in terms of the density. The exact ground state is the global minimum of this functional. [18]

Given these theorems, how can we find the functional for an atomistic system and how can we minimize it regarding its energy? Starting from the many-electron time-independent Schrödinger equation

$$\left[\hat{T} + \hat{V}_{\text{ext.}} + \hat{V}_{e-e} \right] |\Psi\rangle = E|\Psi\rangle \tag{1}$$

the individual terms of the Hamiltonian need to be expressed as a functional of the electron density. V_{e-e} represents the electron-electron interaction and can be expressed as

$$V_{e-e}[n(\mathbf{r})] = \frac{e^2}{2} \int \int \frac{n(\mathbf{r})n(\mathbf{r'})}{|\mathbf{r} - \mathbf{r'}|} d\mathbf{r} d\mathbf{r'} + U_{\text{xc}}[n(\mathbf{r})] \tag{2}$$

In Equation (2) the first term on the right side accounts for Coulomb repulsion while the second term U_{xc} represents the exchange and correlation term discussed below. $V_{\text{ext.}}$ denotes the external potential due to the atomic nuclei and is easily expressed in terms of the electron density

$$V_{\text{ext.}}[n(\mathbf{r})] = \int n(\mathbf{r})V_{\text{ext}}(\mathbf{R})d\mathbf{r}. \tag{3}$$

The $\mathbf{R}$ are the fixed ionic positions in Born-Oppenheimer approximation. The kinetic energy term can be expressed as

$$T[n(\mathbf{r})] = T_0[n(\mathbf{r})] + T_{\text{corr}}[n(\mathbf{r})] \tag{4}$$

where T_0 represents the kinetic energy of non-interacting electrons and T_{corr} stands for the corrections due to interaction of the electrons.

After identifying all parts of the functional we arrive at

$$E[n(\mathbf{r})] = V_{ext.}[n(\mathbf{r})] + V_H[n(\mathbf{r})] + T_0[n(\mathbf{r})] + \overbrace{T_{corr}[n(\mathbf{r})] + U_{exc}[n(\mathbf{r})]}^{E_{xc}}. \tag{5}$$

The only part that remains to be expressed, to be able to fully write down the energy functional in terms of the density, is the so-called exchange correlation functional $E_{xc}[n(\mathbf{r})]$.

This functional should compensate for the error included in the calculation of the kinetic energy and the electron-electron interaction. How to choose this functional turns out to be the core challenge in applying DFT. The most common approaches are the local density approximation (LDA) and generalized gradient approximation (GGA). The most intuitive approach, the local density approximation, models the exchange correlation functional via:

$$E_{xc}^{LDA}[n] \quad = \quad E_x^{LDA}[n] + E_c^{LDA}[n] \tag{6}$$

$$E_x^{LDA}[n(r)] \quad = \quad -\frac{3}{4}\left(\frac{3}{\pi}\right)^{\frac{1}{3}} \int n(r)^{\frac{4}{3}} dr \tag{7}$$

$$E_c^{LDA}[n(r)] \quad = \quad \int n(r) \cdot a \cdot \ln\left(1 + \frac{b}{r_s} + \frac{b}{r_s^2}\right) dr \tag{8}$$

$E_x^{LDA}[n]$ is the exchange functional, the integral over the approximated exchange energy density, given by the Dirac exchange energy density for a homogeneous electron gas. The $E_c^{LDA}[n]$ is the correlation functional, fitted to Monte Carlo simulations, by a fit function with fitting parameters a,b and r_s just recently derived [19] (For details see [20]).

With the energy functional at hand, one now has to search for the electron density that minimizes the energy such that,

$$\left.\frac{\delta E[n]}{\delta n}\right|_{n=n_0} = 0. \tag{9}$$

This can only be done iteratively and implies - for larger systems (50-200 atoms) - a high computational effort, as a self consistent matrix equation has to be solved. This limits the applicability of DFT for large systems.

Although DFT works remarkably well for many systems there are some limitations [20] most prominently the treatment of Van der Waals interactions.

One extension of DFT used in this master's thesis is to apply the Hellmann-Feynman theorem which enables calculating the forces acting on the ionic sites starting from the ground state [20]. By iteratively moving the atoms from a starting position according to the calculated forces from each ground state electron density associated with the current ionic positions one can find the relaxed and stable atomic structure.

DFT is considered an ab-initio method which means no additional parameters from previous calculations are needed to apply the method to a new system. Although some might argue that the exchange correlation potential needs to be fitted and DFT cannot be considered an ab-initio method.

2.2 Maximally Localized Wannier Functions (MLW.F)

A set of Bloch functions used in solid state physics can be transformed into a set of localized wavefunctions via the Fourier-type transformation

$$\Psi_{n,\mathbf{R}}(\mathbf{r}) = \frac{V}{(2\pi)^3} \int_{BZ} \sum_m U_{nm} e^{i\mathbf{R}\mathbf{k}} \Phi_m(\mathbf{k}) d\mathbf{k}. \qquad [21, \ 22] \qquad (10)$$

The Ψ are called Wannier functions for a suitable U_{nm}. The Wannier function $\Psi_{n,\mathbf{R}}(\mathbf{r})$ is localized around lattice side $\mathbf{R}$ and can be associated with band n. $\Phi_m(\mathbf{i})$ are the standard Bloch functions in a periodic potential. U is a unitary matrix and contributes to the gauge freedom that comes with independently chosen phases of each Bloch function. Due to the unitarity of the transformation in Equation (10), the Wannier functions are orthogonal to each other and span the same space as the Bloch states, i.e. no information on the system is lost.

The gauge degree of freedom in U causes the Wannier functions to be not uniquely defined. Depending on which matrix U is chosen, the localization "quality" varies [22]. Although different localization criteria can be defined a very widely used criterion was developed by Mazari and Vanderbilt [22, 23]. It involves the minimization of the sum of the quadratic spread,

$$\Omega = \sum_n [\langle r_n^2 \rangle - \bar{\mathbf{r}}_n^2] = \sum_n [\langle \mathbf{0}n|r_n^2|\mathbf{0}n \rangle - \langle \mathbf{0}n|r_n|\mathbf{0}n \rangle^2]. \qquad (11)$$

Where $|\mathbf{0}n\rangle$ refers to the Wannier function localized at R = 0 and associated with band n.

This criterion can be separated into an off-diagonal and a diagonal component,

$$\Omega = \Omega_I + \tilde{\Omega}, \qquad (12)$$

$$\Omega_I = \sum_n \left[\langle r^2 \rangle_n - \sum_{\mathbf{R},m} |\langle |\mathbf{R}m|\mathbf{r}|\mathbf{0}n \rangle|^2 \right], \qquad (13)$$

$$\tilde{\Omega} = \sum_n \sum_{\mathbf{R}m \neq \mathbf{0}n} |\langle |\mathbf{R}m|\mathbf{r}|\mathbf{0}n \rangle|^2. \qquad (14)$$

The reason for this separation is that Ω_I is positive definite and independent of the choice of U. Furthermore it is possible to express the spread function $\tilde{\Omega}$ in k space. By minimizing Ω, one finds the Wannier functions with minimal spread according to the minimization criterion of Equation (11), the so-called Maximally Localized Wannier Functions (MLWF) [23].

2.2.1 Disentanglement:

Usually only a small subset of orbitals in an atomic structure contribute significantly to electronic properties such as transport. Therefore only a small number of bands and therefore Bloch states need to be considered in the calculation, but ab initio methods, such as described in Section 2.1, usually deliver a full set of Bloch states (up to a

certain cut-off energy). Great care has to be taken which Bloch states should be used in the transformation of Equation (10).

When the relevant energy bands are well separated from other bands by an energy gap over the full Brillouin zone, the choice of bands and Bloch states is rather straight forward. The bands are said to be not entangled. By contrast if relevant bands are entangled with other bands meaning that relevant energy bands and non relevant bands intersect somewhere in the Brillouin zone a so-called disentanglement procedure has to be used. The aim of this disentanglement procedure is to find the set of relevant bands N out of a set of $N_k \geq N$ bands that reach inside a certain energy window at a point k. At every point $\mathbf{k}$ the N_k bands span a N_k dimensional space $\mathcal{S}(k)$ and one can define a number of sub spaces $\mathcal{F}(k) \subseteq \mathcal{S}(k)$ with dimension N. Therefore we have to find the subspace $\mathcal{F}(k)$ that minimizes the spread function Ω. Since Ω_I is independent of the choice of U and $\tilde{\Omega}$ is positive semi definite one can obtain the relevant set of Bloch states by minimizing Ω_I under variation of the subsets $\mathcal{F}$ [24].

The remaining difficulty is finding a good starting guess for the Wannier orbitals on which the Bloch functions can be projected. This is usually achieved by choosing atomic orbitals of the outer shell of the corresponding free atoms [24].

2.3   Tight-binding Method

Tight-binding is a method to efficiently calculate properties of large scale nanodevices (with fast computers, in our days, up to 10^7 atoms). The approach is widely used for many different problems, even though its assumptions are a crude simplification of the real lattice.

The main assumptions are:

- The dynamics of the nuclei can be neglected like in almost all electronic structure method. This follows by looking at the adiabatic theorem (Born-Oppenheimer-approximation), which can be applied due to the much greater mass of the nuclei compared to the electrons.

- The electrons are tightly bound to the nuclei meaning the electron wavefunctions are strong localized around the nuclei. Here lies the origin of the term "tight-binding". This assumption is valid for low energies forming a main restriction of the method.

- Tight-binding is a single particle model where electron-electron interactions are included as in a meanfield effective potential V_{eff}.

With these assumptions we can choose the basis of our lattice to be the orbitals of all atoms relevant for transport. This approach is called linear combination of atomic orbitals (LCAO), as every state can be represented is linear combination of atomic orbitals where i runs over all atomic orbitals.

Our single electron Hamiltonian reads

$$H_{\text{se}} = \sum_{l,n,i} H_{\text{atm,i}}(\mathbf{r} + \mathbf{R}_{l,n}) + V_{\text{eff}}(\mathbf{r}), \tag{15}$$

where $\mathbf{H}_{\mathrm{atm}}$ is the Hamiltonian for an electron in the valence band of a free atom and the $R_{l,n} = l\mathbf{a}_1 + n\mathbf{a}_2$ are spatial shifts by full unit cells and V_{eff} represents the effective lattice potential. This potential can be understood as a mean-field approximation of electron-electron coupling and external potential contributions.

With the assumption of tightly bound electrons, the orbitals of all atoms in the lattice form a basis set for electrons with an energy around the Fermi energy. Orbitals with low and high energy compared to the Fermi level are neglected as electrons in low energy orbitals do not contribute to transport and high energy orbitals are very unprobable to be occupied. The strong localization around the atomic nuclei implies that the overlap with orbitals of neighboring atoms is small. In the following we will refer to this basis as tight-binding basis. The basis is not a complete basis as the orbitals that do not contribute to transport are dropped.

A state can be expanded as

$$|\Psi\rangle = \sum_n c_n |\phi_n\rangle. \tag{16}$$

where $|\phi_n\rangle$ represents one localized orbital site n. Representing the Schrödinger equation in the LCAO basis and applying basis elements from the left yields a matrix eigenvalue problem of the form

$$\sum_n \langle \phi_m | H_{\mathrm{se}} | \phi_n \rangle c_n = E \sum_n c_n \langle \phi_m | \phi_n \rangle \qquad \Rightarrow \qquad H\mathbf{c} = E\mathbf{c}. \tag{17}$$

In Equation (17) H is the matrix representation of the Hamiltonian in LCAO basis. One can distinguish between diagonal and off-diagonal elements

$$\epsilon_i \quad = H_{i,i} = \langle \phi_i | H_{\mathrm{se}} | \phi_i \rangle \tag{18}$$

$$\gamma_{i,j} \quad = H_{i,j} = \langle \phi_i | H_{\mathrm{se}} | \phi_j \rangle \tag{19}$$

The diagonal elements ϵ_i are the part of the Hamiltonian that describes energy contributions on a given site, from e.g. potentials or the kinetic energy. They are referred to as on-site energies. The $\gamma_{i,j}$ contribute to interaction between orbital i and orbital j, i.e. the amplitude for coupling between orbital i and orbital j.

Since the overlap of LCAO basis elements is small for atomic lattice sites far apart the coupling parameter $\gamma_{i,j}$ for distant sites is small and is usually dropped to reduce computational effort. An approximation where all interaction parameters beyond the nth nearest neighbors are dropped, is called n^{th} nearest neighbor approximation.

2.3.1 Band structure calculations

The band structure evaluated along a high symmetric path on a single reciprocal unit cell of a lattice, is of special interest. This band structure characterizes all properties of the electron wavefunction within the lattice. How can the band structure be obtained from the Schrödinger equation in the tight-binding model?

Considering that every LCAO orbital in a solid fulfills the Bloch condition for unit cell translations the elements of the LCAO basis can be renumbered

$$|\phi_i\rangle \rightarrow |\phi_{n,l,i}\rangle. \tag{20}$$

$|\phi_{n,l,i}\rangle$ is the i$^{\text{th}}$ LCAO orbital of a unit cell shifted by $\mathbf{R}_{l,n}$ from an arbitrarily chosen origin. Every orbital in the solid can be expressed via an orbital in the unit cell at the origin by the Bloch relation

$$|\phi_{n,l,i}\rangle = e^{i\mathbf{k}\cdot\mathbf{R}_{n,l}}|\phi_{0,0,i}\rangle. \tag{21}$$

When looking at the Schrödinger equation in Equation (17) we find

$$\sum_{n,l,i} H_{(n,l,i),(0,0,j)}|\phi_{n,l,i}\rangle = E|\phi_{0,0,j}\rangle \tag{22}$$

$$\Leftrightarrow \sum_{n,l,i} H_{i,j}e^{i\mathbf{k}\cdot R_{n,l}}|\phi_{0,0,i}\rangle = E|\phi_{0,0,j}\rangle. \tag{23}$$

This reduces the evaluation of the band structure to an eigenvalue problem of size P, with P the number of LCAO orbitals in one unit cell.

2.3.2 Tight-binding and MLWF

For certain energy ranges and lattice configurations - when the MLWFs are well localized and orthogonal to each other at one atomic site and energy range - the MLWFs can be used as tight-binding basis. This is valid because MLWFs have the same properties as the LCAO basis. To underline the similarity, we plot a Wannier orbital with the same symmetry as a LCAO p_z orbital (see Figure 1).
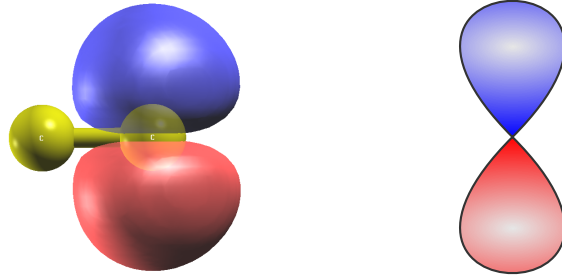

Figure 1: Left: MLWF orbital obtained from graphene DFT calculations located at a carbon atom (yellow structure represents a graphene unit cell). Right: A LCAO p_z orbital, with a comparable localization and the same symmetry.

2.4 Transport in Mesoscopic Systems

Mesoscopic systems (from several tens of atoms to μm solids) are a key research field in modern solid state physics, as they relate quantum mechanical results to macroscopic properties of materials. Especially, modeling electronic transport properties is of mayor interest as semiconductor devices and applications from new materials are meanwhile small enough that quantum effects need to be considered, yet of a size that tight-binding can handle with modern algorithms.

The physics of such systems is very broad. We therefore focus on the most important concepts. For a detailed introduction see [25, 26].

2.4.1 Landauer formula

Transmission probabilities and electronic properties (e.g. the conductance) of a ballistic mesoscopic device can be calculated via the Landauer-Büttiker formalism. In this subsection we want to shortly motivate this formalism.

To model a scattering structure one can think of a geometry consisting of two leads attached to a scattering region as outlined in Figure 2. The expansion of the leads and the scattering region in z direction is so narrow that the system can be viewed as two-dimensional. Electrons in the conduction bands of the leads far away from the scattering region can move freely in x-direction and are restricted to only a few modes M due to the finite width W in y-direction [25],

$$M = \text{int}\left[\frac{2W}{\lambda_F}\right] \tag{24}$$

with λ_F the wavelength at the Fermi energy. Due to the special bandstructure M has to be doubled for graphene.

The electronic wavefunctions can be expressed as plane waves times a transverse function χ

$$\Psi_{\mathbf{k}}(x, y) = Ce^{ikx}\chi(y). \tag{25}$$

The probability for electrons to pass through the device from one lead to the other can be expressed by a transmission probability function $T = |t|^2$. This probability relates to the conductance G via the Landauer formula

$$G = \frac{2e^2}{h} \overbrace{\sum_{i=1}^{M} |t_i|^2}^{\bar{T}}. \tag{26}$$

Equations (24) and (26) give rise to the discrete increase of conductance as energy is increased. Note that Equation (26) does not account for a finite temperature or a larger number of leads attached to the system. Therefore Büttiker expanded the Landauer equation (Equation (26)) to a larger number of attached leads and for finite temperatures. The conductance G between leads p and q at temperature T can be expressed via [25],

$$G_{p,q} = \frac{2e^2}{h} \int \bar{T}_{p,q}(E)\left(-\frac{\partial f_0(T)}{\partial E}\right)dE \tag{27}$$

where $f_0(T)$ it the equilibrium Fermi function.

Equation (27) builds an important step towards understanding Green's functions which will be shortly introduced in the next section and widely used in this thesis.
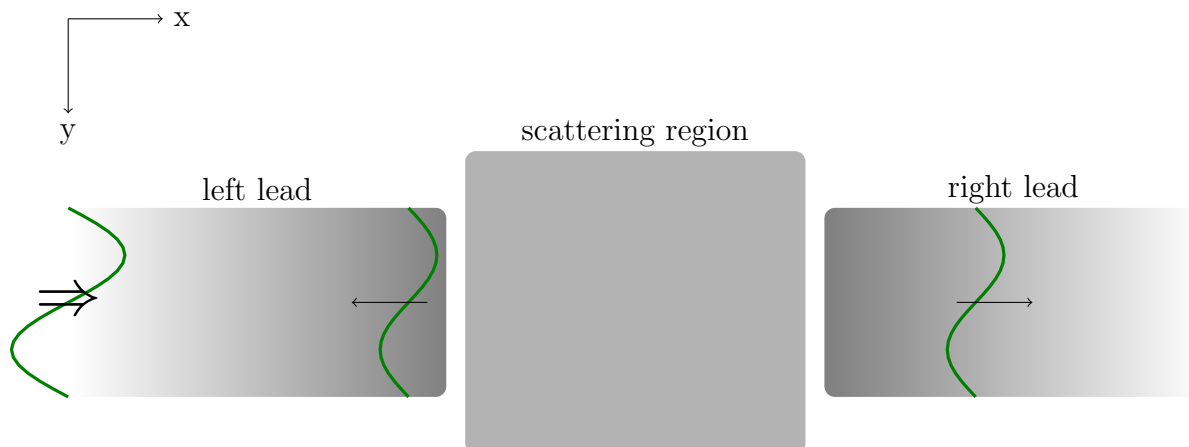
Figure 2: Basic structure of a scattering device. A lead attached at each side, with discrete modes entering the scattering region and either being scattered back to the lead of origin or into any other lead.

2.4.2 Green's function method

The concept of Green's function is used in many fields of physics. In general a Green's function G expresses the response R to any excitation S of a system if the response is related via a differential operator D_{op} [25],

$$D_{op}R = S \Rightarrow R = D_{op}^{-1}S \qquad \text{and} \qquad D_{op}^{-1} = G. \tag{28}$$

In the case of coherent scattering our differential operator is given by $D_{op} = \{E - H\}$, where H is the Hamilton operator of the system. When calculating the conductance by Equation (26) the excitation term S is an incident wave as defined in Equation (25). However, this is not the only excitation one can think of as will be seen in Section 6. The Green's function can be related to the well known scattering matrix and therefore to the transmission probability via the Fisher-Lee relation [27].

$$S_{jl} = -\delta_{jl} + i\hbar \sqrt{v_l^L v_j^R} \int dy_R \int dy_L \chi_l(y_L) G_{LR}^r(y_L, y_R) \chi_j(y_R) \tag{29}$$

where v_j^R and v_l^L are the group velocities at the leads L and R. With this we can understand the Green's function $G(r, r')$ as a measure for the response at position r for an excitation of the system at position r'.

2.4.3 Using Dyson's equation for appending leads

The Green's function as a direct measure of the response of a system fully describes the scattering problem in coherent transport at the precision of the modeled Hamiltonian.
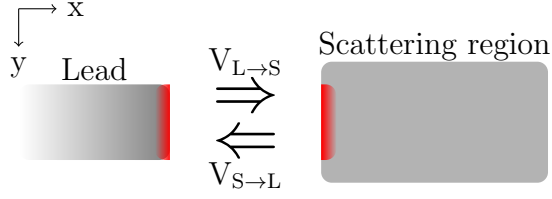
Figure 3: Interaction potential $V_{L \to S}$ ($V_{S \to L}$) between scattering region (S) and lead (L) only act on a small part of the lead.

Calculating the Green's function is a challenging task, as a large matrix inversion has to be done. Moreover, for infinite leads, the Hamiltonian matrix is infinite dimensional making it impossible to calculate. This problem can be overcome via Dyson's equation. In the following we sketch a derivation starting from two separate structures (see Figure 3).

Thinking of a scattering region attached to an infinite lead as shown in Figure 3 the Hamiltonian describing the system can be written as

$$\begin{pmatrix} (H_{L0} - E\mathbb{1}_{\infty,\infty}) & V_{L \leftarrow S} \\ V_{S \leftarrow L} & (H_0 - E\mathbb{1}_{N,N}) \end{pmatrix} \begin{pmatrix} G_L & G_{L \leftarrow S} \\ G_{S \leftarrow L} & G_S \end{pmatrix} = \mathbb{1}_{\infty,\infty}. \tag{30}$$

Here $V_{L \leftarrow S}$ is the interaction between the scattering region and the lead with $V_{L \leftarrow S} = V_{S \leftarrow L}^\dagger$. H_0 is the Hamiltonian of the non-interacting scattering region and H_{L0} is the non-interacting Hamiltonian of the lead. This leads to four equations

$$(H_{L0} - E\mathbb{1}_{\infty,\infty})G_L + V_{L \leftarrow S}G_{S \leftarrow L} = \mathbb{1}_{\infty,\infty} \tag{31}$$

$$V_{L \leftarrow S}^\dagger G_L + (H_0 - E\mathbb{1}_{N,N})G_{S \leftarrow L} = 0 \tag{32}$$

$$(H_{L0} - E\mathbb{1}_{\infty,\infty})G_{L \leftarrow S} + V_{L \leftarrow S}G_S = 0 \tag{33}$$

$$V_{L \leftarrow S}^\dagger G_{L \leftarrow S} + (H_0 - E\mathbb{1}_{N,N})G_S = \mathbb{1}_{N,N} \tag{34}$$

and, after solving for G_S, one arrives at

$$G_S = \left[\overbrace{(H_0 - E\mathbb{1}_{N,N})}^{=G_{S0}^{-1}} - \underbrace{V_{L \leftarrow S}^\dagger \overbrace{(H_L - E\mathbb{1}_{\infty,\infty})^{-1}}^{=G_{L0}} V_{L \leftarrow S}}_{\Sigma_L} \right]^{-1}, \tag{35}$$

which can easily be transformed into the matrix form of a special case of Dyson's equation [25, 26, 31],

$$G_S = G_{S0} + G_{S0}\Sigma_L G_S. \tag{36}$$

This result still contains an infinite-dimensional matrix but this is not a problem because the non-interacting Green's function G_{L0} at the border of the half infinite lead can usually be evaluated analytically. This is done by first calculating the Green's function for the infinite lead and then splitting it up into two half infinite ones [26]. The procedure introduced above is not only valid for connecting half infinite leads with scattering regions but for any non-local perturbation of the system [28, 29, 25].

10

3 Properties of graphene

One must not search for reasons why graphene is a promising research field. It was first observed only a few years ago [1] defining a new class of materials, the so-called 2D materials. Many other 2D materials have followed the discovery (e.g. hexagonal boron-nitrite).
Graphene is a one atom-thin membrane of carbon atoms, where each atom features three covalent in-plane bonds separated by 120 degree angles defining a honeycomb lattice.

3.1 Solid state description

Graphene can be described with 2 atoms per unit cell. The basis vectors are given by [2],

$$\vec{a}_1 = \frac{a}{2} \begin{pmatrix} \sqrt{3} \\ 3 \end{pmatrix} \qquad \vec{a}_2 = \frac{a}{2} \begin{pmatrix} -\sqrt{3} \\ 3 \end{pmatrix} \tag{37}$$

where $a \approx 1.42\text{Å}$ represents the inter atomic distance. The basis in reciprocal space is given by [2],

$$\vec{b}_1 = \frac{2\pi}{3a} \begin{pmatrix} \sqrt{3} \\ 1 \end{pmatrix} \qquad \vec{b}_2 = \frac{2\pi}{3a} \begin{pmatrix} -\sqrt{3} \\ 1 \end{pmatrix}. \tag{38}$$
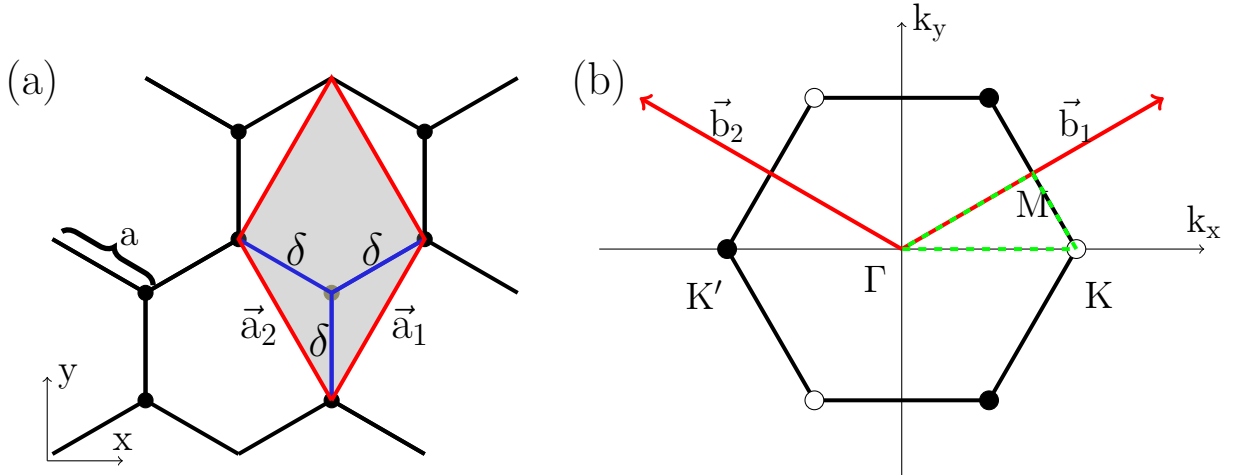
Figure 4: (a) Graphene in real space, the δ 's mark the nearest neighbor interactions. (b) Graphene in reciprocal space with the marked first Brillouin zone and the Dirac points at K and K'. Also the usual high symmetry path alongside which the band structure is evaluated is indicated by the doted green line, along ΓKMΓ.

In a hexagonal honeycomb lattice the carbon atom orbitals p_x^2, p_y^2 and s^2 form sp2-hybridized orbitals (see Figure 4). The p_z^2 orbitals of the lattice atoms form a π band.
The (un)occupied $sp2$ orbitals are energetically much lower (higher) in energy than the π band. They are therefore entirely filled or empty and do not contribute to transport.

On the other hand the π band is composed of half filled p_z orbitals allowing easy hopping from one atom to another and high electron mobility.

The crystalline structure can meanwhile be grown very pure leading to few defects and few lattice scattering events of current-carrying electrons. Electron mobilities measured in graphene flakes have reached $2 \cdot 10^5 \mathrm{cm/s^2}$ even exceeding that of silver [32].

The hexagonal structure of graphene leads to a whole set of interesting properties. The dispersion relation is linear within an energy window of ± 1 eV around the Fermi level (see detailed derivation in the following Section 3.2). Effects that occur due to the quasi relativistic particle behavior and low disorder, such as Klein-tunneling [2] can be observed. Great mechanical strength and the recently described pseudo-magnetic-fields are other examples of the very special properties of graphene [2].

3.2 Linear dispersion relation

In this section we outline the derivation and some consequences of the special band structure of graphene. Assuming low energies (in the range of one eV) transport is dominated by the p_z orbitals which are well localized at the atoms. Therefore a tight-binding approach is appropriate (see Section 2.3).

As only the electron in the p_z orbitals (respectively the electrons in the π band) contribute to transport the number of eigenstates per atom can be reduced to one. Under the constraint of mutually small overlaps these eigenstates are in good approximation orthogonal to each other, defining a proper basis to represent the total tight-binding Hamiltonian of the lattice, as described in Section 2.2 and Section 2.3.

$$\mathrm{H_{TB}^{tot}} = \sum_{\mathrm{i=0}}^{\mathrm{N}} \mathrm{H_{TB}^i} \qquad \text{with} \qquad \mathrm{H_{TB}^i} = \epsilon \left|\phi_\mathrm{i}\right\rangle \left\langle\phi_\mathrm{i}\right| + \sum_\mathrm{j} \gamma_\mathrm{i,j} \left|\phi_\mathrm{j}\right\rangle \left\langle\phi_\mathrm{i}\right|, \qquad (39)$$

where j runs over the neighbors taken into account, ϵ describes the on-site energy, $\gamma_\mathrm{i,j}$ the tight-binding interaction parameters for a certain neighbor coupling and $\left|\phi_\mathrm{i}\right\rangle$ the p_z orbital located at atom i.

Large lattices can be - in good approximation - viewed as infinite. Looking at an arbitrary state in such an infinite lattice,

$$\left|\psi\right\rangle = \sum_\mathrm{i} \mathrm{c_{i,A}} \left|\phi_\mathrm{i,A}\right\rangle + \mathrm{c_{i,B}} \left|\phi_\mathrm{i,B}\right\rangle \qquad (40)$$

where i runs over all unit cells and c_{iA} and c_{iB} are the amplitudes of the state in unit cell i at site A and B. the Hamiltonian is periodic in $\vec{\mathrm{R}}_\mathrm{l,m} = \mathrm{l} \cdot \vec{\mathrm{a}}_1 + \mathrm{m} \cdot \vec{\mathrm{a}}_2$ and thus Bloch's theorem can be applied.

$$\mathrm{H_{TB}^{inf}} \left|\psi\right\rangle = \mathrm{E} \left|\psi\right\rangle \qquad \left\langle \mathrm{r} + \mathrm{R_n} | \psi \right\rangle = \mathrm{e}^{i\vec{\mathrm{k}}\cdot\vec{\mathrm{R}}} \left\langle \mathrm{r} | \psi \right\rangle \qquad (41)$$

With the procedure described in Section 2.3.1 using Bloch's theorem the eigenvalue equation in Equation (41) can be reduced to two dimensions. Including second nearest

neighbors one arrives at [44, 26]

$$H_{TB}^{inf}|\psi\rangle = E|\psi\rangle = \begin{pmatrix} \epsilon + f_2(\vec{k}) & f_1(\vec{k}) \\ f_1(-\vec{k}) & \epsilon + f_2(\vec{k}) \end{pmatrix} \begin{pmatrix} c_A \\ c_B \end{pmatrix} = E \begin{pmatrix} c_A \\ c_B \end{pmatrix}. \tag{42}$$

The $f_{1,2}$ in the above equation refer to all first and second nearest neighbor interaction terms (E.g. $f_1(k) = \gamma_1(e^{i\vec{k}\cdot\delta_1} + e^{i\vec{k}\cdot\delta_2} + e^{i\vec{k}\cdot\delta_3})$, δ's from Figure 4) [26].

The dispersion relation for this eigenvalue problem can also be calculated analytically,

$$E_\pm = \pm\gamma_1\sqrt{3 + f(\vec{k})} - \gamma_2 f(\vec{k}) \qquad f(\vec{k}) = 2\cos(\sqrt{3}k_y a) + 4\cos\left(\frac{\sqrt{3}}{2}k_y a\right)\cos\left(\frac{3}{2}k_x a\right). \tag{43}$$

This dispersion relation is quite special (see Figure 5): around the K and K' points, the dispersion relation has a double-cone like shape, as the valence and conduction band touch each other at a single point. This leads to two conclusions:

- With peaks touching but not overlapping, one cannot expect typical metallic behavior where one half filled band is responsible for the conductance. But also semiconductor-like behavior with spacing between valence- and conductance band cannot be expected.

- With the cone like shape around K and K' points, the energy-momentum relation is linear. This is not expected by classical mechanics where $E_{kin} \propto k^2$ but rather by a relativistic description of a particle with zero mass $E \propto k$. Expanding Equation (43) around K gives [30]

$$E_\pm(q) = \pm v_F|q| + O[(q/K)^2]. \tag{44}$$

$v_F \approx 10^6$m/s is the Fermi velocity of the electrons which can be identified via $v_F = \frac{3\gamma_1 a}{2}$. Replacing the speed of light in the Dirac-equation with the Fermi velocity of the electrons the "new" Dirac-equation describes electronic behavior in graphene for low energies very well.
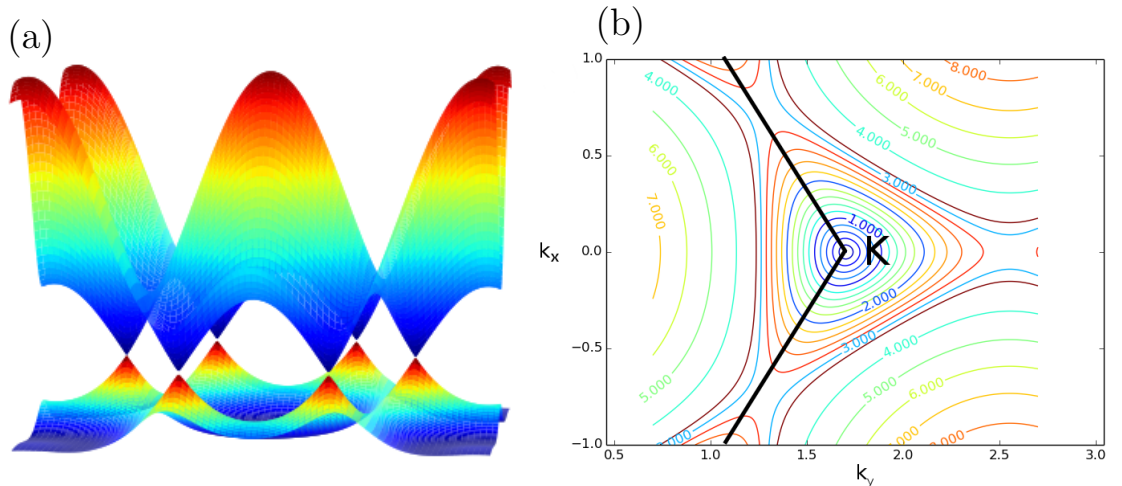
Figure 5: a: Dispersion relation obtained from second NN coupling using $\gamma_1 = 2.7$ eV and $\gamma_2 = -0.2$ eV [2]. b: line plot of Equation (43) trigonal warping around K point. The values indicated on the plots line are in units of eV relative to the Fermi energy.

Up to first order the dispersion relation has no directional dependence. When expanding Equation (43) to second-order one obtains,

$$
E_\pm \approx \pm v_F |q| - \left(\frac{9\gamma_2 a^2}{4} \pm \frac{3\gamma_1 a^2}{8} \sin\left[3\arctan\left(\frac{q_x}{q_y} \right) \right] \right) |q^2|. \tag{45}
$$

An additional direction dependent term leads to a threefold symmetry and the so-called trigonal warping [2]. For energies below $1eV$ the dispersion relation is barely direction dependent, whereas for higher energies, the dependence increases see Figure 5, a).

3.2.1 Simulating a perfect graphene lattice

In the previous section we found that the band structure is linear around the Fermi energy [2, 30]. To simulate graphene by a crude model it therefore would be sufficient to only consider first NN tight-binding parameters reshaping a perfect cone like band structure around the K point (see Figure 6). This crude simulation does not correctly account for the trigonal warping and also reproduces the band structure around the K point poorly. The third NN description is computationally as expensive as the second NN description (as is outlined below) and more accurate. Therefore to simulate a perfect graphene lattice interactions up to third-nearest neighbors are taken into account. With the procedure outlined in Section 2.3.1 and used above one obtains [26]

$$
H_{TB}^{inf}|\psi\rangle = E|\psi\rangle = \begin{pmatrix} \epsilon + f_2(\vec{k}) & f_1(\vec{k}) + f_3(\vec{k}) \\ f_1(-\vec{k}) + f_3(-\vec{k}) & \epsilon + f_2(\vec{k}) \end{pmatrix} \begin{pmatrix} c_A \\ c_B \end{pmatrix} = E \begin{pmatrix} c_A \\ c_B \end{pmatrix}. \tag{46}
$$

By solving this eigenvalue problem a third NN tight-binding approximation of the dispersion relation for an infinite graphene lattice is obtained.

As outlined in Section 2.3, tight-binding is no ab-initio method and the coupling

14

parameters γ_i must be calculated using DFT. This has been done [26, 31] via fitting the band structure obtained from tight-binding to the band structure taken from DFT. The values obtained are,

$$\gamma_1 = 3.145 \text{ eV} \qquad \gamma_2 = -0.042 \text{ eV} \qquad \gamma_3 = 0.35 \text{ eV}. \qquad (47)$$
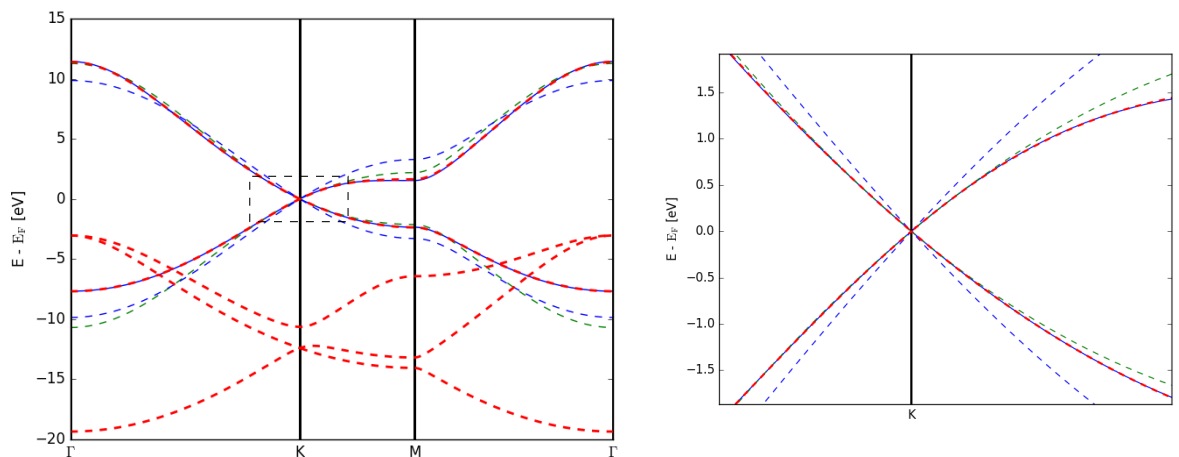
Figure 6: Dispersion relation obtained from ab-initio calculations (dashed red line), with 10th NN coupling (solid red line), with third NN coupling using a parameter set from [31] (dotted green line) and with first NN coupling (dotted blue line).

For energies up to 2 eV, the fitting for third NN shows excellent agreement with the band structure calculated from ab-initio results (see Figure 6). The tight-binding description up to third-nearest neighbors accurately describes transport in perfect bulk graphene at low energies. A detailed discussion can be found in [26].

Numbering the next neighbors
In the following we specify the numbering of the nth nearest neighbor. For a perfect lattice this is straightforward. Starting from the circle with the smallest radius all atoms with the same distance to the corresponding lattice side are numbered in ascending order (see Figure 7).

Advantage of third-nearest neighbor approximation
The possibility to use only third NNs to accurately simulate electron transport in perfect bulk graphene allows calculating the Green's function slice by slice and then join the slices together using Dyson's equation. One can split a perfect graphene zigzag ribbon into parts each consisting of a single slice (see Figure 8). When only third-nearest neighbors are considered, the slices can be added iteratively to the total Green's function via Dyson's equation, similar to the procedure described in Section 2.4.2 [26, 29].
This procedure is not so simple anymore if fourth-nearest neighbors or higher are
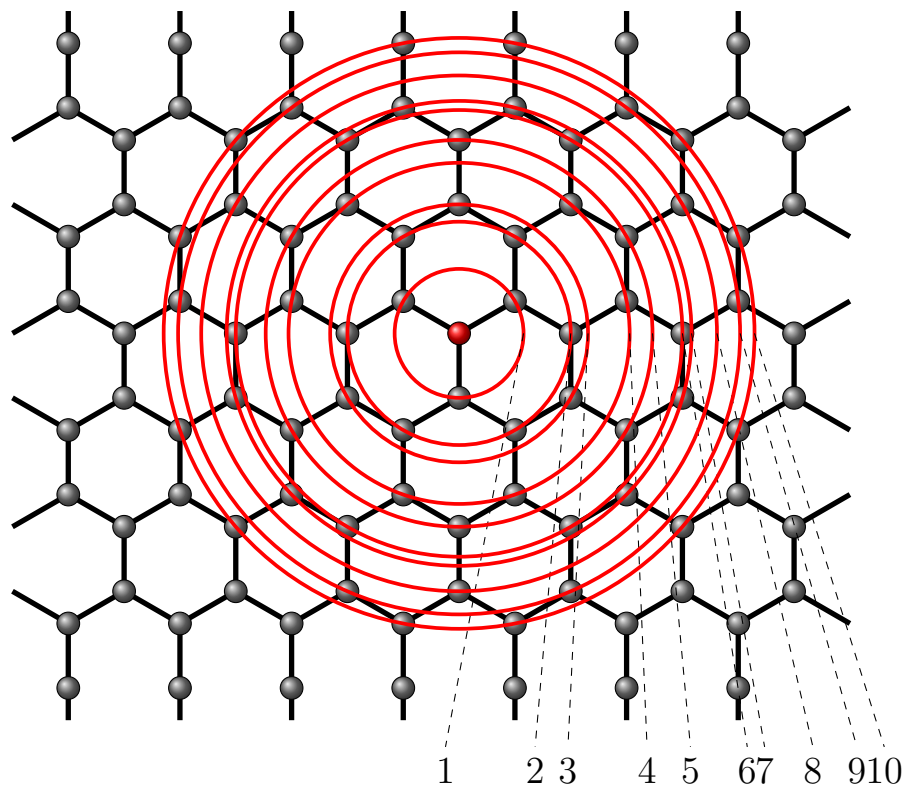
Figure 7: Nearest neighbor numbering in a perfect hexagonal lattice. All atoms on the same red circle share the same next neighbor index to the center atom (marked in red).
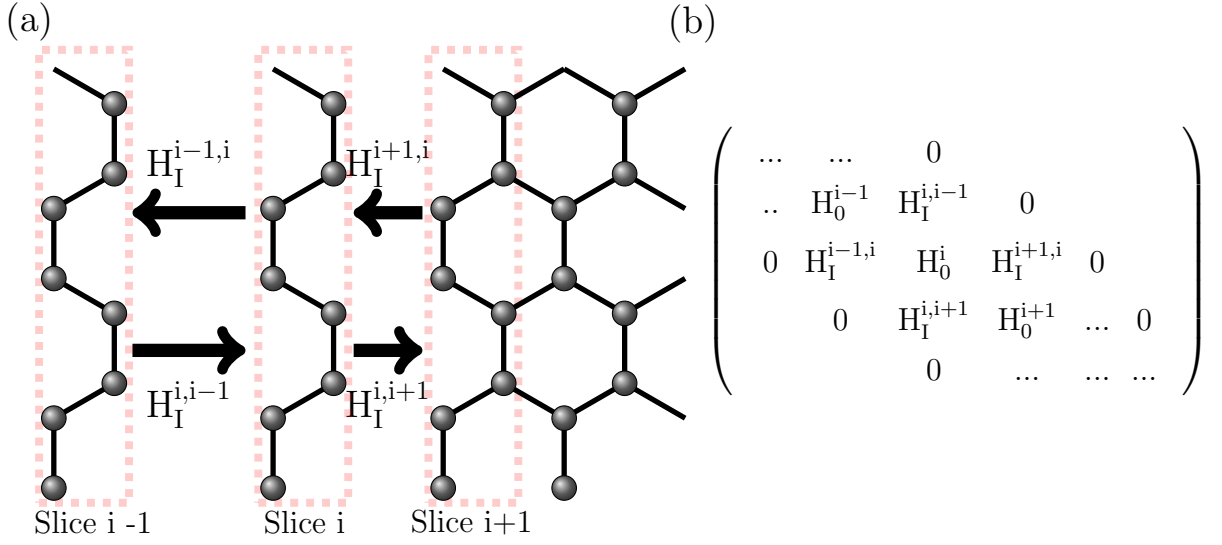
Figure 8: (a) Illustration of how the lattice can be viewed as built up by slices and the interaction potentials between neighboring slices. When considering only third-nearest neighbor coupling all interaction terms between not neighboring slices are dropped and the tight-binding Hamiltonian has the form illustrated in (b).

considered, as the tight-binding Hamiltonian between non neighboring slices becomes nonzero. However a similar approach would be possible by splitting the lattice into pieces of two or more slices each. Considering fourth NN would increase the computational effort to calculate the Green's function for the same geometry by a factor of four. This is because the calculation of the Green's function per slice scales cubically and the number of slices considered will be halved. For eight nearest neighbors each piece would have to consist of three slices increasing the computational effort compared to the third-nearest neighbor approximation by a factor of nine.

3.3 Defect structures

Graphene lattices typically have high crystalline quality and thus feature only very few defects at room temperature [11, 7]. Nevertheless defects have a strong effect on lattice properties, e.g. they weaken the mechanical stability and are a central source of electron scattering [11]. The aim of this master's thesis is to find a method to simulate defect structures in large-scale graphene devices with high accuracy. It is therefore urgent to first characterize the different types of defects.

3.3.1 Characterization of defect structures

Defects in a lattice can roughly be classified according to,

- their dimensionality

- by the number and types of atoms added to or removed from the lattice

- and by the new geometric order caused by these changes.

The listing in this section is not intended to be exhaustive, but rather gives an overview over defects in graphene.

Dimension of defects

As in a bulk material there are **zero-dimensional** defects. Their spatial extension is of the order of one Wigner-Seitz-cell. The most prominent case is just one missing atom, a vacancy [7]. The role of **one-dimensional** defects in a 2D material is already very different to the 3D case, as there is - simply speaking - no easy way around for the electrons. Defects of this kind form a line and can extend over the full width of, e.g. a ribbon. As an example for line like defects consider epitaxially grown graphene where the lattice orientation changes locally due to the method of growth [2]. This leaves grain boundaries between homogeneous local areas [7].

Number and types

Removing atoms leads to **vacancies** while replacing a carbon atom leads to an **impurity**. Adding an atom at a lattice site is called **adsorbate** and rearranging atoms while keeping their number constant results in configurations such as the very prominent Stone-Wales defect (see Figure 9).

Geometric order

For vacancies, impurities and adsorbate defects the geometric ordering of the atoms as well as the binding behavior changes. E.g. in a zero-dimensional vacancy the neighboring atoms rearrange, see Figure 9.
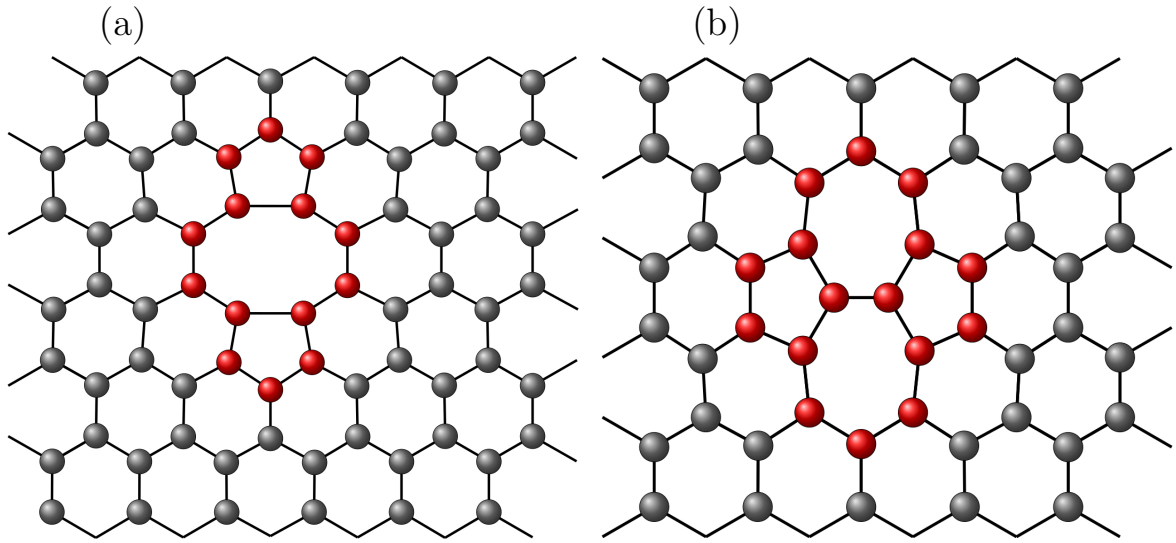
Figure 9: a: An example how the lattice can rearrange around a double vacancy. b: Image of a Stone-Wales-defect. Geometries obtained from DFT relaxations. The red marked atomic lattice sites indicate the central sites of the defect structure.

The number of these defects is very low at room temperature, due to high formation energies and (depending on the defect-type) high mobility [16]. It is possible to increase the number of defects, by irradiation using electron-beams [9] or evaporation of e.g. fluorine [8].

3.3.2   Simple defect simulation technique

To describe disorder within the tight-binding approach outlined in Section 2.3 the coupling parameters at and around the defect need to be adapted. Some defect structures such as vacancies or adsorbates can be simulated by using a very crude model: the orbitals of the defect structure are thought of as no longer participating in transport. Surrounding electrons cannot scatter into orbitals of the defect structure. To achieve this the on-site energies of defect structure orbitals are increased to a very high value (usually 1000 eV) [42].

This model has its obvious limitations as no reordering and therefore change in the surrounding interaction parameters is taken into account. Also no possible remaining scattering into the defect orbit (for example in adsorbates) is accounted for and only a limited number of defect types can be handled. Nevertheless it is a reasonable approach for e.g. fluorine defects as a carbon atom located beneath a fluorine atom forms an sp_3 hybridization where no p_z orbital is left for scattering and the lattice geometry only changes slightly [8].
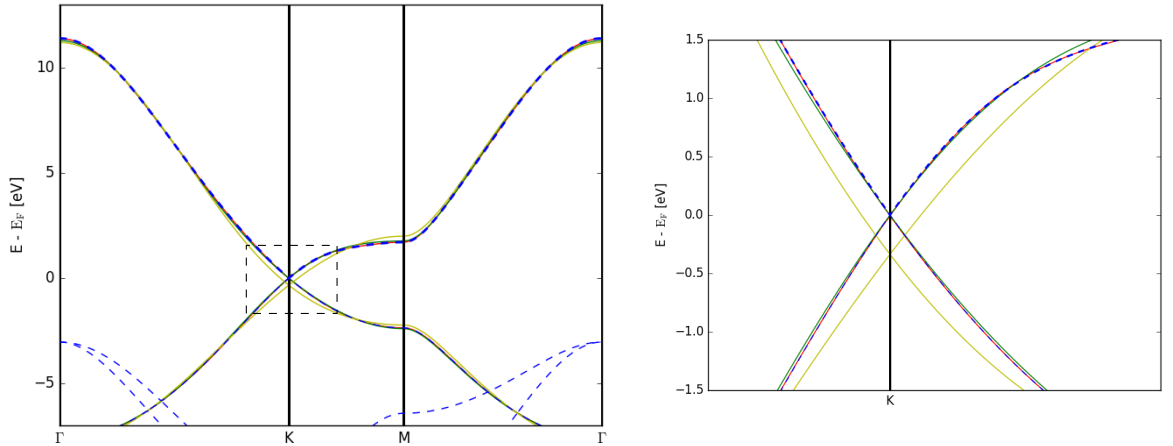
Figure 10: Band structures for a perfect lattice calculated with MLWF. Taking all (dotted blue line), up to tenth (solid red line), seventh (solid green line) and third (solid yellow line) NN parameters into account. The shift from the Fermi energy at the K point for the third NN parameter set, is caused by the cut-off of higher order NN parameters. Only with tenth NN parameter set the band structure can be reproduced accurately in the energy range ± 1.2 eV around the Fermi energy.

4   Towards an accurate defect simulation

A more advanced approach than the basic one outlined in Section 3.3.2, is to perform DFT calculations. Starting from an initial guess a number of atoms arranged in a large super cell can be relaxed into their ground state and an accurate electron density can be calculated. This is done by minimizing the Kohn-Sham energy functional as described in Section 2.1. From this ground state electron density the tight-binding parameters can be obtained via basis transformation into MLWF, as described in Section 2.2.

The challenging and limiting part in these calculations is that not only one graphene unit cell but large super cells consisting of the whole defect and some surrounding atoms have to be simulated. Depending on the defect size already zero-dimensional defects such as double vacancies need to include 70 atomic sites to obtain a structure where the atomic sites at the border of the structure rebuild perfect graphene.

How can we obtain reasonable NN parameters from such large structures? The two possible approaches for obtaining NN parameters in a perfect graphene lattice are MLWF and band structure fitting.

- **MLWF:** Starting from the Kohn-Sham orbitals in Bloch basis one can use the criterion introduced in Equation (11) to obtain Maximally Localized Wannier Functions (MLWF) and then drop all higher interaction terms. This has been done by [31], finding that at least 10th NN interaction are needed to accurately reproduce the band structure of a perfect lattice.

- **Band structure Fitting:** Another approach is to use Gauss-Newton based

least squares optimization algorithms, to optimize NN parameters up to a certain order to best fit the band structure obtained from DFT calculations. This has also be done by [31] using the Lederberg-Manquard algorithm [33, 34], for a third NN parameter set obtaining the values from Equation (47). The corresponding band structure is displayed in Figure 6.

While the method of obtaining NN sets from MLWF is also adaptable to large super cells band structure fitting is not feasible for large structures. This can be made clear when considering a double vacancy structure Figure 9 (a) consisting of 70 atoms. To optimize for a third NN parameter set 910 free parameters would need to be optimized. Even with the fourfold defect symmetry 260 free parameters are left leading to a Levenberg-Manquard optimization problem of the same dimensionality. With the unknown smoothness of this high dimensional optimization function the optimization results may be rather unphysical and the band structure fitting procedure, as used for the perfect crystal, is not applicable. Another difficulty is the assignment of which band structure line to fit to which eigenvalue of the band structure matrix. While this is straightforward for small cells (see Figure 10) it becomes an impossible task for large cells (see Figure 11).
The method of obtaining NN parameters directly from MLWF can be used but also has some unpleasant issues, as outlined in the next subsection.

4.1 Using MLWF to obtain NN parameters for large unit cells

Sticking with the example of a double vacancy one can use Wannierisation algorithms as outlined in Section 2.2 to obtain all tight-binding parameters.
From these tight-binding parameters the relevant ones have to be chosen. Proceeding the same path as for perfect graphene in [31] we now have to find the minimum number of NN that have to be considered in order to accurately reproduce the band structure. Choosing the next neighbors as outlined in Figure 7 we can compare the band structure obtained using different maximum NN numbers. Calculating different maximal NN parameters one finds that considering all NN up to the eighth NN the band structure fits the exact bandstand already very well, while when only considering up to third-nearest neighbors results are not meaningful (see Figure 11).
 Using the method of directly obtaining NN parameters from MLWFs therefore requires at least eighth NN to be useful.
Four problems occur when directly using MLWF for an exact defect description,

- **No general rule** exists to provide the needed maximum NN number in order to reproduce the defect bands with high accuracy. Therefore each defect structure potentially requires a different number of NNs for a converged description.

- **High computational effort** for defect simulations as all the surrounding perfect graphene lattice has to be calculated with NN parameters of the same order to guarantee smoothness between the WMLF parameters of the defect structure and the perfect lattice. As outlined in Section 3.2.1, using higher order NN

(a)   (b)
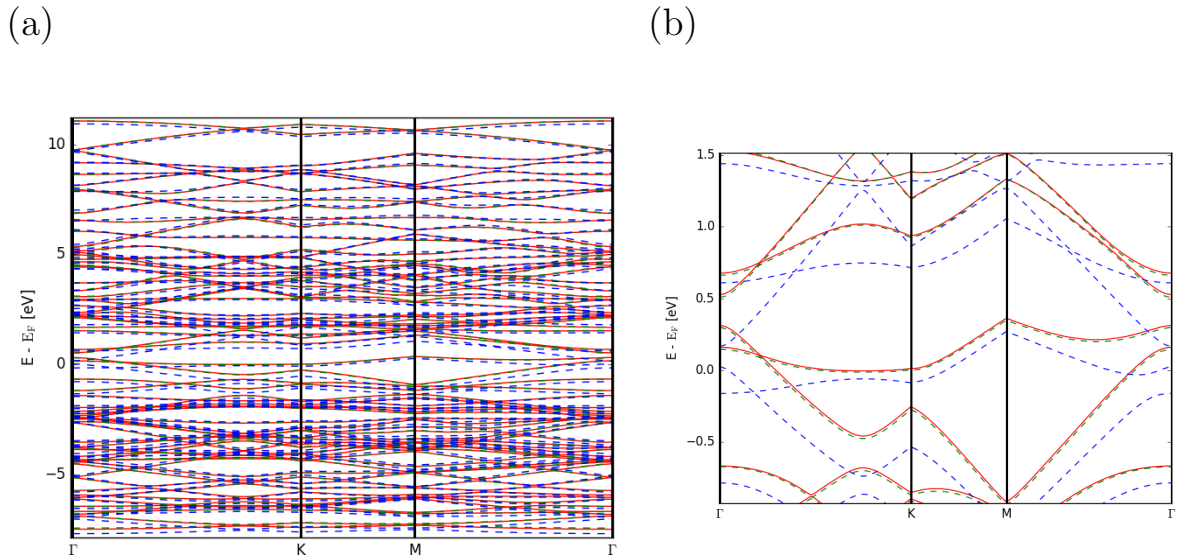
Figure 11: (a) Band structure of a double defect embedded in a 70 atom large super cell, as shown in Figure 9 (a), as calculated from DFT (solid red line), with up to eighth nearest neighbor parameters (dashed green line) and up to third-nearest neighbors (dashed blue line). (b) Zoomed in around the Fermi energy.

parameters strongly increases computational effort.

- The **modular recursive Green's function** method as introduced by [29] is **not directly applicable** for higher NN couplings anymore. Without such a method no simulation of large mesoscopic structures in a reasonable amount of time is possible.

- **Larger super cells** are needed for higher order NN couplings. This is because periodic boundary conditions in the DFT calculation cause high order NN parameters to obtain values that couple defect orbitals with the defect structure in the periodic replica of the super cell.

4.2   Embedding defects by combining MLWF and fitting procedures

Due to the impossibility of using band structure fitting and the difficulties that arise when using the MLWF method to obtain physical tight-binding parameters for defect structures we have to search for other approaches. The is obviously to increase the computational effort by as little as possible and to allow simulation of a broad range of defects.

One approach that one could think of is combining both methods such that the difficulties of each method are overcome. We meet these requirements by choosing a

mixed approach of MLWF and band structure fitting.

The idea of our embedding approach is to use a number of atoms in the perfect lattice around the calculated defect structure as transition area for the tight-binding parameters. Starting far away from the defect structure with the bulk third NN parameters obtained from fitting to the perfect band structure the number of NN parameters considered is slowly increased and their values change accordingly. This is done until up to the tenth NN parameters obtained by MLWF calculations of bulk graphene are reached. Within the region where tenth nearest neighbors are considered the defect structure then can be placed.

The reason we choose the transition area to reach up to tenth NN parameters is that we expect the band structure of tenth NN parameter calculations to perfectly resemble the accurate band structure for any given defect structure. This is a large advantage as it makes the embedding technique largely independent of the defect structure it embeds.

The procedure of our proposed embedding technique can be split into three parts,

- Starting from a perfect graphene lattice structure an area is replaced by the **defect structure** calculation.

- Around the defect area a broad **transition region has to be defined**. The transition region is further decomposed into sub-areas to ensure a smooth transition of the NN parameters. We call these sub areas curtains, as they enclose the defect like a set of curtains.

- After defining the curtains we have to **choose reasonable interaction parameters** for each of them.

4.2.1 Requirements to the defect structure calculation

When calculating the defect structure with ab-initio methods one has to keep in mind some requirements that have to be fulfilled in order to reach physical results applicable within our embedding technique. The exact parameters for density functional theory calculations and Wannierisation process are discussed in detail in Section 5. The main requirement for the ab-initio calculation employed in the embedding technique is that the calculated number of atoms and shape of the defect structure is chosen such that the NN parameters at the border of the defect are of compatible size with the ones obtained for the bulk lattice. As a general rule we found that at least one full unit cell of an essentially unperturbed lattice should lie between the mayor part of the defect and the border of the defect structure.

4.2.2 Defining the transition region

Figure 12 illustrates how the geometry is build up: at the center of the defect area lies an arbitrary defect, which fulfills the requirements of Section 4.2.1. Around this defect curtains are placed. We choose the curtains such that for any path at least one unit cell of a perfect graphene structure has to be passed, meaning that to the left and right

a slice as defined in Figure 8 is appended and to the top and bottom of the structure the slice is expanded by two atoms each.

The number of curtains to choose depends on the smoothness which is required for the transition from third NN parameters to tenth NN parameters.

One could also think of other curtain geometries, such as only appending one atom at the top and bottom each. Our choice seems reasonable as the distance in real space, that an electron has to travel to pass through the curtain is about the same in both coordinate directions.

The reason a rectangular shape of the defect structure's super cell was chosen and not e.g. a hexagonal is due to the easiness of keeping track of individual atoms with a simple shape.

4.2.3 Choose the correct parameters

To meet the criterion of smoothness between the used parameter set in the defect structure and the perfect lattice a convenient criterion has to be defined on how the NN parameters should slowly be shifted while still reproducing the correct band structure. For convenience we now introduce a notation for NN parameter sets,

$$\mathcal{S}_{\mathrm{NN_{max}}} = \{\epsilon_0^{\mathrm{NN_{max}}}, \gamma_1^{\mathrm{NN_{max}}}, ..., \gamma_{\mathrm{NN_{max}}}^{\mathrm{NN_{max}}}\} \tag{48}$$

where $\mathcal{S}_{\mathrm{NN_{max}}}$ is the tight-binding parameter set including up to $\mathrm{NN_{max}}$ parameters are non-zero and the $\epsilon_0^{\mathrm{NN_{max}}}$ and $\gamma_i^{\mathrm{NN_{max}}}$ are the NN parameters of this set.

As a starting point we used least squares optimization to the perfect band structure with ever increasing maximal NNs. This turned out to work very well (see Section 6.2). One could also think of more advanced optimization routines using Lagrange multipliers to only optimize within a subset in which the lowest γ_i for each set are confined to a certain range. As the simple approach turned out to work very well we did not use more advanced approaches even though we expect them to be more precise.

To guarantee that the tight-binding Hamiltonian is hermitian we used the following procedure to set the NN parameters within the curtain structure.

- assign every orbital i of the structure with a parameter set $\mathcal{S}_{\mathrm{N_{i,max}}}$.

- For every orbital i iterate through all orbitals j with a NN distance N smaller than $\mathrm{N_{i,max}}$.

- if $\mathrm{N_{i,max}} \leq \mathrm{N_{j,max}}$ then set the NN interaction parameter in the tight-binding Hamiltonian to $\gamma_{\mathrm{N}}^{\mathrm{N_{i,max}}}$

- If both orbitals lie within the defect structure area $\gamma_{i,j}$ is taken from the Wannier parameters obtained from the DFT calculation.

- the on-site energies ϵ_i are set to $\epsilon_0^{\mathrm{N_{i,max}}}$ inside the curtain area and to the values obtained from MLWF in the defect area.
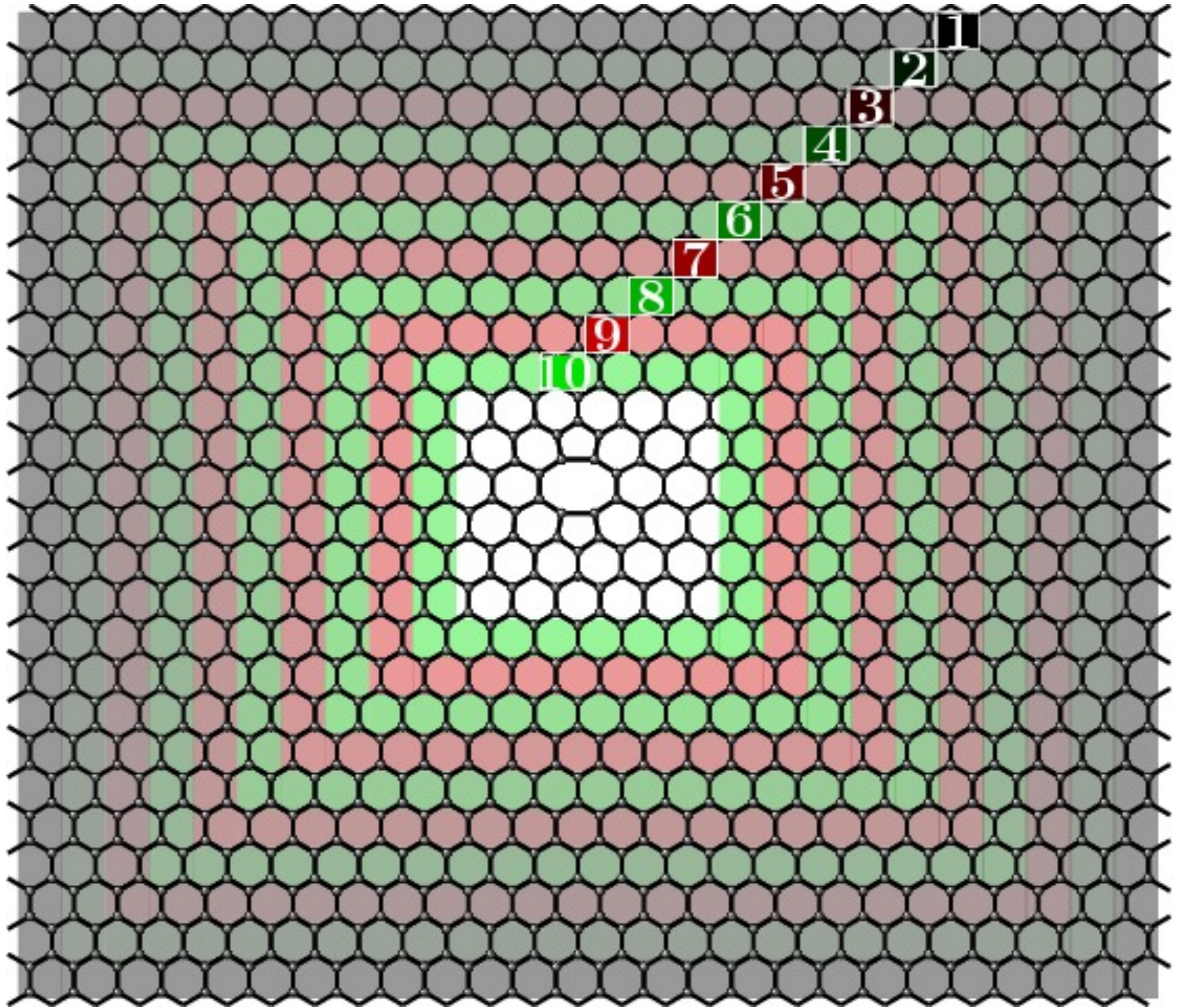
Figure 12: Defect structure (shaded white) surrounded by 10 so-called curtains enumerated from 1 to 10. Every atom within the red (or green) shaded areas is part of the corresponding curtain. In every curtain the order of included NN parameters is increased. Note that the curtain numbers indicated do not correspond to the order of NN parameters considered, e.g. curtain number four and five can both be described by a NN parameter set of order seven.

Setting the NN parameters as explained above guarantees that the Hamiltonian is hermitian. This can be made clear when looking at the tight-binding value distribution of the Hamiltonian of the single slice which "cuts" exactly through the defect structure (see Figure 13).
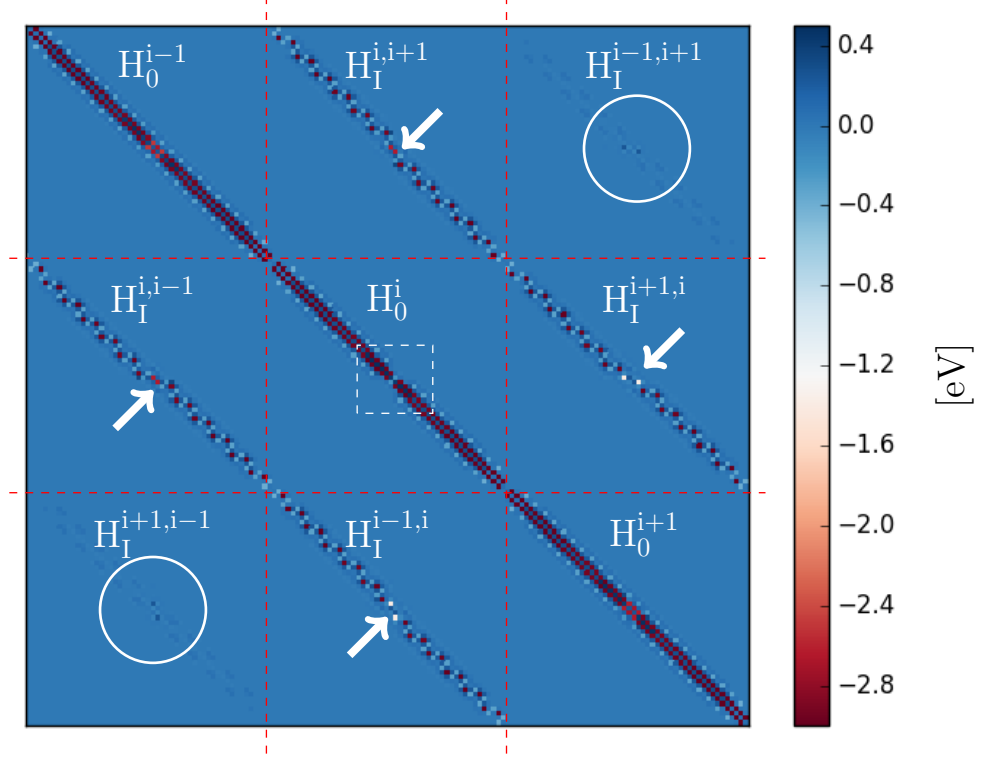
Figure 13: The NN parameter value distribution in the tight-binding Hamiltonian of the central slices of the defect structure with curtains, shown in Figure 12.

The dotted red lines indicate the border between neighboring parts of the Hamiltonian. This can be made clear by comparing the structure of this plot with Figure 8 b, where slice i is the slices which cuts exactly through the middle of the structure shown in Figure 12.

The non-interacting Hamiltonian parts of the slices H_0 are along the diagonal part, note that at the borders the number of non-zero interaction parameters decrease and in the center of each slice the parameters shift due to the influence of the defect which is located in the white rectangle. Also the center slice is two orbital sites smaller due to the missing orbitals at the defect.

The parts of the Hamiltonian that contribute to interaction between neighboring slices (indicated with white arrows and $H_I^{i,i+1}$, $H_I^{i+1,i}$, $H_I^{i,i-1}$ and $H_I^{i-1,i}$) also shift at the borders and in the middle due to defect influence. In the upper right and lower left corner also some off-diagonal non-vanishing parts of the Hamiltonian $H_I^{i-1,i+1}$ and $H_I^{i+1,i-1}$ are recognizable (white circles), these parameters are at least fourth NN parameters $\gamma_{4\leq i}$ and contribute to next to nearest neighbor slice interaction. These parameters are set zero when the lattice is treated with third NN parameter set $\mathcal{S}^3$ and therefore approach to zero at the boundary of the structure.

5 DFT calculations and Wannierisation

As outlined in Section 2.1 we used density functional theory and maximally localized Wannier orbitals to obtain tight-binding parameters. In this section these calculations are discussed in detail. In the first two sub-chapters some general points are highlighted and in the following perfect lattice calculations and individual defect structure calculations are discussed.

5.1 DFT calculations

For all DFT calculations we used VASP (Vienna ab-initio simulation package) [35, 36, 37, 38] together with the standard LDA (local density approximation) exchange correlation potential. The same procedure was used for all DFT calculations. The DFT calculations were done with an energy cut-off of 700eV, meaning that all Bloch waves up to the energy

$$E_{max} = \frac{\hbar^2}{2m} G_{cut} \qquad \text{with} \qquad G_{cut} > |\mathbf{k} - \mathbf{G}| \tag{49}$$

were used as a basis set. $\mathbf{G_{cut}}$ is the maximal super cell shift considered and m the electron mass. A Monkhorst-pack grid was used for k-point sampling of the numerical integrations together with a Gaussian smearing function with a standard deviation σ of 0.2 Å. The steps described here are all performed within VASP and only controlled via parameter input.

As **initial positions** a number of carbon atoms were placed within a defined super cell. The super cell and the position of the atoms were chosen according to a perfect honeycomb lattice. Starting from this perfect structure local perturbations were created by either removing, adding or shifting one or several atoms.
We used two different forms of periodic super cells a rectangular shape for large calculations and simple multiplicities of the normal unit cell for smaller structures (see Figure 14). There are two reasons for choosing two different shapes of super cells. The rectangular unit cell shape only builds up a periodic structure if the atoms per slice are dividable by four. Therefore if the size of a defect structure lies between two sizes of periodic rectangular shapes a unit cell like shape is preferable as the numerical effort would increase unnecessarily. The reason to -in some cases- prefer rectangular super cell shapes is that the Wannierisation for large super cells works more conveniently for the rectangular shape.

In a next step the ionic positions were **relaxed** using a conjugate gradient algorithm. Iteratively the ionic positions were shifted along the gradient of the forces, using alternating a trial step and a correction step. After every step, the electron density was calculated with DFT and new forces were obtained.
The relaxation was done until the change of the forces between two steps was smaller than 10^{-3}eV/Å.

(a)   (b)
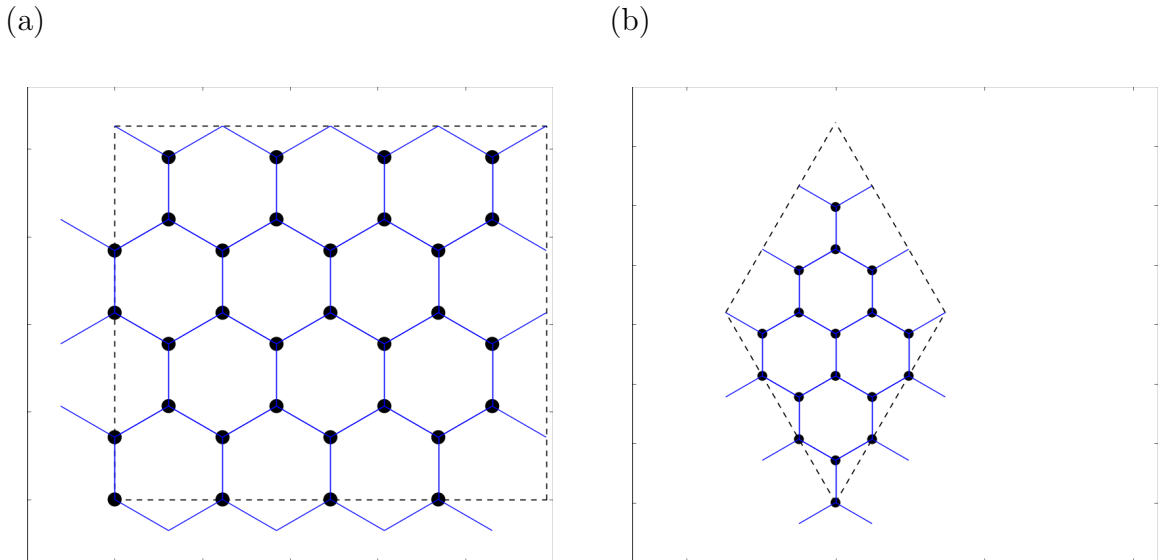
Figure 14: (a) The rectangular shape of the super cell used in DFT calculations for large structures. (b) The shape of a super cell consisting of a multiplicity of just the normal graphene unit cell.

After the relaxation an **accurate DFT calculation** was done. The Kohn-Sham functional is minimized until the energy change between two minimization steps is smaller than 10^{-6}eV. This is also done multiple times during the relaxation, but with lower accuracy as the relaxation does not need these high accuracy electron densities.

5.2   Wannierisation

As outlined in Section 2.2 Mazari and Vanderbilt developed an algorithm to obtain MLWF from a set of entangled bands [23]. We use a computational tool based on this algorithm called wannier90 [22, 23, 39] to transform the Bloch states obtained from DFT calculations into a localized basis.

In this algorithm the input parameters are initial projections onto localized orbitals, the Bloch basis overlaps, as well as a few computational parameters. The initial projections are needed to correctly disentangle the Bloch bands in order to choose the right band at every k point in the brillouin for Wannierisation (see Section 2.2 and [23, 24]). In order to obtain correct results the initial orbital projections should be chosen such that they in a good approximation rebuild the final Wannier orbitals.

The initial orbitals onto which the Bloch states are projected are LCAO orbitals with one p_z orbital at every atomic lattice site and one s orbital at every double bond centered between two atomic sites. When looking at Figure 1 one finds that the chosen p_z orbital resembles the final localized orbital well.

An alternative initial projection set could be chosen by taking the sp2 hybridized orbitals of the outer shell of the carbon atom. However we obtained more accurate results when choosing this projection set in lines with previous results [31].

29
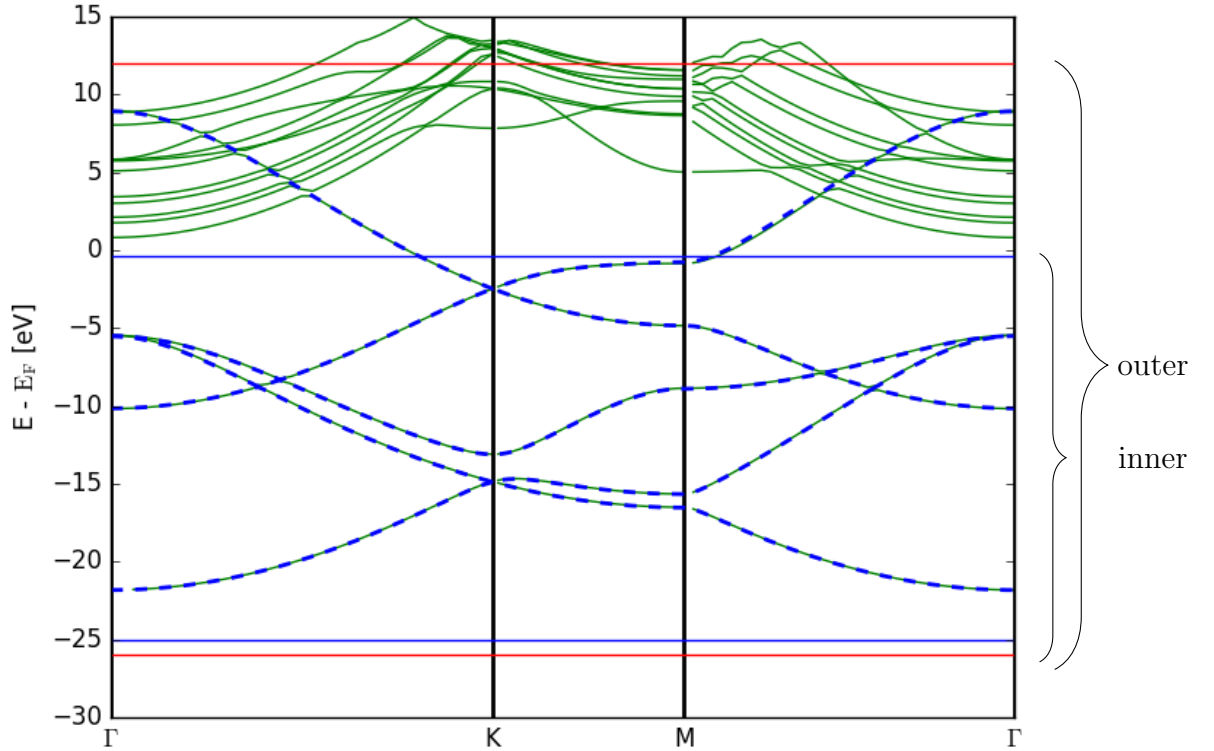
Figure 15: Illustration of the used energy windows for the disentanglement procedure. The solid green plot is the band structure obtained from DFT calculations of a simple perfect lattice unit cell as shown in Figure 14 (b), the doted blue plot is the ban structure after wannierisation. Note that only a small fraction of the band structure calculated with DFT is used in the wannier basis. To choose the right bands from the DFT calculation the inner energy window has to set right below the minimum of the lowest band, which is not used in the Wannierisation and the outer energy window limit is placed exactly above the maximum value of the highest band considered.

Other important parameters which do also concern the disentanglement are the chosen inner and outer energy window. They define the energy range in which bands of the band structure and therefore their Bloch functions can / have to be included in the disentanglement procedure. All bands that lie within the outer energy window can be included in the disentanglement meaning they build up the space $\mathcal{S}(\mathrm{k})$ defined in Section 2.2. All bands within the inner energy window have to be part of the sub space $\mathcal{F}(\mathrm{k})$ that minimizes Ω_I (see Section 2.2). The extend of the two windows massively influences the convergence of the disentanglement procedure. In all Wannierisation calculations we set the inner energy window in the range of -25 eV to -0.4 eV and the outer energy window from -26 to 12 eV (see Figure 15).
   The Wannierisation process leads to no loss of information on the relevant bands as it only entails a unitary basis rotation. The band structure is obtained with equivalent

accuracy (see Figure 15).

The maximum number of iteration steps we chose for the disentanglement (as described in [24]) was 5000 steps and for the Wannierisation (as described in [23]) was 500 steps. Although these parameters are of minor importance as the iterations should converge before this high number of iteration steps is reached they can work as benchmark numbers. If the disentanglement or the Wannierisation has not reached the required accuracy before the maximum number of iterations, some parameters of the calculation such as the projections or the energy windows were not set properly.

5.3 Curtain parameter calculations

To obtain the tight-binding parameter sets $\mathcal{S}^{i}$ of the curtains a DFT calculation of a single perfect lattice unit cell was performed and the Wannier parameters were calculated. Starting from these parameters a least square Levenberg-Marquard fitting was used to calculate the $\mathcal{S}^{NN}$ for each set of NN parameters, used in different curtains. For the DFT calculation, a k-point grid of 35x35x1 samples was used. Together with the Monkhorst sampling with which, due to symmetry only 1/12 of the reciprocal unit cell had to be calculated, this provided a rather fine k-mesh. It was important to use an odd number of sample points in the xy plane. Otherwise the high symmetry points K and K' of the reciprocal unit cell would not be evaluated directly but interpolated, leading to a large error at these -for transport highly important- points.

For the case of a perfect lattice structure no relaxation calculation was needed, as the lattice constant was already known from [31] giving 1.4208 Å and the ionic positions could be set accordingly.

Wannierisation was done using initial projections onto three s orbital located between the two lattice sites and two p_z orbitals located at the atomic lattice sites for each unit cell (see Figure 16). The validity of the transformation was verified by comparing the two band structures before and after the Wannierisation which showed perfect agreement (see Figure 15). The Levenberg-Marquard algorithm [33, 34] tries to minimize the norm

$$||\mathbf{y} - \mathbf{f}(\mathbf{x}, \boldsymbol{\beta})||^2. \tag{50}$$

Where $\mathbf{y}$ are the target values for the fit and $\mathbf{f}$ is the function under variation of the fit parameters $\boldsymbol{\beta}$. In our case $\mathbf{y}$ is the perfect band structure, $\mathbf{f}$ is the eigenvalue problem of the tight-binding Hamiltonian described in Section 2.3.1 and $\boldsymbol{\beta}$ is the corresponding parameter set $\mathcal{S}$.

The correction term $\boldsymbol{\delta}$ for the parameter set $\boldsymbol{\beta}$ is calculated in each step by solving,

$$(\mathbf{J}^{T}\mathbf{J} - \lambda\mathbf{I})\boldsymbol{\delta} = \mathbf{J}^{T}[\mathbf{y} - \mathbf{f}(\boldsymbol{\beta})]. \tag{51}$$

The $\mathbf{J}$ is the Jacobian matrix of the function $\mathbf{f}$ and λ serves as damping factor with $\mathbf{I}$ the unit matrix. As a starting set for the Levenberg-Marquard optimization of $\mathcal{S}^{10}$ we used the parameters obtained from Wannierisation, dropping all higher NN parameters. For every lower set $\mathcal{S}^{i}$ we used $\mathcal{S}^{i+1}$ as a starting point, dropping the highest γ_{i+1}. The values we obtained are given in Table 1. The $\mathbf{y}$ onto which the fitting was executed were taken from the band structure calculated with DFT, which lie within the considered energy range, ± 1.2eV from the Fermi energy.
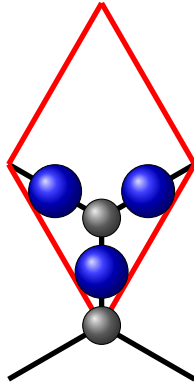
Figure 16: The large blue spheres indicate the position of the initially projected s orbitals relative to the carbon atoms of one unit cell (border indicated by red lines). The smaller gray spheres indicate the position of the carbon atoms and the p_z orbitals used for initial projections of the perfect lattice structure for Wannierisation.

[eV]	$\mathcal{S}^{10}$	$\mathcal{S}^9$	$\mathcal{S}^8$	$\mathcal{S}^7$	$\mathcal{S}^6$	$\mathcal{S}^5$	$\mathcal{S}^4$	$\mathcal{S}^3$
ϵ_0	0.29697	0.29499	0.29464	0.30003	0.30323	0.29570	0.08835	0.07893
γ_1	-2.91164	-2.92326	-2.95482	-3.03528	-3.11753	-3.14029	-3.09637	-3.28542
γ_2	0.22317	0.22675	0.22625	0.23194	0.23803	0.23385	0.03508	0.03186
γ_3	-0.28900	-0.29228	-0.28632	-0.29412	-0.30412	-0.31542	-0.29678	-0.37544
γ_4	0.02480	0.02503	0.02445	0.02512	0.02598	0.02730	0.03617	
γ_5	0.05493	0.05380	0.05358	0.05532	0.05752	0.06778		
γ_6	-0.02232	-0.02161	-0.02163	-0.02235	-0.02321			
γ_7	-0.01295	-0.01257	-0.01260	-0.01299				
γ_8	-0.02181	-0.02115	-0.02111					
γ_9	0.00716	0.00695						
γ_{10}	0.00400							

Table 1: Tight-binding parameter set values obtained from fitting. $\mathcal{S}^i$ is the parameter set that accounts for up to i NN parameters.

One can verify the set by comparing the resulting band structure with the original band structure from the DFT calculation (see Figure 17). To use the parameter sets in the curtain area of the embedding technique introduced in Section 4 the condition of smoothly shifting parameters between adjacent curtains must be fulfilled. The criterion is met by most but not all parameters in Table 1. This was considered a problem for the embedding technique. However, the benchmark calculations in Section 6.2 show that the parameter shifts are sufficiently smooth and the obtained parameter sets are suitable for the embedding technique.
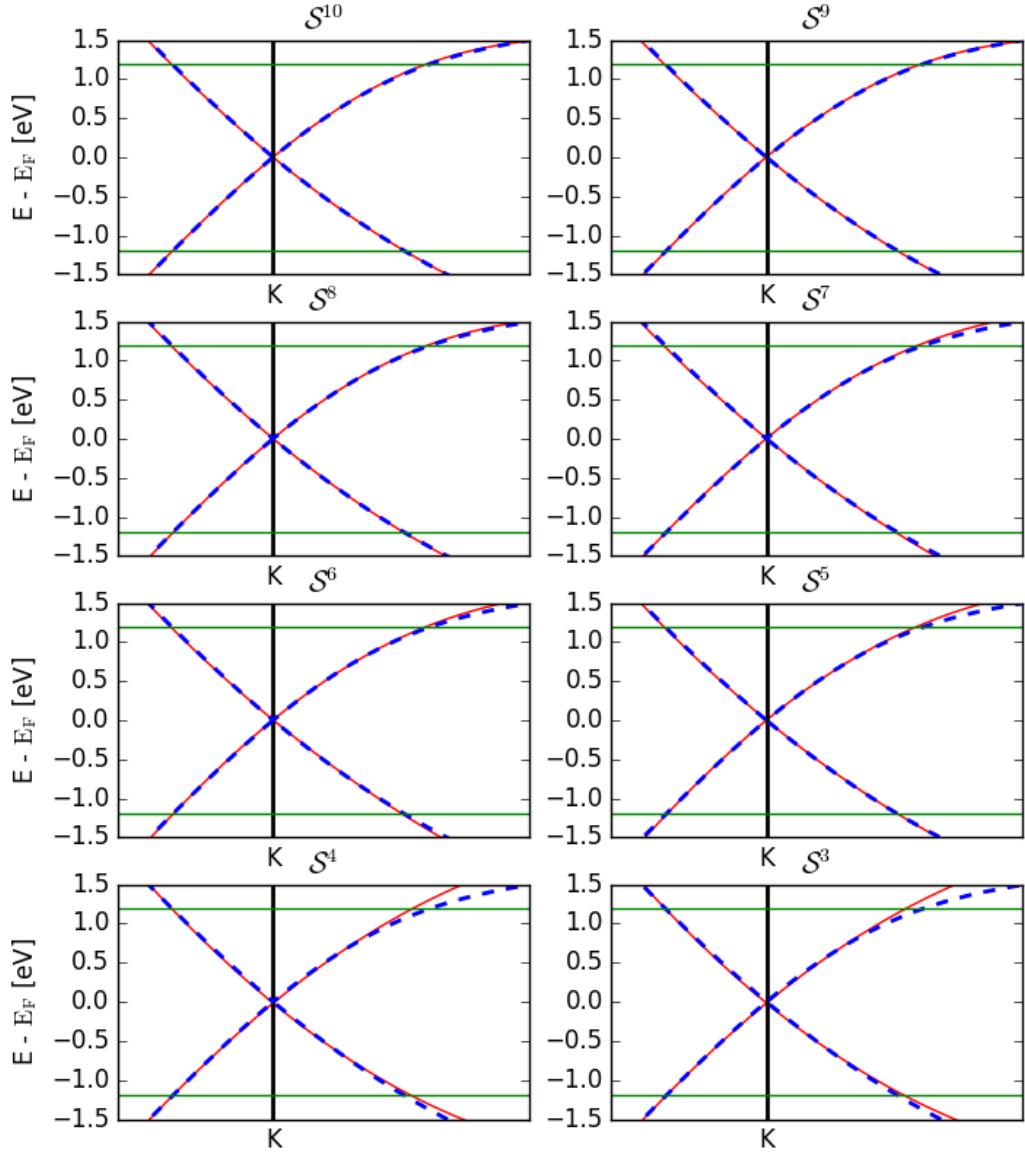
Figure 17: The band structures calculated with the fitted tight-binding parameter sets $\mathcal{S}^i$. The solid green lines indicate the optimized energy window. The dotted blue line is the band structure around the K point, calculated with DFT, the solid red line indicates the band structure calculated with the optimized tight-binding parameter sets.

5.4 Defect structures calculations

To accurately simulate defects not only the embedding has to be performed with high accuracy but also the defect structure calculations need to be of high quality. We performed DFT calculations for four different types of defects: Stone-Wales, double vacancies, silicon substitute and flower-like defects.

Problems in the compatibility of the programs VASP and Wannier90 caused difficulties when performing spin polarized calculations. Therefore no defect structures that would need to be calculated spin polarized (e.g. single vacancies) could be treated.

5.4.1 Stone-Wales

The influence of the Stone-Wales (SW) defect, the most investigated defect structure in graphene with a rather low activation energy of 2 eV [12], on transport properties was already discussed for nanoscale GNRs [14]. To calculate this defect we used a super cell consisting of 50 atoms arranged in a perfect lattice in a super cell consisting of 5x5 unit cells (see Figure 18 (a)). Only two atoms in the center of the super cell were shifted from their initial position into a position very close to the expected relaxed ionic positions of the SW defect.

For the relaxation calculation all ions were allowed to shift into all directions of space, except the right and bottom border atoms of the structure that were fixed to achieve converge of the defect structure towards the bulk lattice (see Figure 18 (b) bottom and right).

Due to the large number of atoms and the large real space extension of the super cell a smaller k point sampling had to be chosen: only three k points in each direction of the xy plane were sampled. However, due to the large super cell the reciprocal unit cell is very small and a small number of k points is therefore sufficient.

Comparing the band structure obtained from using the final tight-binding parameters up to tenth NNs, to the band structure calculated with DFT, the results show perfect agreement (see Figure 19). For the atomic lattice sites, 0-4, 10-14, 25, 20, 21, 42 and 43 as numbered in Figure 18 the next neighbor parameters up to 10 nearest neighbor are listed in Appendix A.1. All other hopping parameters can be obtained from these values due to symmetry of the structure.
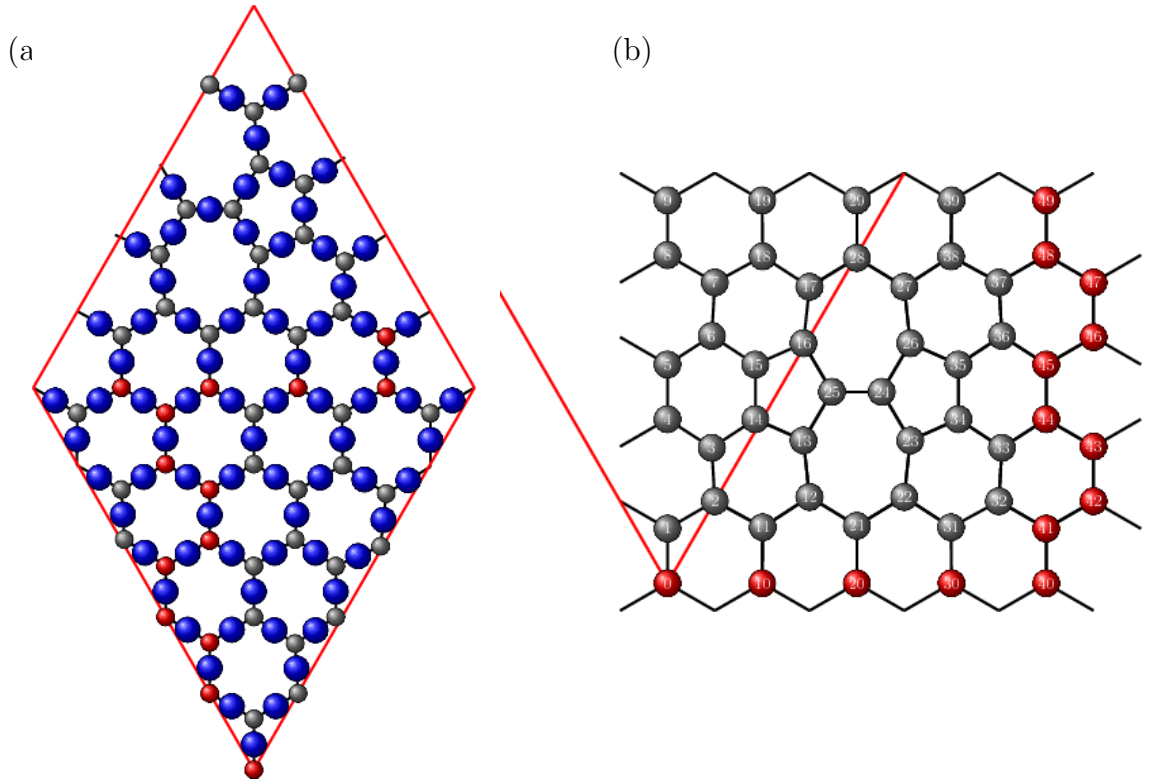
Figure 18: (a) Shows how the atoms are arranged in the super cell during the DFT calculation. The red atomic lattice sites are fixed in space during relaxation. The large spheres indicate the projection positions of the s orbitals in the Wannierisation.

In (b) the lattice structure is rearranged, such that the defect is at the center of the structure. This is done by full unit vector shifts of a number of orbitals, as the structure is calculated with periodic boundary conditions this shifting is valid. Also the atomic lattice sites are numbered.

5.4.2 Double Vacancy

To test the embedding model on vacancy type defects we also calculated a double vacancy structure. The DFT calculation discussed below fails for single vacancies, as for half filled orbitals also spin contributions need to be considered. A rectangular super cell with 70 atoms was used to calculate this defect (see Figure 20). Due to the large super cell also only three k points per direction in the xy plane were used. For the ionic relaxation all atoms were allowed to move except the ones on the bottom and the right of the super cell (red indicated atoms in Figure 20). In Figure 20 (a) also the chosen s orbital projections are shown.

The tight-binding parameter set $\mathcal{S}^{10}$ obtained from this calculation is listed in Appendix A. Due to the large number of atomic sites in the super cell, only the orbital sites 0-6,12-18 and 24-27 are listed, all parameters belonging to other orbital sites can be obtained through defect structure symmetry.
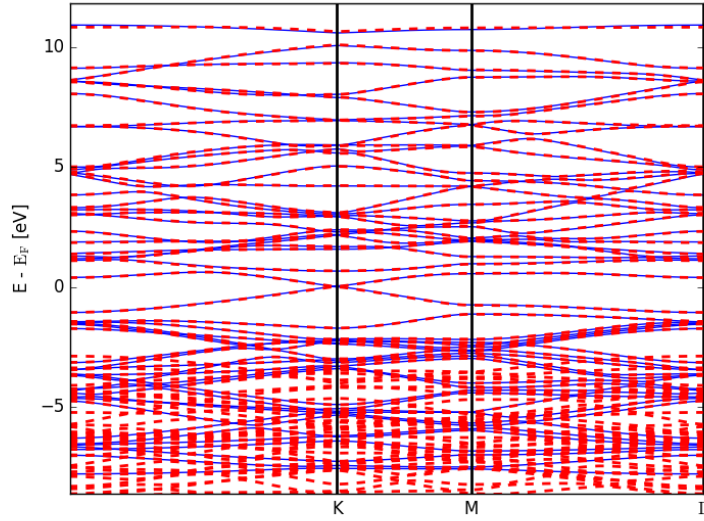
Figure 19: Band structures of the defect structure with a Stone-Wales defect, shown in Figure 18 (a). The dashed red line indicates the band structure obtained from DFT calculation, the solid blue line shows the band structure after dropping NN parameters higher than tenth. Perfect agreement between the two is found.

(a)

(b)
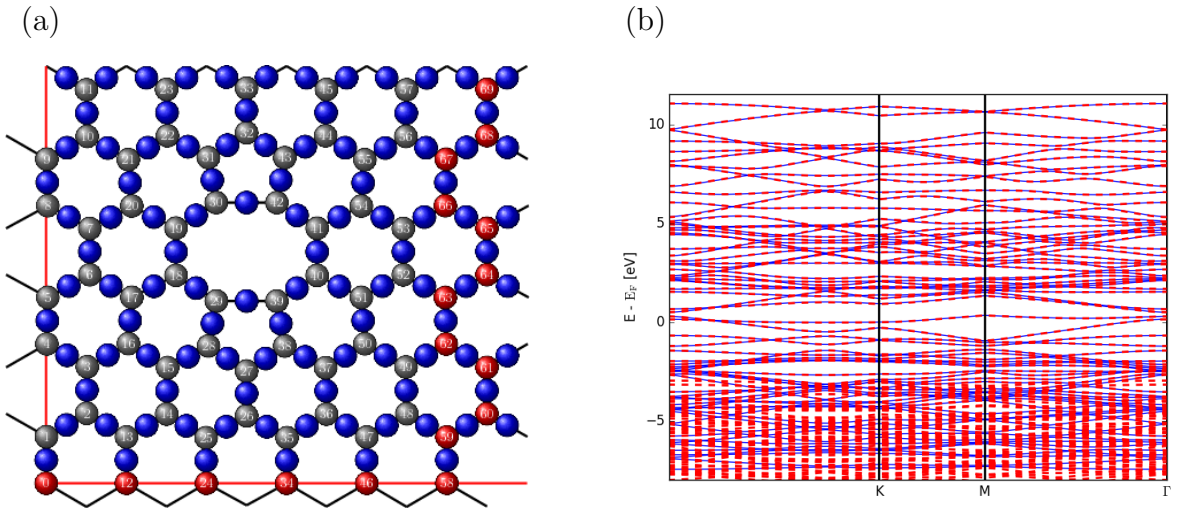
Figure 20: (a) Atomic ordering of the atoms after DFT relaxation calculation. The red atomic sites denote the atoms, which were fixed in space during relaxation. The blue spheres indicate the positions of the s orbitals used for initial projection during Wannierisation.
(b) The band structures for a double vacancy structure as shown in (a). The dotted red lines indicate the band structure calculated with DFT, the solid blue lines show the band structure calculated with up to tenth NN parameters. The two band structures show perfect agreement.

36

5.4.3 Silicon Substitution

To also test the embedding technique for substitutes we consider a single silicon atom replacing one carbon atom in a perfect graphene lattice structure. As the lattice atoms in this defect structure are expected to shift only slightly in the xy plane, a smaller configuration consisting of only 31 carbon atoms and one silicon atom were used in a rectangular shaped super cell (see Figure 21 (a). The initial projections used to disentangle the four valence orbitals of the silicon atom were chosen as sp2 hybridized, equivalent to the hybridization of the carbon atoms in a perfect graphene lattice.

The band structure obtained from DFT calculations shows perfect agreement with the band structure calculated with up to tenth NN parameters (see Figure 21 (b)). In Appendix A.4 the tight-binding parameter for the atomic numbers (numbered in Figure 21) 0-3, 8-11, 16, 17 and 20 are listed. The hopping parameters for the other lattice sites can be obtained from these values using symmetry.

(a) (b)
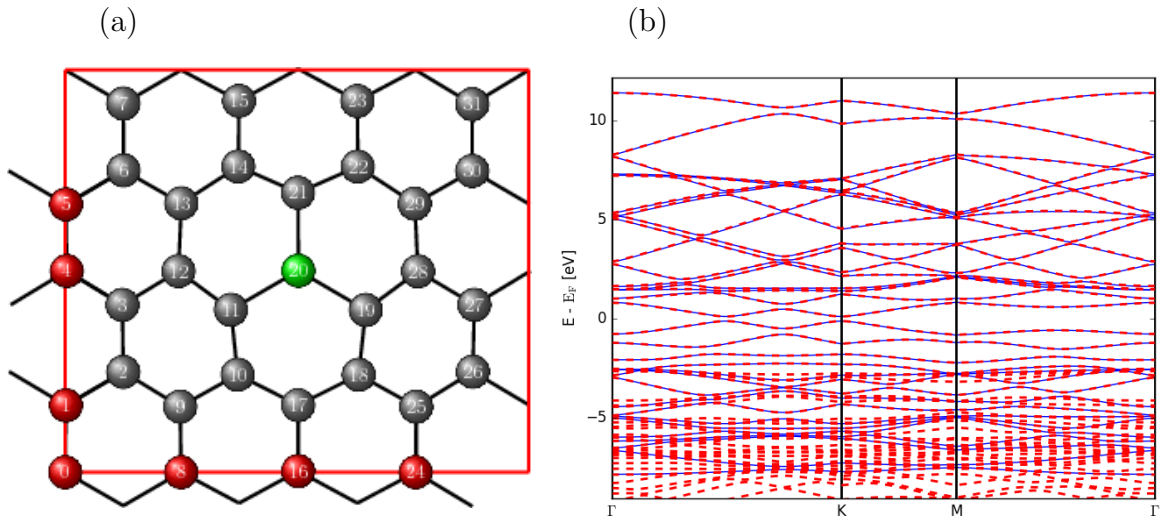
Figure 21: (a) Atomic ordering of the atoms after DFT relaxation calculation for the silicon substitute defect structure. The atoms next to the substitution are shifted slightly away from the silicon. The red atomic sites denote the atoms which were fixed in space during relaxation, the green atom is the silicon substitute. (b) The dashed red line indicates the band structure calculated with DFT and the solid blue line the band structure calculated with up top tenth nearest neighbor parameters. The two band structures show perfect agreement in the energy range around the Fermi energy which is relevant for transport.

5.4.4 Flower defect

A flower defect consists of six pairs of 5-fold and 7-fold rings of carbon atoms (see Figure 22). Flower-like rotational grain boundaries have a very low activation energy (1.2eV per pair) and are considered to have a large influence on transport properties [12]. Although it is not yet entirely clear how they form, it is suggested that nitrogen atoms may work as a catalyst or moving groups of Stone-Wales defects form flower defects [13].

For the DFT calculations we used a rectangular super cell consisting of 128 atoms. The defect is built by cutting out the center atoms of the defect, rotating them by 30 degrees and "gluing" them again, via DFT relaxation calculations. Due to the large super cell, a small k mesh of only 3 samples per direction in the xy plane, were chosen. In Appendix A.3 the hopping parameters for the atomic lattice sites 1-3, 17, 33-36 and 49-56 are tabulated, all other hopping parameters can be obtained from this set, due to the sixfold symmetry of the defect.
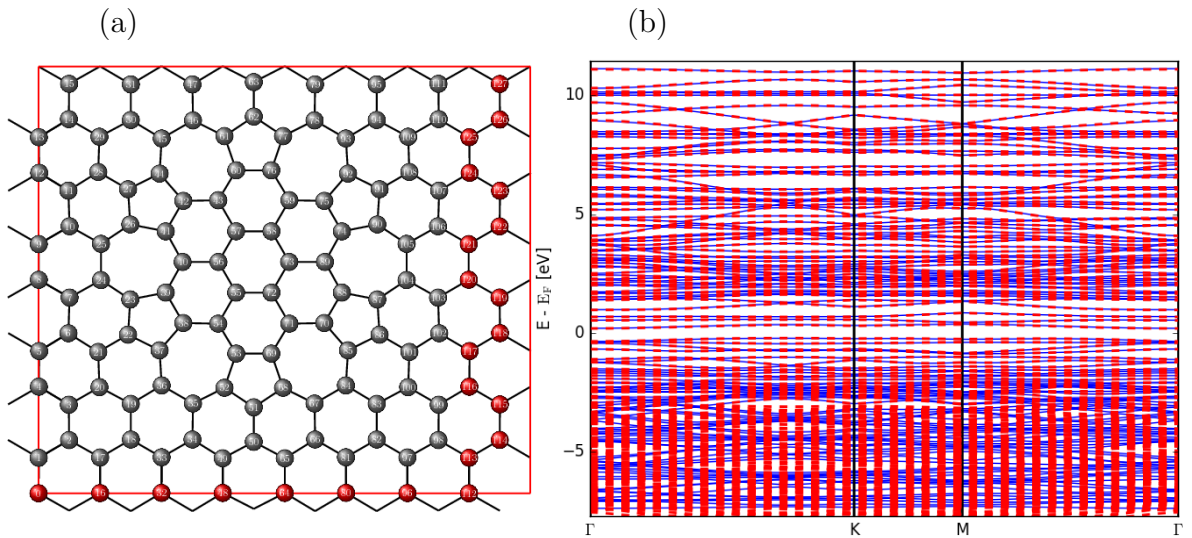
Figure 22: (a) Geometry of the relaxed flower defect. The red atomic sites denote the atoms fixed in space during relaxation. (b) The dotted red lines show the band structure calculated with DFT, the solid blue lines indicate the band structure calculated with NN parameters considering up to tenth NNs. Perfect agreement between the two band structures is found over the whole energy range.

6 Testing the embedding technique

Up to this point we have explained how an embedding technique for defect structures could look like and have discussed all calculations necessary to realize such an embedding. In this chapter the validity of the developed technique is tested and some results are presented.

At the University of Vienna transport measurements in graphene are currently conducted. We hope to be able to explain some observations made by this experiment. Therefore we modeled our embedding test suite such that it resembles the experimental setup. We first describe the experiment and how we modeled it and in the following sub-chapters we test the embedding technique by the embedding of defect free structures.

6.1 An experimental setup

A minimal transport measurement in solids consist of a sample structure and at least two contacts with voltage bias. The measured observable is then the current flow between two contacts or leads. However, with this approach a lot of information on the interior scattering behavior is lost or can only be measured indirectly.

2D materials offer new ways to directly measure the electron density at any position in the lattice due to the accessibility of measurement tools from either side. The group of Meyer at the University of Vienna tries to realize such a measurement [17]. They access a free hanging single layer graphene sheet from two sites with two scanning tunneling microscope (STM) tips, using one of the tips as a electrical contact. Between the tip used as contact and another contact far away from the measured region a voltage bias is applied. The second tip scans over the lattice to measure the electron density in each orbital that interacts with the STM tip. Other experimental configurations with the same setup can be achieved by varying the potential between the lattice, the contact tip and the scanning tip.

The electron density measured is the electron density in the p_z orbitals, as only they contribute significantly to the tip-lattice interaction. The electron density in each p_z orbital is proportional to the probability of the electron to scatter into this lattice site. As outlined in Section 2.4.2 the scattering probability is given by the absolute squared of the response of the system, which can be calculated by applying an excitation onto the Green's function describing the lattice. We therefore are able to model this experiment.

The size of the modeled lattice was chosen to be 545×630 nm (equals 256×512 atoms), a size that is computable in a reasonable amount of time and also leaves almost no boundary effects in the region of interest.

Dyson's equation was used to join slices of the lattice iteratively (see Figure 8) to efficiently calculate the Green's function of the lattice. To prevent backscattering at the boundaries of the structure half infinite leads were attached to the structure on all four sides. The only hard wall boundaries remaining in our model are the corners of the structure. The backscattering of electrons at these edges is negligible. Without the leads at all four sides boundary backscattering dominates the electron scattering in the simulation. By contrast, the size of the experimental flake ($\approx$1 μm) precludes any

significant finite size effects.

Using a tight-binding model together with our embedding technique is an approxima-
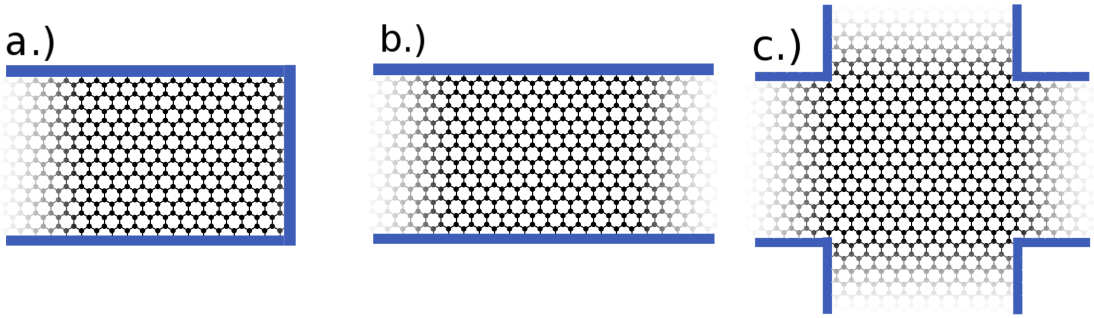
Figure 23: Different configurations with hard wall boundary conditions.Image (c) reproduces the physical most accurate boundaries, as only very little backscattering from the remaining edges occurs.

tion which does not account for several effects. Besides the ones listed in Section 2.3 these effects are,

- deformation of the lattice due to tip-lattice interaction,

- heating due to the current (actually any finite temperature effects are not included),

- oscillations of the freely hanging lattice

- and influence of the surrounding atmosphere.

How large these effects are is partly still under investigation. Nevertheless we hope to have established a reliable model.

6.2 Defect free scattering patterns

Before testing the embedding method the defect free scattering amplitudes for the configuration outlined above are discussed. Due to the imperfect cone form of the dispersion relation around the high symmetry points we found interesting scattering patterns even for perfect graphene lattices.

The Green's function is a direct measure of the response of a system to an excitation. The current induced by the contact tip is an excitation of the system at the orbital site $|\Phi_i\rangle$ in contact. The response of the system is obtained by applying the excitation to the Green's function,

$$R = GS. \tag{52}$$

$|R|^2$ is the probability for an electron injected by the tip to scatter into any lattice site. We discuss two cases: (i) an excitation at only one lattice side, equal to a STM lattice interaction between only one p_z orbital with a normalized excitation,

$$S_1 = |\Phi_{i\rangle} \tag{53}$$

40

and (ii) the excitation of two neighboring lattice sites, equal to an STM tip coupling to two adjacent orbitals, expressed by the excitation,

$$S_2 = \frac{1}{\sqrt{2}}(|\Phi_i\rangle + |\Phi_{i+1}\rangle). \tag{54}$$

(i) When applying the excitation of Equation (53) onto the Green's function of the simulated graphene structure the scattering amplitude of the electrons in this configuration can be calculated (see Figure 24 (a)). In this scattering pattern six preferred scattering directions can be identified. The reason they occur can be understood by looking at the dispersion relation of graphene which deviates from the perfect cone shape at high energies forming a threefold symmetry around the K point (see Figure 5 (b)). With equally distributed wave number $\vec{k}$ along the dispersion relation electrons are more likely to be scattered into directions with larger absolute $\vec{k}$ values. The same threefold symmetry emerges around the K' point, only rotated by 60 degrees. This deviation of the dispersion relation around the K and K' point is called trigonal warping. As electrons scatter equally around the K and the K' point six dominant directions of scattering emerge. The preferred scattering directions become more pronounced as the electron energy increases since the deviation of the band structure increases for increasing energies.

(ii) Placing the STM tip exactly between two lattice sites causes an excitation as given in Equation (54). This excitation contributes equally to electron scattering into either lattice site, A or B. Typical scattering amplitudes of electrons in the lattice with an excitation of this form are shown in Figure 25. The twofold symmetry of the preferred scattering directions can be understood when expanding the tight-binding Hamiltonian around the K and K' points up to second-order and calculating the resulting wavefunctions. The second-order Hamiltonian expanded around K reads [40, 41],

$$H(\vec{q}) = v(q_x\sigma_x + q_y\sigma_y) - \epsilon\left[(q_x^2 + q_y^2)\sigma_x - 2q_x q_y\sigma_y\right] \tag{55}$$

and can be rewritten to

$$H(\vec{q}) = \begin{pmatrix} 0 & v|\vec{q}|e^{-i\theta(\tilde{q})} - \epsilon|\vec{q}|^2 e^{2i\theta(\tilde{q})} \\ v|\vec{q}|e^{i\theta(\tilde{q})} - \epsilon|\vec{q}|^2 e^{-2i\theta(\tilde{q})} & 0 \end{pmatrix} \tag{56}$$

$$\text{with} \quad \theta = \arctan\left(\frac{q_x}{q_y}\right). \tag{57}$$

Here $v \approx 5.37$ eVÅ and $\epsilon \approx 4.12$ eVÅ^2 are expansion coefficients that we calculated via band structure fitting [42]. The σ_x and σ_y are the Pauli matrices and $\vec{q}$ is the wave vector origin in K, with $\vec{q} = \vec{k} - \vec{K}$. The Schrödinger equation around K,

$$\begin{pmatrix} 0 & v|\vec{q}|e^{-i\theta(\tilde{q})} - \epsilon|\vec{q}|^2 e^{2i\theta(\tilde{q})} \\ v|\vec{q}|e^{i\theta(\tilde{q})} - \epsilon|\vec{q}|^2 e^{-2i\theta(\tilde{q})} & 0 \end{pmatrix} |\psi\rangle = E|\psi\rangle \tag{58}$$

can now be calculated analytically. The eigenfunctions obtained are given by,

$$\psi_K(\vec{q}) = \frac{1}{\sqrt{2}}\begin{pmatrix} \pm\sqrt{\frac{\alpha(\vec{q})}{\beta(\vec{q})}} \\ 1 \end{pmatrix} \tag{59}$$

41
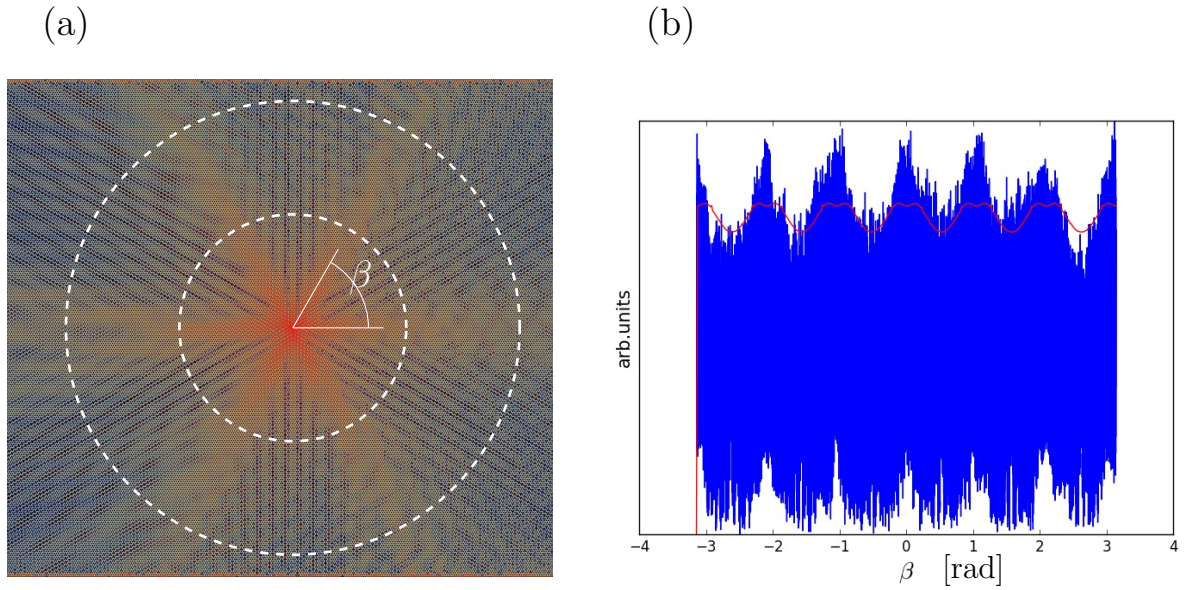
Figure 24: (a) The scattering amplitude for an electron injected by the STM tip into the graphene sheet at any point in the lattice. This is proportional to the absolute value of the response of the system. In this image the excitation was given by Equation (53), leading to a clear threefold symmetry -so-called trigonal warping- and six preferred scattering directions. The scattering amplitude shown in this plot was calculated with the geometry and parameters introduced in the beginning of this chapter, with an electron energy of 1 eV. The STM tip and therefore the excitation is attached to the lattice site exactly at the center of the structure. (b) Explanation of the six preferred scattering directions. The blue area indicates the angular resolved probabilities to scatter into lattice sites between the two circles indicated in (a). The red line shows the number of k states per scattering angle from the second-order dispersion relation around K and K'.

with

$$\alpha(\vec{q}) = v_F |q| e^{-i\theta(\vec{q})} - \epsilon |q|^2 e^{2i\theta(\vec{q})} \qquad \beta(\vec{q}) = v_F |q| e^{i\theta(\vec{q})} - \epsilon |q|^2 e^{-2i\theta(\vec{q})} \qquad (60)$$

and eigenvalues

$$E_\pm(\vec{q}) = \pm\sqrt{\alpha(\vec{q})\beta(\vec{q})}. \qquad (61)$$

With the same procedure as above the wavefunction around K′ can be calculated analytically yielding,

$$\psi_{K'}(\vec{q}) = \frac{1}{\sqrt{2}} \begin{pmatrix} \mp\sqrt{\frac{\alpha'(\vec{q})}{\beta'(\vec{q})}} \\ 1 \end{pmatrix} \qquad (62)$$

with

$$\alpha'(\vec{q}) = v_F |q| e^{-i\theta(\vec{q})} + \epsilon |q|^2 e^{2i\theta(\vec{q})} \qquad \beta'(\vec{q}) = v_F |q| e^{i\theta(\vec{q})} + \epsilon |q|^2 e^{-2i\theta(\vec{q})}. \qquad (63)$$

When taking the absolute value of the summed wavefunctions [42],

$$|\psi_K + \psi_{K'}| \qquad (64)$$

one finds the curve shown in Figure 25 (b). This analytic expansion rebuilds the simulated scattering amplitudes remarkably well. The analytic model and the simulation predict both a far more pronounced angle dependent scattering for the excitation in (ii) than for the trigonal warping effect as found for an excitation given in (i).

A more detailed discussion of the preferred scattering directions in defect free lattices of this configuration can be found in [42].
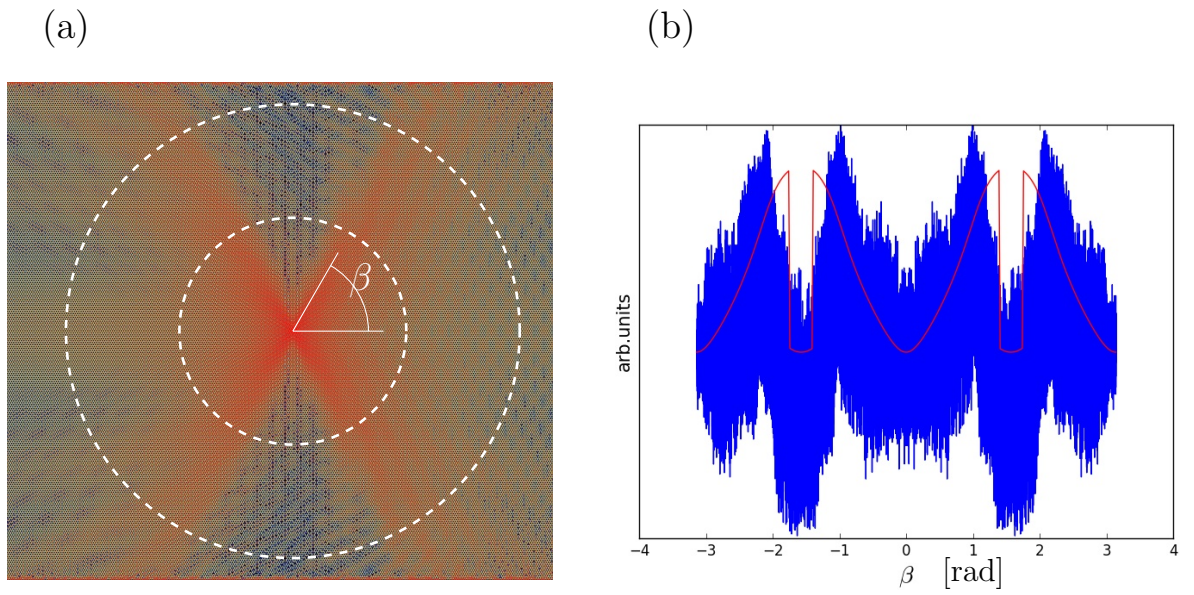
Figure 25: (a) Scattering amplitudes for electrons injected by an STM tip exactly between two atomic lattice sites for an electron energy of 1 eV. A very clear twofold symmetry is established that can be understood as an interference effect of the two wavefunctions around K and K'. (b) Comparison between simulation and analytic model. The blue area shows the angular resolved probability values taken from all lattice sites between the two dotted white circles of (a). The red line shows the result of the analytically model. For larger electron energies the twofold symmetry becomes even more pronounced.

6.3 Perfect lattice embedding

Before embedding defects into the lattice configuration we use the embedding technique on a defect free lattice. By comparing the differences in scattering amplitudes of defect free simulations and simulations with a perfect lattice embedding the order and type of the perturbations due to embedding can be studied.

The reason the embedded structure is a perturbation of the perfect lattice described with third-nearest neighbors is due to the different NN descriptions in the transition area. We therefore expect differences in the scatter amplitudes for a perfect graphene lattice simulated with third nearest-neighbor parameter sets and a perfect lattice embedding. This scattering is a consequence of the curtain method, as it would not occur for a lattice structure simulated everywhere at the tenth-nearest neighbor level. Due to the relative smooth transition of NN parameters in the curtain area of the embedded structure, this perturbations are expected to be small and the scattering should be dominated by the embedded defect structure.

We studied this effect by placing a 50 atom high and 25 slices wide defect into one of the preferred scattering directions of Figure 24, starting at a distance of 14 slices ($\approx 34\text{Å}$) of the STM tip. The size and position of the embedded structure is outlined in Figure 26 a (i).

To compare the the two calculations we used the difference of the scattering amplitudes

$$\Delta_{\text{diff}} = \left| |\text{R}| - |\text{R}'| \right| \tag{65}$$

Where R is the response of the system with third-nearest neighbor description and R′ the response of the system with perfect lattice embedding. For the defect structure we used curtains C_i (numbered in Figure 12) together with parameter sets from Table 1 and assigned in Table 2.

C_1	C_2	C_3	C_4	C_5	C_6	C_7	C_8	C_9	C_{10}
$\mathcal{S}^3$	$\mathcal{S}^4$	$\mathcal{S}^5$	$\mathcal{S}^5$	$\mathcal{S}^6$	$\mathcal{S}^7$	$\mathcal{S}^8$	$\mathcal{S}^8$	$\mathcal{S}^9$	$\mathcal{S}^{10}$

Table 2: Parameter sets used for different curtains.

The reason curtains C_4 and C_5 where both assigned with the parameter set $\mathcal{S}^5$ is due to the large parameter shifts from $\mathcal{S}^4$ and $\mathcal{S}^5$. By assigning the same parameter set to two neighboring curtains the transition is made slightly smoother. This was also the reason to choose the parameter set $\mathcal{S}^8$ on both curtains C_7 and C_8. The calculations were done for energies 0.2 eV, 0.5 eV, 0.8 eV, 1.0 eV, 1.2 eV and 1.5 eV (see Figures 26 to 28). For each energy the scattering probability with an embedding (i) and without an embedding (ii) is shown together with the error as defined in Equation (65) (iii). When comparing the Figures 26 to 28 (i) with each other one finds the threefold symmetry as explained in Section 6.2) emerging with growing electron energy.

Comparing the scattering amplitudes with (i) and without (ii) embedding in Figures 26 to 28 it is clear that the error made by embedding the defects is rather small compared to the total scattering amplitude. How small the error is can be seen in (iii) of Figures 26

to 28 when comparing the absolute difference with typical scattering amplitudes at the distance of the defect. For energies between 0.2 eV and 1.0 eV the maximal difference in scattering amplitudes lies within 1-5 % while it strongly increases for electron energies above 1.2 eV yielding a maximal relative error of 35 % . The reason for a larger error at higher energies can be easily understood by comparing the band structures in Figure 17 for third NN set and for higher NN sets. The band structure of the third NN approximation and higher NN sets differ strongly at energies above the optimization range and therefore the scattering at the transition between curtains strongly increases. Due to the small error for energies below 1.2 eV no differences in the scattering plots with and without embedding can be seen. At 1.2 eV (Figure 28 a) a minor change of the scattering pattern can be recognized and for 1.5 eV a strong perturbation due to the embedded structure becomes apparent.

When testing the embedding technique on perfect lattice embedding one finds that the embedding technique causes only small but energy dependent errors. Therefore we can define two criteria that must be satisfied in order for the embedding technique to be applicable.

- The perturbation caused by a defect structure must be much (about one magnitude) larger than the perturbation caused by perfect lattice embedding.

- The embedding technique is applicable only up to electron energies of 1.2eV. As explained above this is due to the large perturbation caused by the embedding technique for large energies (Figure 28 b). This is not really a restriction as the tight-binding model for 3NN also fails at higher energies because at higher energies the third order tight-binding approximation also does not resemble the real band structure appropriately.
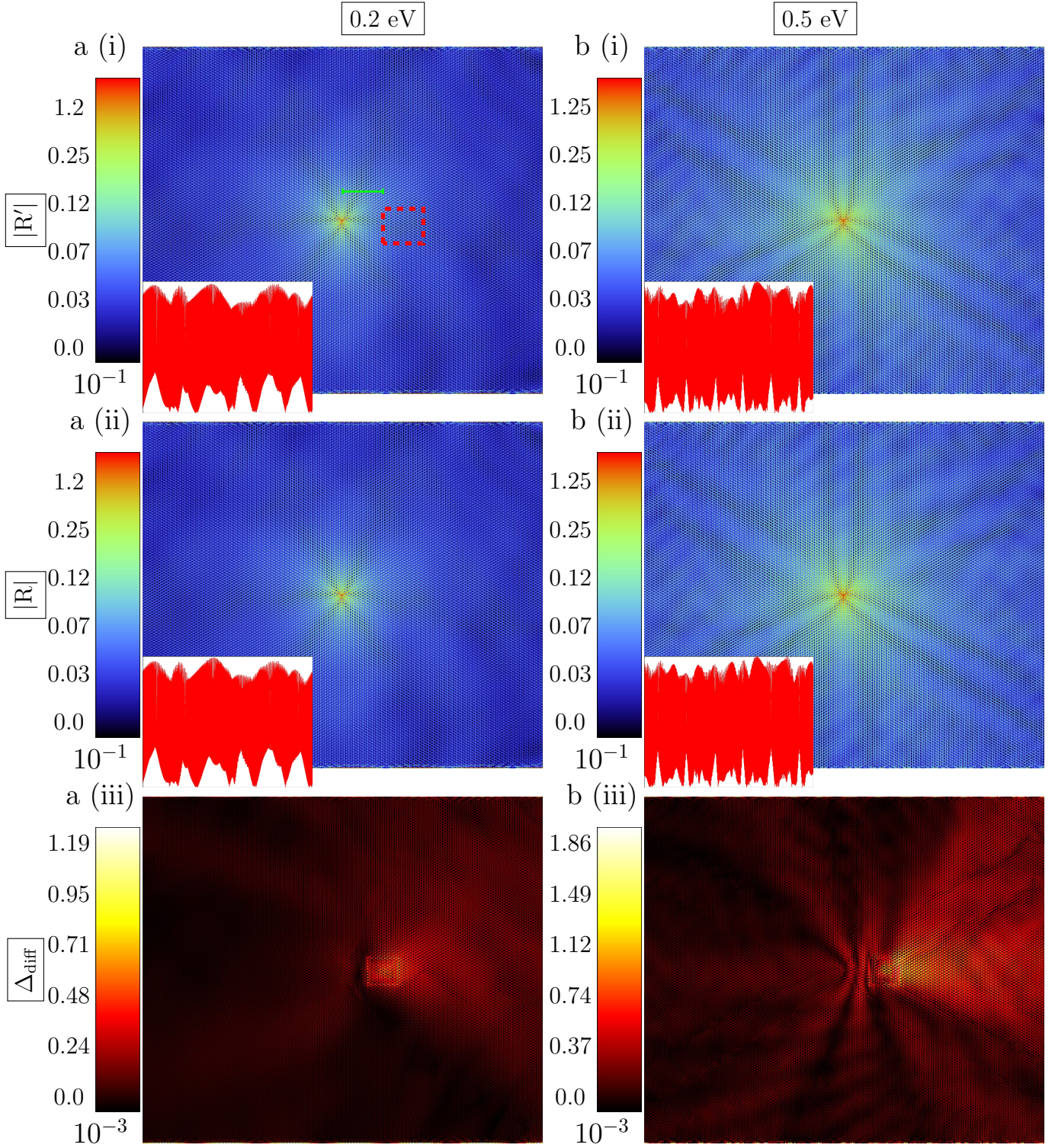
Figure 26: Scattering states at 0.2eV and 0.5eV. In (i) defect free scattering amplitudes are plotted in (ii) scattering amplitudes of perfect lattice embedding are shown. (iii) shows the difference in scattering amplitudes as shown in Equation (65). The bottom left insets in (i) and (ii) show the angle resolved scattering amplitudes with angle and axes as defined in Figure 24.

Between (i) and (ii) no difference can be seen, in (iii) we find that the error for these low energies is small compared to the total scattering amplitudes. In a (i) the position, shape and distance of the embedded structure to the excitation position is shown.
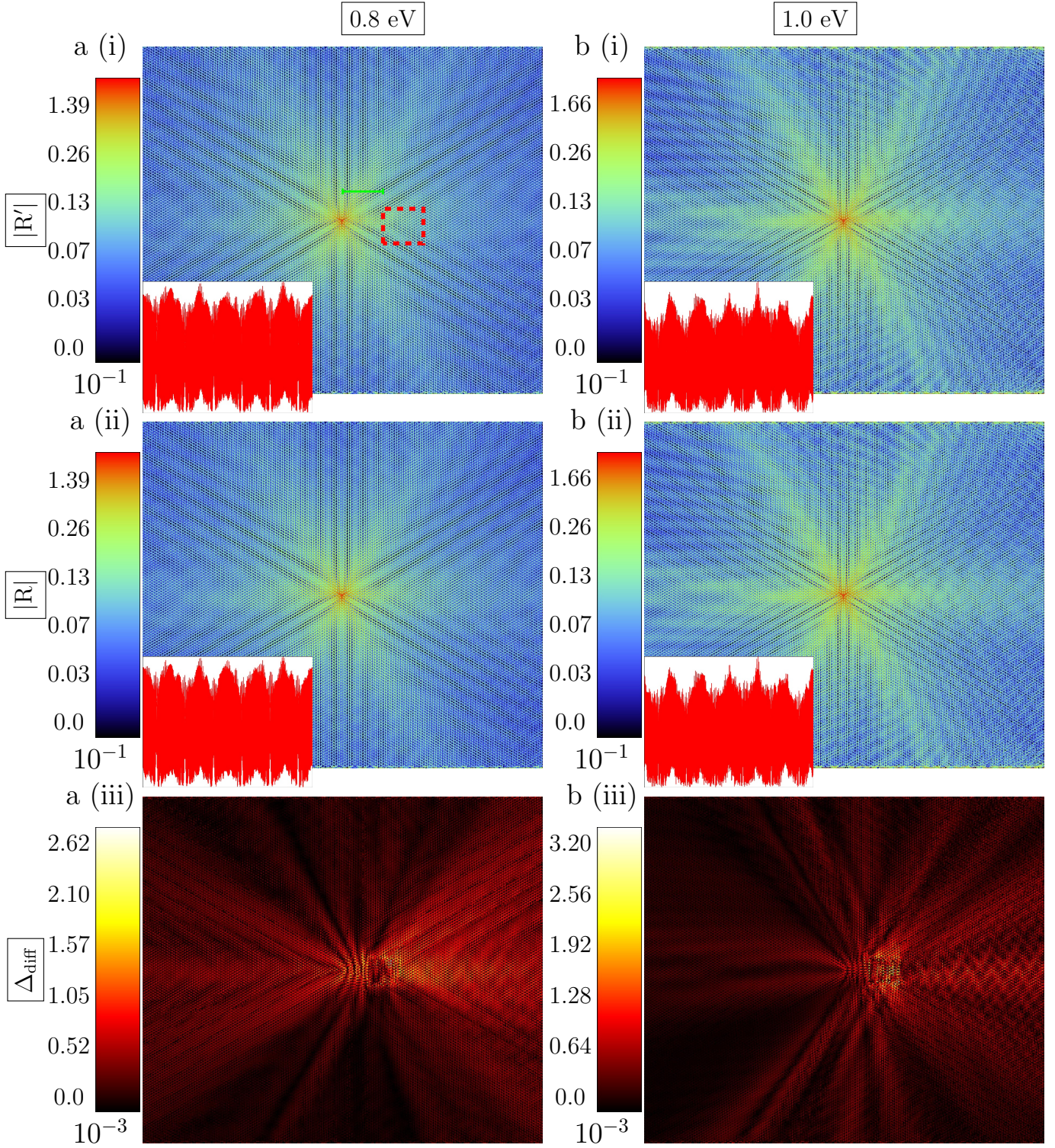
Figure 27: Scattering states at 0.8eV and 1.0eV. In (i) defect free scattering amplitudes are plotted in (ii) scattering amplitudes of perfect lattice embedding are shown. (iii) shows the difference in scattering amplitudes as shown in Equation (65). The bottom left insets in (i) and (ii) show the angle resolved scattering amplitudes with angle and axes as defined in Figure 24.

Between (i) and (ii) no difference can be seen, in (iii) we find that the error for these electron energies is small compared to the total scattering amplitudes. In a (i) the position and shape of the embedded structure relative to the excitation position is shown.
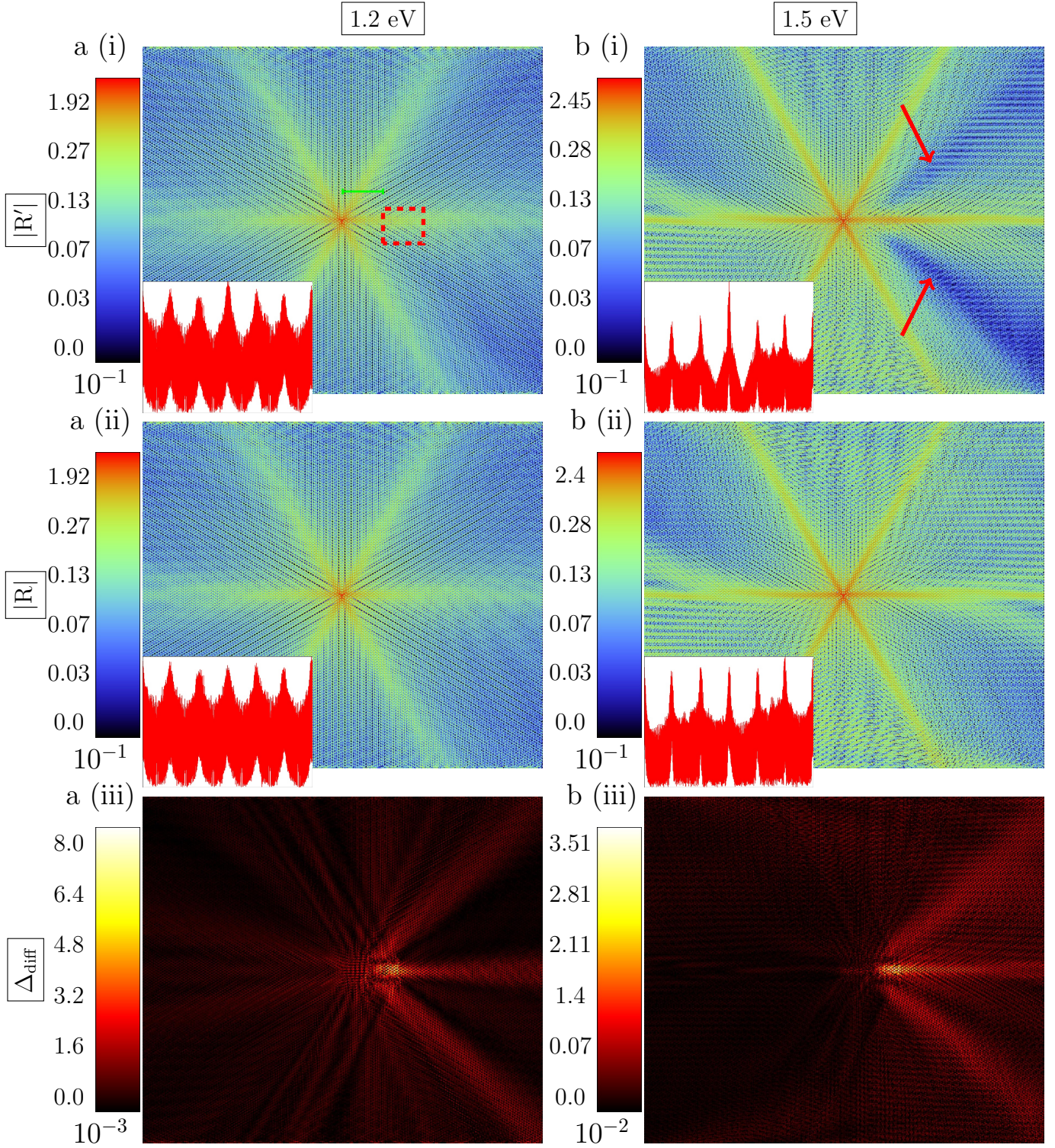
Figure 28: Scattering states at 1.2eV and 1.5eV. In (i) defect free scattering amplitudes are plotted in (ii) scattering amplitudes of perfect lattice embedding are shown. (iii) shows the difference in scattering amplitudes as shown in Equation (65). The bottom left insets in (i) and (ii) show the angle resolved scattering amplitudes with angle and axes as defined in Figure 24.

When comparing a(i) and a(ii) one finds that small differences due to the larger embedding error found in a(iii) can be found. These differences become very prominent for even higher energies as can be seen when looking at b (iii) and by comparing the angle resolved plots in b (i) and b (ii). In b (i) the strongly differing areas are indicated by red arrows.

7 Defect embedding

After having established the error concepts for the presented embedding technique (Section 6.3), this embedding technique can now be applied for scattering at different defect structures. We use the same setup for the curtains as discussed in Section 6.3 and placed the embedded structure 34Å to the right of the STM contact tip (see red arrows in Figures 29 to 32). The embedded structures consist of the defects calculated in Section 5 and the surrounding curtains calculated in Section 4. To investigate scattering at defects a number of parameters can be varied, such as the tip-defect distance, the angle of the tip-defect line relative to the lattice orientation and the energy. Of these parameters, the electron energy is of particular interest. We investigated therefore electron scattering at various defect structures for different electron energies.

7.1 Stone-Wales defect

We found that the Stone-Wales defect has only very little influence on the total scattering behavior in all investigated energy regimes (see Figure 29). For very low energies the embedding technique causes a rather large error, as the perturbation due to the defect is only slightly larger than the perturbation caused due to the embedding technique (see Figure 29 a (ii)). In Figure 29 a (ii) the rectangular shape of the embedded region becomes apparent. Even for 1.2 eV and therefore very pronounced preferred scattering directions the influence of the defect on the total scattering amplitudes is small compared to other defects.

7.2 Flower defect

Of all investigated defects this defect structure features the most pronounced influence onto the scattering amplitudes. The perturbation caused by the defect is -at all investigated energies- one order of magnitude larger than the perturbation due to embedding. Therefore the embedding technique works very well for this defect structure (see Figure 30).

At low energies (0.2 eV and 0.5 eV) we found that a localized state in and around the defect emerges (see Figure 30 a (i) and b (i)). By a localized state we mean that large scatter amplitudes in the orbits in and around the defect structure where found, this is equivalent to a large probability of the electrons to scatter into orbitals around the defect. A localized state at the flower defect was already observed in [13] using DFT calculations. This result provides further proof of the validity of the embedding technique and an interesting feature worth further investigation.

For higher energies (0.8 eV, 1.0 eV and 1.2 eV) another property of scattering at the defect emerges. The backscattering from the defect seems to develop a threefold symmetry just as the perfect lattice scattering has (see Figure 30 b (i), c (i) and c (ii)). An explanation for this behavior is the threefold symmetry of the defect itself.
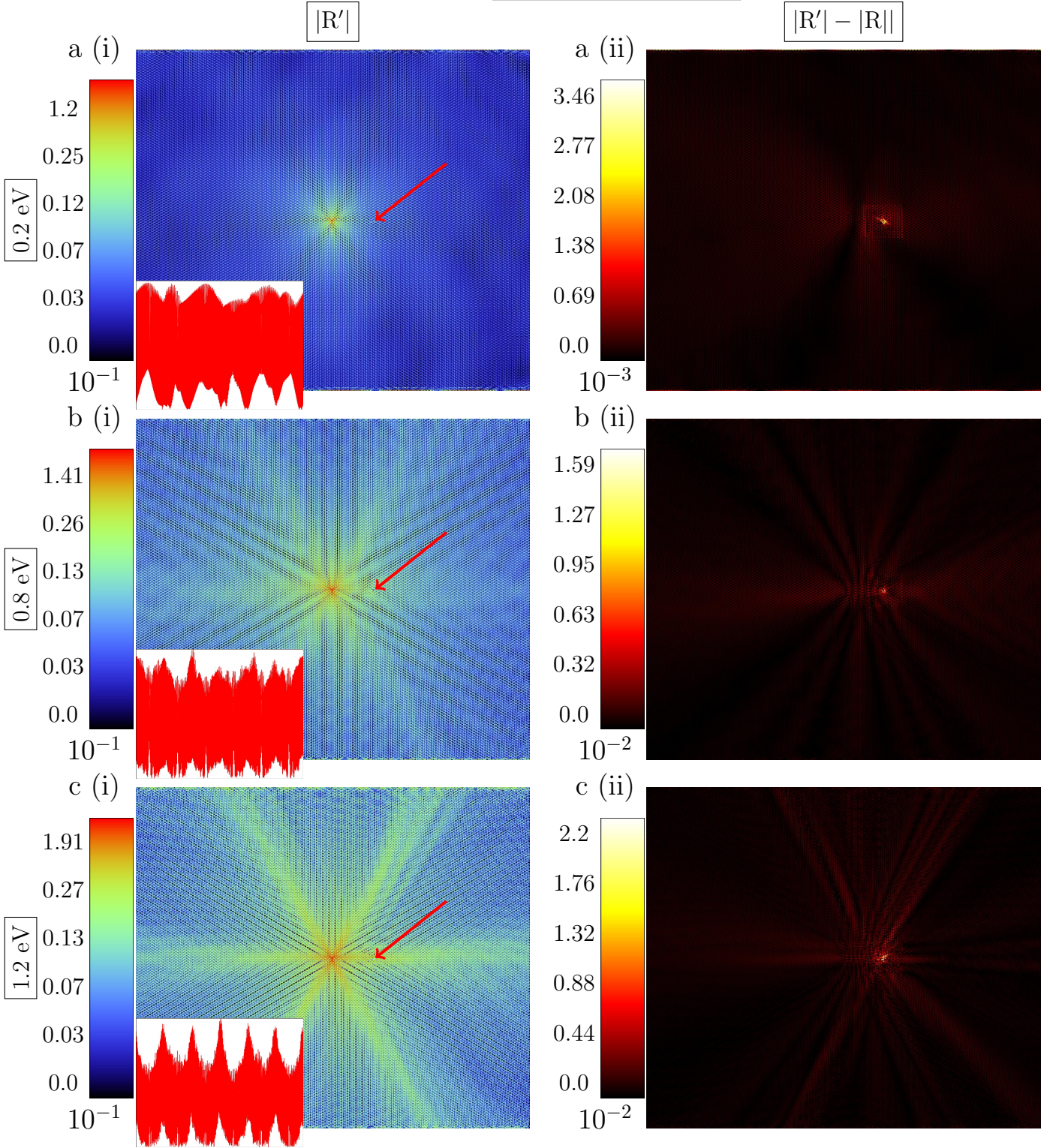
Figure 29: Scattering amplitudes (i) and deviation from the scattering pattern of the defect free lattice (ii) for an embedded Stone-Wales defect at three different energies. $|R'|$ and $||R'| - |R||$ as defined in Equation (65). The defect position is marked by a red arrow. The nested plot in (i) show the angle resolved scattering amplitudes with axes and angle defined as in Figure 24.

For 0.2 eV the embedding technique is not very accurate as the perturbation caused by the defect is not much larger than the perturbation caused by the embedding (compare Figure 26 c (i) with a (ii) of this figure). For 1.2 eV the defect only causes slight scattering.
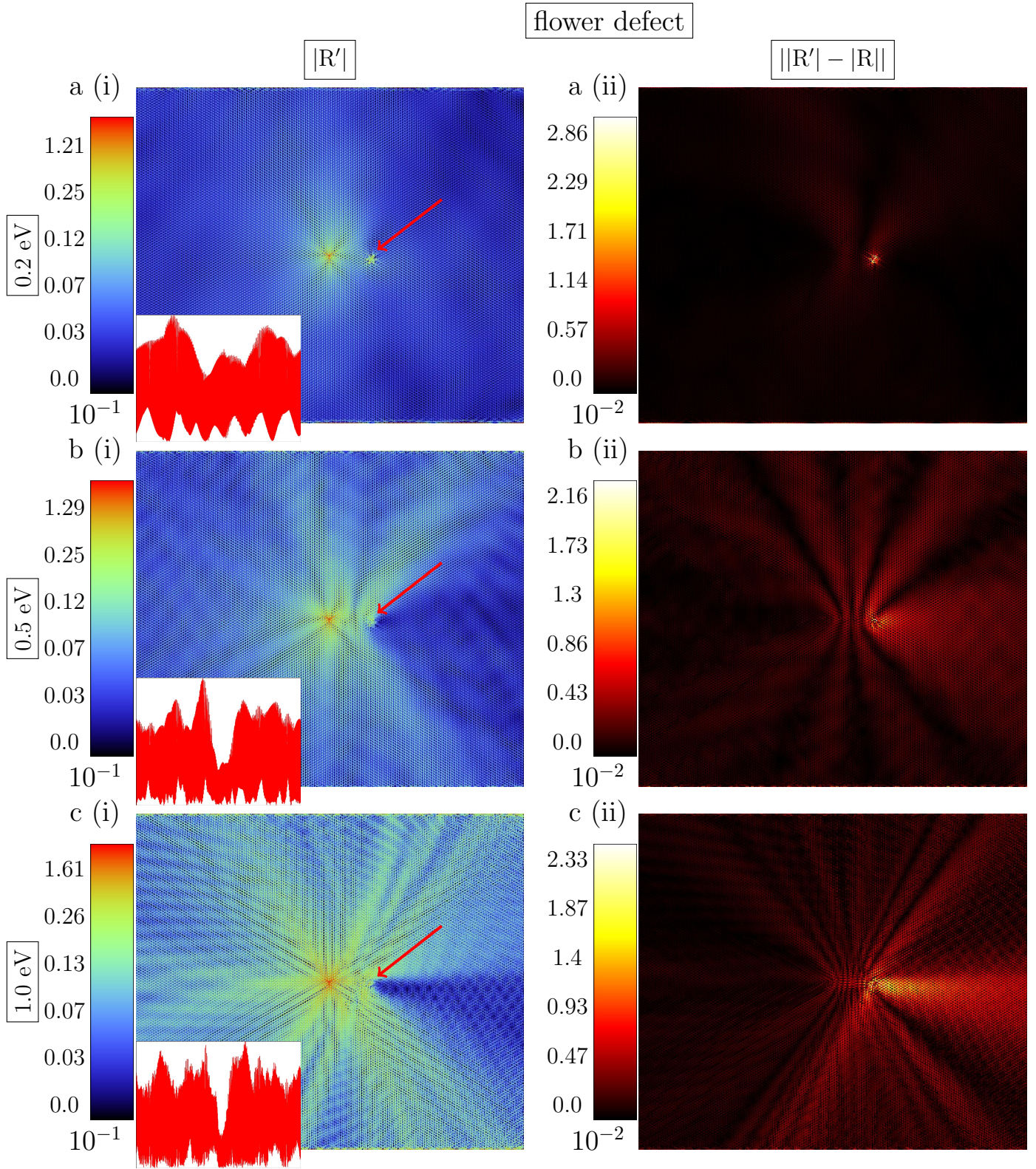
Figure 30: Scattering amplitudes (i) and deviation from the scattering pattern of the defect free lattice (ii) for an embedded flower defect at three different energies. $|R'|$ and $||R'| - |R||$ as defined in Equation (65). The defect position is marked by a red arrow. The bottom left insets in (i) show the angle resolved scattering amplitudes with axes and angle defined as in Figure 24.

The embedding technique is applicable for all investigated energies as the perturbation caused by the defect is much larger than the perturbation caused by the embedding technique. The defect position is marked by a red arrow. In a(i) and b(i) a localized state around the defect can be identified.

7.3 Si Substitute

The replacement of a carbon atom by a Si atom in the lattice leads to surprisingly strong backscattering (see Figure 31 (i)). For the entire investigated energy range the perturbation caused by the substitution defect is far larger than the perturbation caused by the embedding. Therefore the embedding technique is applicable in the entire energy range.

The reason for the rather strong influence on the scattering behavior is unclear as the geometrical lattice expansion (as shown in Figure 21) is small compared to other investigated defects. This could be subject to further investigations.

At 1.2 eV a threefold symmetry with three pronounced scattering directions emerges. The incident electron beam gets strongly scattered at the defect structure where two directions of backscattering emerge (see the two horizontal arrows in Figure 31 c(ii)). The preferred directions of backscattering can be explained by the symmetry of the defect structure.

7.4 Double Vacancy

We found that the influence of the double vacancy on the total scattering pattern is very small. An argument that supports this observation is that the two sublattices of graphene are disturbed the same way. Even though the defect structure opens up a band-gap it conserves AB sub-lattice symmetry and therefore conserves the pseudo-spin in graphene [43]. The conserved pseudo-spin causes strongly suppressed backscattering at the defect structure [43]. Due to the small influence of the defect the embedding method performs rather poorly for low electron energies (see Figure 32 a (ii)). Nevertheless starting from 0.5eV the embedding gives reasonable results and the vacancy hardly changes the scattering pattern. Only for 1.2eV a slight change can be found (see Figure 32 c (ii)).
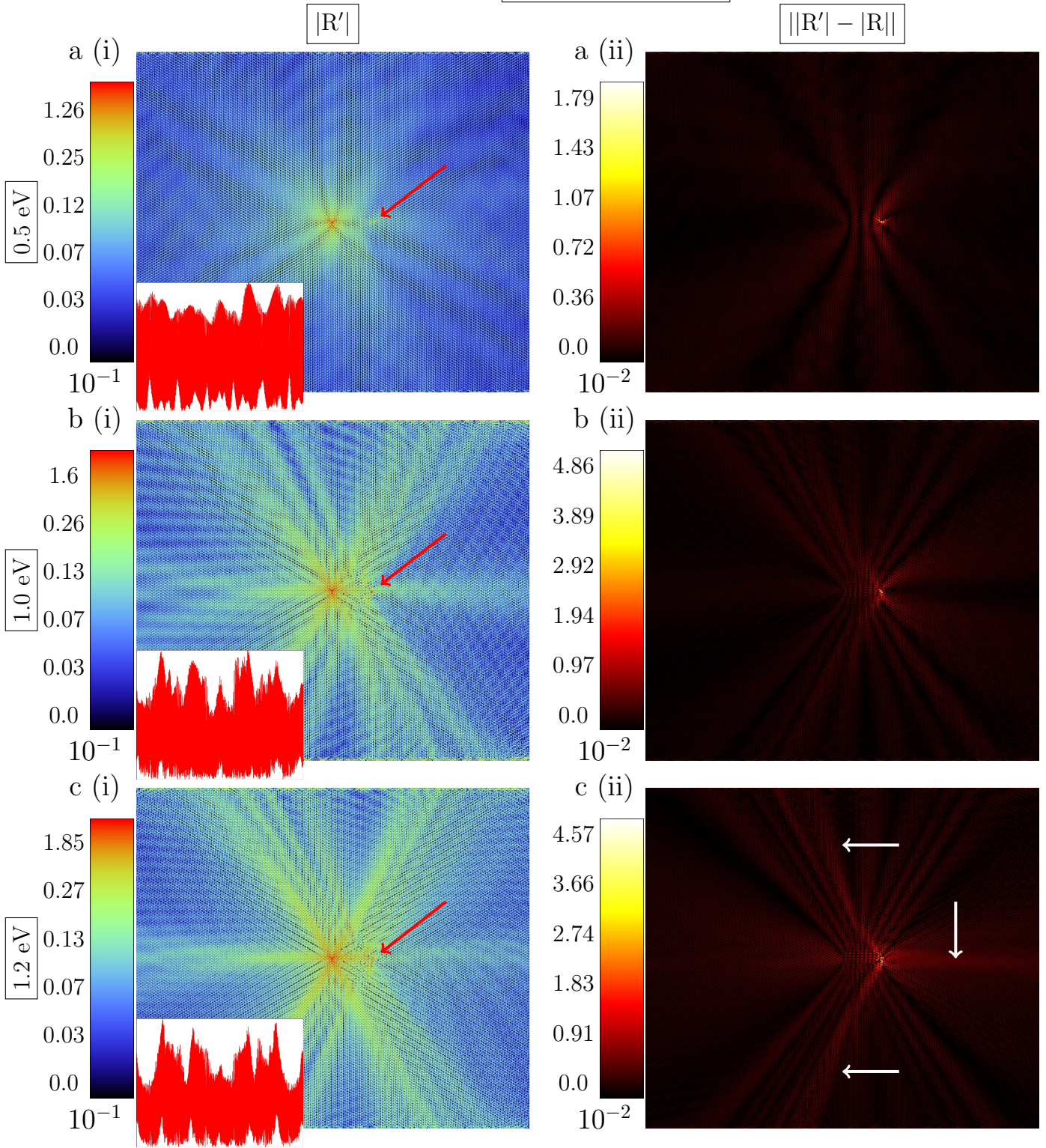
Figure 31: Scattering amplitudes (i) and deviation from the scattering pattern of the defect free lattice (ii) for an embedded silicon interstitial at three different energies. $|R'|$ and $||R'| - |R||$ as defined in Equation (65). The defect position is marked by a red arrow. The bottom left insets in (i) show the angle resolved scattering amplitudes with axes and angle defined as in Figure 24.

For 0.2 eV the embedding technique is not very accurate, as the perturbation caused by the defect is not much larger than the perturbation caused by the embedding (compare Figure 26 c (i) with a (ii) of this figure). For 1.2 eV the defect only causes slight scattering. The defect position is marked by a red arrow.

54
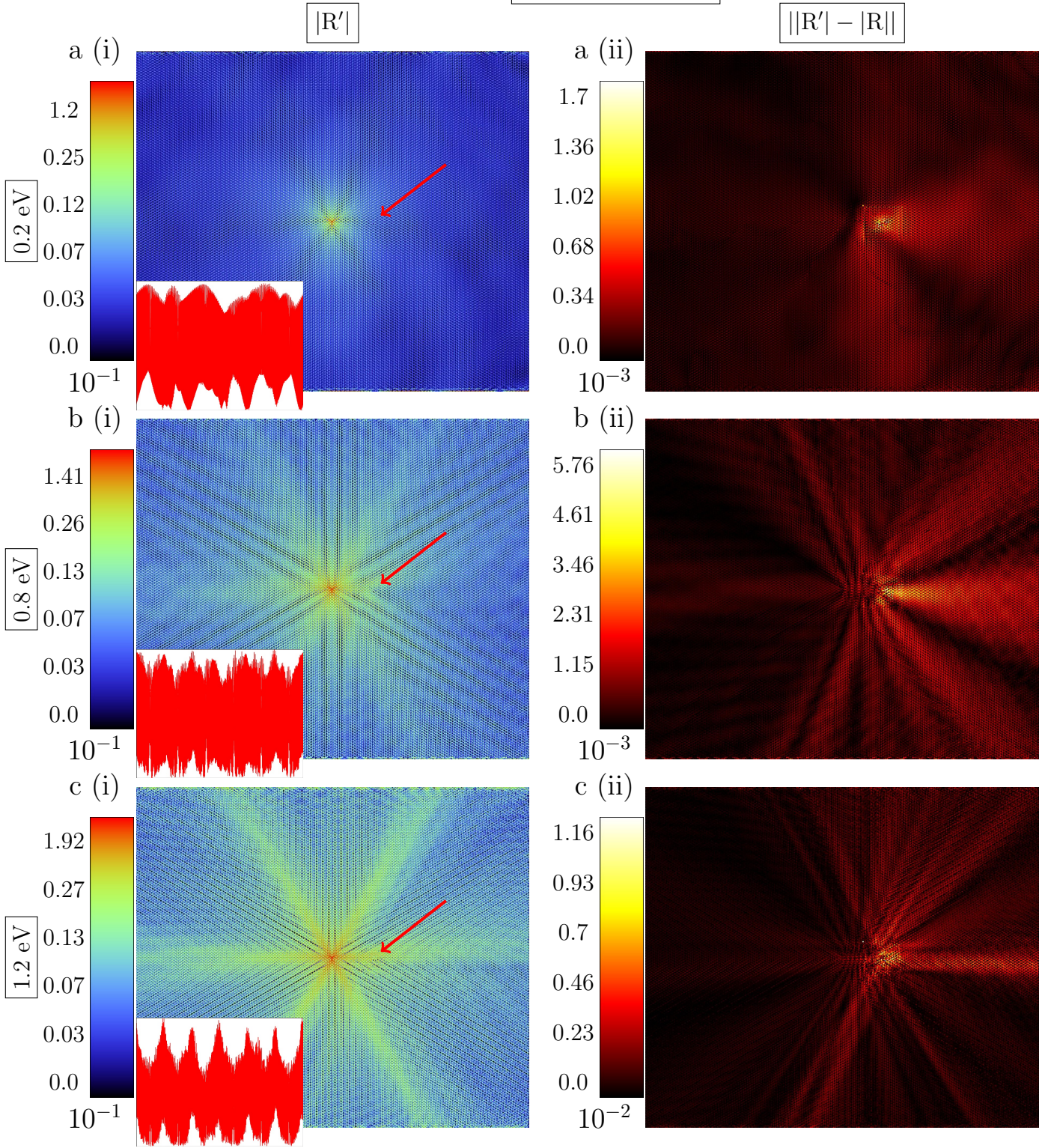
Figure 32: Scattering amplitudes (i) and deviation from the scattering pattern of the defect free lattice (ii) for an embedded double vacancy at three different energies. $|R'|$ and $||R'|-|R||$ as defined in Equation (65). The defect position is marked by a red arrow. The bottom left insets in (i) show the angle resolved scattering amplitudes with axes and angle defined as in Figure 24.

For 0.2 eV the embedding technique is not very accurate as the perturbation caused by the defect is not much larger than the perturbation caused by the embedding (compare Figure 26 c (i) with a (ii) of this figure). For 1.2 eV the defect only causes slight scattering.

7.5 Conclusion

While the flower defect causes massive backscattering of incident electrons the Stone-Wales defect and the double vacancy hardly cause any scattering at all. The silicon interstitial leads to a backscattering at the structure that is surprisingly strong, considering the geometrical extension of the defect.

We currently do not have an explanation for the localized state at low energies around the flower defect. While the strongly suppressed backscattering at the double defect could be explained with conservation of pseudo-spin, the reason for the very small influence of the Stone-Wales defect must lie in a different argument.

For defects with little influence on the scattering at low energies (0.2-0.5 eV) the established embedding method is applicable but not very accurate. At higher energies the influence of the defect on the total scattering pattern increases leading to a more accurate description of defect scattering in graphene. For defects with larger influence on the scattering pattern (e.g. flower and silicon interstitial) the embedding technique is accurate in the entire energy regime.

8 Summary

The aim of this thesis was to contribute to the understanding of defects in graphene. We successfully established, implemented, and tested an embedding technique to simulate transport through large graphene lattices with defects and used it to simulate transport with a variety of different defect structures. We use a Green's functions method to calculate large lattice structures in the tight-binding formalism. We include defect structures, consisting of a rearrangement of the atoms around the defect and a corresponding change in tight-binding parameters, in these large lattices via an embedding technique. We use density functional theory (DFT) to obtain an accurate defect description while the computational effort of describing embedded defects via tight-binding remains reasonable. The embedding technique surrounds a structure relaxed via DFT with a transition area consisting of several layers of atomic lattice sites. Tight-binding parameters in the transition region smoothly connect the high-order description around the defect with the bulk lattice parameters. We tested this method by embedding defect free structures and found that the embedding technique is valid. An experimental setup currently used at the University of Vienna serves as a template to shape our simulations, with this approach we hope to predict some results of these measurements.

We find preferred scattering directions for electrons induced by a STM tip. These preferred scattering directions could be explained analytically via trigonal warping and interference effects of wavefunctions. Testing the embedding technique on the setup we found that the gradual change of NN parameters in the transition region causes only small errors in the scattering patterns and is therefore applicable for embedding defect structures.

After these benchmark calculations we apply our embedding technique to a number of different defect structures to determine their influence on the local transport properties. We obtain a high-level description of defect structures using DFT calculations on large super cells. A basis transformation of these calculations into maximally localized Wannier orbitals yields tight-binding parameters of the defect structure.

We consider flower and Stone Wales defects, vacancies and silicon substitutes. While Stone Wales and double vacancy defects only slightly change the scattering behavior of the electrons, the larger flower defect massively influences the scattering behavior. Quite interestingly also the geometrically rather small silicon substitution defect caused a large perturbation of the scattering pattern. We also observed pronounced localized states at the defect structure for flower defects at low electron energies.

9 Outlook

Future work based on this thesis could extend our results in various directions.

- Comparison with the discussed experiment,

- applying the embedding method to additional defect structures,

- improving the embedding technique itself,

- considering additional degrees of freedom of the lattice (e.g. electron-phonon interactions)

- Developing a Green's function method based on tenth NN coupling everywhere making the embedding obsolete.

The embedding model could also be extended to larger defect structures, e.g. extended one-dimensional topological defects spanning the whole lattice. One example would be grain boundaries on epitaxially grown graphene where flakes that grow with different orientation touch. Such defects are very common and up to this date not well understood.

One obvious next step will be to compare the results obtained in this thesis with the experimental data from the experiment discussed in Section 6.

An improvement of the embedding technique could be obtained by finding NN parameter sets that blend smoothly into each other. One possible way of realizing this would be limiting the optimization parameter space to a subset where the NN parameters are smoothly transformed via Lagrange multipliers.

During the discussion some simplifications were applied to make large systems treatable with modern computational capacities. One very drastic simplification was neglecting electron phonon interactions. When N phonons per atomic lattice site are considered the tight-binding Hamiltonian would be N times larger leading to a massive increase in computational effort. Promising work is currently done to reduce the number of basis elements that need to be considered in the phonon-electron interaction bringing such treatment within reach.

Finally one could think of a variation of the currently implemented method of calculating the Green's function. Instead of proceeding slice by slice one could calculate three slices at a time. While this would massively increase the computational effort it would also make the embedding obsolete, as the lattice can be treated naturally in the tenth nearest neighbor approximation.

In conclusion we can say that there is a lot left for investigation providing promising research topics for the next years.

A   DFT defect structure parameters

A.1   Stone-Wales defect

	0	1	2	3	4	10	11	12	13	14	25	20	21	42	43
0	0.1947	-2.8953	0.2034	0.0583	0.0417	0.1969	-0.2593	0.0437	-0.0100	-0.0411	-0.0269	-0.0068	0.0096		
1	-2.8953	0.2538	-2.9047	0.1160	-0.2585	-0.2756	0.2541	0.0268	0.0629	0.0640	-0.0106	-0.0280	-0.0335		
2	0.2034	-2.9047	0.2882	-3.0600	0.3420	0.1554	-2.9393	0.1615	-0.3205	0.2341	0.0422	0.0638	0.0654		
3	0.0583	0.1160	-3.0600	0.3188	-3.1530	0.0324	0.2723	-0.2149	0.2602	-3.1975	0.0022	0.0322	0.1447		
4	0.0417	-0.2585	0.3420	-3.1530	0.3694	-0.0177	-0.0159	0.0308	0.0430	0.1423	0.0028	-0.0095	-0.0481		
5	-0.0142	0.0425	-0.0143	0.2721	-2.9470	0.0032	0.0016	-0.0134	0.0972	-0.3507	-0.0108	-0.0016	-0.0481	0.0005	0.0007
6	-0.0046	0.0073	0.0306	-0.2125	0.2720	0.0027	-0.0193	-0.0436	0.0290	0.2483		0.0300	0.1447	0.0070	-0.0065
7	0.0030	-0.0049	-0.0073	0.0306	-0.0143	-0.0006	0.0054	0.0264	-0.0552	0.0241		-0.0144	0.0654		
8		0.0007	-0.0049	0.0073	0.0425		0.0023	-0.0119	0.0242	-0.0342			-0.0335		
9			0.0030	-0.0046	-0.0142				-0.0056	0.0141			0.0096		
10	0.1969	-0.2756	0.1554	0.0324	-0.0177	0.2047	-2.7537	0.2656	0.0047	0.0492	0.2059	-0.2653	-0.0158		
11	-0.2593	0.2541	-2.9393	0.2723	-0.0159	-2.7537	0.2244	-2.7548	0.2016	-0.3005	-0.2603	0.1077	0.0018		
12	0.0437	0.0268	0.1615	-0.2149	0.0308	0.2656	-2.7548	0.1243	-2.6565	0.1196	0.2087	-2.7663	0.3679		
13	-0.0100	0.0629	-0.3205	0.2602	0.0430	0.0047	0.2016	-2.6565	0.3600	-3.0570	0.0157	0.2116	-2.6558		
14	-0.0411	0.0640	0.2341	-3.1975	0.1423	0.0492	0.0767	0.1196	-3.0570	0.3202	0.0196	0.0480	-0.4083		
15	0.0141	-0.0341	0.0241	0.2484	-0.3507	-0.0235	-0.0314	0.0671	0.1606	-2.9286	-0.0292	-0.0592	-0.4082		
16	-0.0056	0.0242	-0.0551	0.0290	0.0972	0.0157	0.0080	-0.0513	0.1549	0.1605	0.0164	0.0423	-2.6558		
17		-0.0119	0.0264	-0.0436	-0.0134	-0.0047	-0.0169	0.0112	-0.0513	0.0672	-0.0115	-0.0134	0.3680		
18		0.0023	0.0054	-0.0193	0.0017			0.0080	-0.0314	0.0767	0.0044	0.0041	0.0018		
19			-0.0006	0.0027	0.0032			-0.0047	0.0157	-0.0235			-0.0158		
20	-0.0269	-0.0106	0.0422	-0.0082	0.0022	0.2059	-0.2603	0.2087	0.0157	-0.0292	0.1952	-2.5731	0.0164	0.0038	-0.0024
21	-0.0068	-0.0280	0.0638	0.0322	-0.0095	-0.2653	0.1077	-2.7663	0.2116	0.0480	-2.5731	0.1728	-0.0985	0.0092	-0.0049
22	0.0023	0.0112	-0.0349	-0.0314	0.0115	0.0579	0.0523	0.1428	-0.1357	0.0485	0.2087	-2.7663	-0.0366	-0.0219	0.0038
23	0.0001	-0.0156	0.0347	-0.0196	0.0102	-0.0246	0.0247	-0.1357	-0.3116	0.1034	0.0157	0.2116	0.0939	-0.0249	-0.0328
24	-0.0013	0.0089	-0.0059	-0.0942	0.0201	0.0221	-0.0198	-0.0366	0.0939	0.2115	0.0164	-0.0985	-3.3475	-0.0013	0.0082
25	0.0096	-0.0335	0.0654	0.1447	-0.0481	-0.0158	0.0018	0.3679	-2.6558	-0.4083	0.0164	0.0423	0.1032	0.0054	-0.0016
26		0.0024	-0.0103	0.0529	-0.0218	-0.0084	0.0072	-0.0018	0.1080	-0.1287	-0.0115	-0.0134	0.0939	0.0069	-0.0353
27			-0.0014	-0.0079	-0.0072		0.0076	-0.0130	-0.0018	0.0166	0.0044	0.0179	-0.0366	0.0048	0.0035
28			-0.0144	0.0300	-0.0016		0.0041	-0.0134	0.0423	-0.0593			-0.0985		0.0011
29				-0.0108	0.0028			0.0044	-0.0115	0.0196			0.0164		
30	-0.0020	0.0025	0.0023	-0.0074		-0.0239	-0.0107	0.0579	-0.0246	0.0040	-0.0269	-0.2653	0.0221	0.0546	-0.0077
31	0.0020	-0.0038	0.0122	0.0090		-0.0107	-0.0305	0.0523	0.0247	-0.0129	-0.0106	0.1077	-0.0198	0.0023	0.0524
32			-0.0094	0.0050		0.0023	0.0122	-0.0349	0.0347	-0.0159	0.0038	0.0638	-0.0058	0.2692	-0.2781
33			0.0050	-0.0083		-0.0074	0.0090	-0.0313	-0.0196	0.0271	-0.0024	0.0322	-0.0942	-0.3125	0.1502
34			-0.0159	0.0271	-0.0094	0.0040	-0.0129	0.0485	0.1033	-0.0818	0.0021	0.0480	0.2115	0.0681	0.0703
35			0.0133	-0.0188	0.0083	0.0032	-0.0026	0.0166	-0.1287	0.0564	0.0028	-0.0592	0.2115	-0.0249	0.0680
36							0.0003	-0.0079	0.0529	-0.0188		0.0300	-0.0941	-0.0230	0.0169
37								-0.0014	-0.0103	0.0134		-0.0144	-0.0059	0.0081	-0.0101
38				0.0003				0.0076	0.0072	-0.0026		0.0040	-0.0198	0.0011	-0.0005
39									-0.0083	0.0032			0.0221		0.0009
40						-0.0020	0.0020	0.0023	0.0001			-0.0068	-0.0013	0.1926	0.0434
41						0.0025	-0.0038	0.0112	-0.0156			-0.0280	0.0089	-2.9128	0.1890
42								0.0005	0.0070			0.0092	0.0054	0.3099	-2.9139
43								0.0007	-0.0065			-0.0049	-0.0016	-2.9139	0.3098
44							-0.0041	0.0115	0.0102	-0.0094		-0.0095	0.0201	0.2507	-2.8941
45								-0.0072	-0.0218	0.0083		-0.0016	0.0201	0.0144	0.2247
46												0.0011	-0.0016	0.0622	-0.2965
47													0.0053	-0.0223	0.0622
48									0.0024				0.0089	0.0013	-0.0119
49													-0.0013	0.0012	0.0014

Table 3: Defect parameters of the Stone-Wales defect, with atoms as numbered in Figure 18.

A.2 Double vacancy

	0	1	2	3	4	5	6	12	13	14	15	16	17	18	24	25	26	27
0	0.3912	-2.8888	0.2232	0.0150	0.0517	-0.0195	0.0030	0.2021	-0.2655	0.0497	-0.0128	-0.0140	0.0042	-0.0009	-0.0186	-0.0112	0.0038	-0.0043
1	-2.8888	0.3905	-2.8817	0.2345	-0.2674	0.0491	-0.0144	-0.2671	0.2033	0.0244	0.0492	0.0118	-0.0115	0.0029	-0.0109	-0.0191	0.0066	0.0023
2	0.2232	-2.8817	0.3933	-2.8774	0.1868	0.0321	0.0565	0.2234	-2.9032	0.2123	-0.2625	0.2227	0.0022	-0.0082	0.0502	0.0265	-0.0200	-0.0113
3	0.0150	0.2345	-2.8774	0.3895	-2.8794	0.1910	0.1822	0.0215	0.0292	0.0504	0.1962	0.2168	-0.2177	0.0357	-0.0130	0.0514	-0.0102	-0.0237
4	0.0517	-0.2674	0.1868	-2.8794	0.3602	-2.8543	-2.7026	-0.0190	-0.0207	-0.0120	0.0237	-0.2545	0.2648	-0.0184	0.0037	-0.0204	0.0032	0.0070
5	-0.0195	0.0491	0.0321	0.1910	-2.8543	0.3592	-2.7026	0.0062	-0.0207	-0.0120	0.0487	0.0795	-2.6928	0.2556	0.0043	-0.0048	0.0057	-0.0178
6	0.0030	-0.0144	0.0565	0.1822	-2.7026	-2.8572	0.1744	0.0014	0.0016	0.0086	0.0565	0.0603	0.1657	-0.1999	-0.0017	0.0057	0.0025	-0.0221
7	-0.0002	0.0036	-0.0215	0.0496	0.0353	0.1703	0.0339	-0.0001		-0.0020	-0.0322	0.0055	0.0297	0.0367			0.0025	0.0000
8		-0.0040	0.0025	-0.0109	0.0551	-0.2805	0.0491				0.0075	0.0037	-0.0195	-0.0040				0.0012
9			-0.0004	0.0032	0.0031	0.0550	-0.0212				-0.0022	-0.0004	-0.0164	-0.0139				
10				-0.0049	-0.0004	-0.0106	0.0014				0.0014		0.0041	0.0033				
11						0.0024												
12	0.2021	-0.2671	0.2234	0.0215	-0.0190	0.0062	-0.0077	0.4295	-2.9182	0.2213	0.0191	0.0507	-0.0189	0.0027	0.2205	-0.2797	0.0537	-0.0131
13	-0.2655	0.2033	-2.9032	0.2110	-0.0207	-0.0207	-0.0226	-2.9182	0.4287	-2.9225	0.2292	-0.2637	0.0489	-0.0139	-0.2738	0.2124	0.0184	0.0577
14	0.0497	0.0244	0.2123	-0.2703	-0.0120	-0.0120	0.0565	0.2213	-2.9225	0.4751	-2.9188	0.2167	0.0280	0.0491	0.2442	-2.9607	0.2502	-0.2956
15	-0.0128	0.0492	-0.2625	0.1962	0.0237	0.0487	0.0795	0.0191	0.2292	-2.9188	0.4675	-2.9369	0.1813	-0.2445	0.0226	0.2072	-0.2629	0.1738
16	-0.0140	0.0118	0.2227	0.2693	-0.2545	0.2648	-2.6928	0.0507	-0.2637	0.2167	-2.9369	0.3790	-2.8551	0.1935	-0.0207	0.0278	0.0454	0.0430
17	0.0042	-0.0115	0.0022	0.2168	0.2648	-0.0184	0.2556	-0.0189	0.0489	0.0280	0.1813	-2.8551	0.3486	-2.4942	0.0067	-0.0201	-0.0121	0.0521
18	-0.0009	0.0029	-0.0082	-0.0148	-0.0184	0.0371	-0.2013	0.0027	-0.0139	0.0491	-0.2445	0.1935	-2.4942	-2.6914	0.0012	-0.0030	-0.0424	0.1115
19		-0.0016	0.0034	-0.0162	-0.0037	0.0313	0.1632	-0.0001	0.0033	-0.0185	0.0404	0.0359	0.1191	0.1262		0.0006	0.0150	-0.0471
20		0.0012	0.0041	0.0035	-0.0201	-0.0232	0.0615		-0.0037	0.0014	-0.0090	0.0579	0.0579	0.0331		0.0024	-0.0027	0.0097
21			-0.0003	0.0015	0.0056	0.0076	-0.0328			-0.0005	0.0043	-0.0255	-0.0084	0.0401				-0.0020
22					-0.0022	-0.0020	0.0087				-0.0045	0.0040	0.0012	-0.0183				0.0020
23						0.0007						-0.0004						
24	-0.0186	-0.0109	0.0502	-0.0130	0.0037	0.0043	-0.0017	0.2205	-0.2738	0.2442	0.0226	-0.0207	0.0067	0.0012	0.4860	-3.0299	0.1894	0.0464
25	-0.0112	-0.0191	0.0265	0.0514	-0.0204	-0.0048	0.0057	-0.2797	0.2124	-2.9607	0.2072	0.0278	-0.0201	-0.0030	-3.0299	0.4877	-2.9648	0.1936
26	0.0038	0.0066	-0.0200	-0.0102	0.0032	0.0057	0.0025	0.0537	0.0184	0.2502	-0.2629	0.0454	-0.0121	-0.0424	0.1894	-2.9648	0.5412	-3.1670
27	-0.0043	0.0023	-0.0113	-0.0237	0.0070	-0.0178	-0.0221	-0.0131	0.0151	-0.2956	0.1738	0.0430	0.0521	0.1115	0.0528	-0.2804	0.2721	-2.9576
28	0.0032	-0.0188	0.0019	0.0280	-0.0203	-0.0005	0.0511	-0.0165	-0.0113	0.2284	0.3361	0.2053	-0.2810	0.0004	-0.0231	0.0549	0.0530	0.0399
29	0.0009	0.0050	0.0023	0.0364	-0.0075	-0.0138	-0.0133	0.0052	-0.0004	-0.0072	-0.0184	-0.2159	0.2429	-2.6277		-0.0028	-0.0042	-0.0004
30			-0.0001	0.0057	0.0008	-0.0005	-0.0012			0.0064	-0.0025	-0.0210	0.0327	0.1787			0.0021	-0.0005
31				-0.0018	0.0027	0.0013	-0.0000			-0.0011	0.0030	0.0066	-0.0239	0.0717				0.0070
32							0.0026				0.0020	-0.0020	0.0097	-0.0477				
33													-0.0026	0.0152				
34	-0.0022	0.0010		-0.0038				-0.0149	-0.0148	0.0519	-0.0068	0.0012	0.0019	-0.0031	0.2662	-0.2720	0.1873	0.0471
35	0.0010	-0.0022		0.0035			0.0000	-0.0149	-0.0150	0.0039	0.0488	-0.0199	0.0038	0.0120	-0.2710	0.2753	-2.9630	0.1932
36				0.0010				0.0049	0.0050	-0.0136	-0.0135	0.0043	-0.0051	0.0003	0.0515	0.0035	0.2515	-0.2948
37				-0.0035				-0.0042	0.0040	0.0609	-0.0290	0.0115	0.0018	-0.0103	-0.0067	0.0489	-0.2630	0.1739
38		-0.0001		0.0120	-0.0027	-0.0014	-0.0014	0.0047	-0.0247	-0.0207	0.0554	-0.0370	-0.0157	0.0086	-0.0276	0.0268	0.2716	-2.9583
39				-0.0341	0.0046	0.0006	0.0082	-0.0003	0.0072	0.0004	0.0333	0.0248	-0.0242	0.2427	0.0116	0.0120	0.0533	0.1118
40				0.0118			0.0008		0.0000	0.0014	-0.0104	-0.0050	0.0111	-0.0749	-0.0031	-0.0036	-0.0425	-0.0472
41				0.0031			-0.0018			0.0004	-0.0000	0.0023	-0.0080	0.0405		-0.0001	0.0151	-0.0005
42				-0.0013		0.0028	0.0038				-0.0025	0.0005	0.0115	-0.0715			-0.0042	-0.0004
43							-0.0099				0.0030	0.0006	-0.0050	0.0088			0.0020	0.0019
44							-0.0004						0.0007	-0.0001				
46								-0.0017	0.0001	0.0050	-0.0041				-0.0149	-0.0150	0.0538	-0.0130
47								0.0002	-0.0016	0.0049	0.0040	-0.0008	0.0022		-0.0146	-0.0147	0.0177	0.0575
48										-0.0024	0.0019		-0.0010	0.0030	0.0039	0.0066	-0.0195	-0.0113
49										0.0009	-0.0034			-0.0050	-0.0038	-0.0199	-0.0105	-0.0236
50									-0.0008	0.0043	0.0115	-0.0049		0.0111	0.0011	0.0038	0.0455	0.0426
51										-0.0051	0.0018	0.0022		-0.0018	0.0019	0.0000	-0.0121	0.0524
52											-0.0014			0.0038			0.0026	-0.0223
53													0.0013	-0.0081			0.0024	0.0001
54														0.0023			-0.0027	0.0097
55											0.0007							-0.0020
58															-0.0022	0.0010	0.0038	-0.0043
59															0.0009	-0.0022	0.0065	0.0024
60																	-0.0021	-0.0021
61																-0.0006	0.0016	-0.0022
62																	0.0032	0.0070
63																	-0.0048	0.0058
64																		-0.0011

Table 4: Defect parameters of the Double vacancy with atoms as numbered in Figure 20.

A.3 Flower defect

	0	1	2	16	32	33	34	35	48	49	50	51	52	53	54	55
0	0.4635	-2.8859	0.2239	0.2333	-0.0220	-0.0119	0.0035	-0.0047	-0.0023	0.0017	-0.0018	0.0018	-0.0002	-0.0012	-0.0023	
1	-2.8859	0.4603	-2.9254	-0.2718	-0.0114	-0.0212	0.0077	0.0023	0.0017	-0.0020	0.0010	-0.0033	0.0026	-0.0094	0.0120	
2	0.2239	-2.9254	0.4579	0.2082	0.0509	0.0244	-0.0210	-0.0089	0.0028	0.0071			0.0106		0.0002	
3	0.0230	0.2135	-2.9051	0.0218	-0.0120	0.0485	-0.0129	-0.0191	-0.0049	0.0031			-0.0008		-0.0050	
4	0.0507	-0.2695	0.0266	-0.0185	0.0034	-0.0190	0.0048	0.0061		-0.0007			0.0011		0.0187	
5	-0.0195	0.0486	0.0460	0.0066	0.0024	-0.0003	-0.0028	-0.0023					0.0109		0.0209	-0.0206
6	0.0055	-0.0135	-0.0168	0.0073	-0.0019	0.0096	0.0033	-0.0147					-0.0029	-0.0010	-0.0107	0.0085
7	-0.0012	0.0043	0.0008	-0.0021		-0.0022	0.0013	0.0015		-0.0017				-0.0014	0.0014	-0.0017
8		-0.0041	0.0014					0.0006						-0.0123	-0.0016	
9																
10																-0.0119
11																0.0024
16	0.2333	-0.2718	0.2082	0.4531	0.1927	-0.2656	0.0501	-0.0137	-0.0243	-0.0090	0.0024	-0.0052	0.0047	-0.0012	-0.0082	-0.0079
17	-0.2667	0.2224	-2.8608	-2.8637	-0.2699	0.2113	0.0223	0.0506	-0.0101	-0.0212	0.0082	0.0040	-0.0231	0.0110	0.0184	0.0078
18	0.0485	0.0233	0.2115	0.2159	0.2058	-2.8526	0.2091	-0.2595	0.0496	0.0332	-0.0258	-0.0115	0.0588	-0.0271	-0.0043	0.0031
19	-0.0121	0.0493	-0.2578	0.0175	0.0262	0.2022	-0.2502	0.1749	-0.0122	0.0435	-0.0079	-0.0269	0.0279	0.0223	-0.0240	0.0253
20	-0.0214	0.0297	0.1940	0.0548	-0.0227	0.0388	0.0426	0.0300	0.0024	-0.0160	0.0040	0.0096	-0.0279	0.0201	-0.0422	-0.0553
21	0.0079	-0.0275	0.0515	-0.0222	0.0080	-0.0274	-0.0078	0.0414	0.0007	0.0046	-0.0093	0.0116	-0.0300	0.0015	0.0714	0.0740
22	-0.0020	0.0110	-0.0357	0.0043	0.0028	-0.0090	-0.0296	0.0391	-0.0038	0.0105	0.0102	-0.0253	0.0491	0.0347	0.0790	-0.0281
23		-0.0020	0.0112	-0.0014	0.0020	-0.0030	0.0188	-0.0556		-0.0048	0.0004	0.0048	0.0061	-0.0637	-0.0429	0.0257
24		0.0020	-0.0015			0.0058	-0.0073	0.0237				0.0005	-0.0083	0.0274	0.0092	-0.0314
25			0.0023					-0.0093					0.0042	-0.0087	-0.0350	0.0233
26								0.0042					-0.0065	0.0147	0.0094	-0.0125
27														-0.0042	-0.0021	
28																
32	-0.0220	-0.0114	0.0509	0.1927	0.4378	-2.8632	0.2219	0.0152	0.1854	-0.2801	0.0568	-0.0163	-0.0181	0.0110	-0.0083	-0.0069
33	-0.0119	-0.0212	0.0244	-0.2656	-2.8632	0.4397	-2.8451	0.2218	-0.2702	0.1779	0.0283	0.0572	0.0276	-0.0285	0.0178	0.0064
34	0.0035	0.0077	-0.0210	0.0501	0.2219	-2.8451	0.4574	-2.7738	0.2505	-2.8543	0.2318	-0.3020	0.1789	0.0231	-0.0031	0.0010
35	-0.0047	0.0023	-0.0089	-0.0137	0.0152	0.2218	-2.7738	0.4274	0.0112	0.2222	-0.2270	0.1705	-2.9108	0.2962	-0.0692	-0.0008
36	0.0042	-0.0181	0.0462	-0.0147	0.0526	-0.2643	0.1738	-2.7359	-0.0191	0.0282	0.0422	0.0342	0.2113	-0.1088	-0.0664	0.0247
37	-0.0001	0.0032	-0.0094	0.0035	-0.0245	0.0600	0.0311	0.2040	0.0107	-0.0285	-0.0287	0.0497	-0.1538	-0.1462	0.2539	0.1948
38		-0.0022	0.0072	-0.0007	0.0125	-0.0288	0.0240	-0.1117	-0.0088	0.0184	0.0033	0.0317	-0.1418	0.1784	-2.9361	-0.2766
39			0.0004			0.0034	-0.0093	0.0224		-0.0062	0.0038	-0.0227	0.0490	0.0450	0.1900	0.2098
40						0.0011	-0.0012	0.0087			-0.0020	0.0094	-0.0346	0.0531	-0.2501	0.0315
41								-0.0086				-0.0042	0.0145	-0.0250	0.0539	0.0510
42													-0.0009	0.0036	-0.0073	0.0234
43													-0.0009	0.0081	-0.0232	-0.0290
44														0.0021	-0.0044	0.0120
45															0.0029	-0.0112
46																
48	-0.0023	0.0017	0.0028	-0.0243	0.1854	-0.2702	0.2505	0.0112	0.5534	-3.0396	0.1902	0.0446	0.0624	-0.0327	0.0125	0.0041
49	0.0017	-0.0020	0.0071	-0.0090	-0.2801	0.1779	-2.8543	0.2222	-3.0396	0.5446	-2.9319	0.1867	-0.2920	0.0746	-0.0248	0.0248
50			-0.0018	0.0024	0.0568	0.0283	0.2318	-0.2270	0.1902	-2.9319	0.6084	-3.0428	0.2549	0.0728	-0.0424	-0.0551
51		-0.0002	0.0018	-0.0052	-0.0163	0.0572	-0.3020	0.1705	0.0446	0.1867	-3.0428	0.6866	-2.8648	-0.1072	0.0724	0.0243
52			0.0026	0.0047	-0.0181	0.0276	0.1789	-2.9108	0.0624	-0.2920	0.2549	-2.8648	0.6187	-2.7089	0.2540	

Table 5: Defect parameters of the Flower defect with atoms as numbered in Figure 22.

atom	0	1	2	16	32	33	34	35	48	49	50	51	52	53	54	55
53			-0.0012	-0.0012	0.0110	-0.0285	0.0231	0.2962	-0.0327	0.0746	0.0728	-0.1072	-2.7089	0.7384	-2.9420	0.1953
54			-0.0023		-0.0083	0.0178	-0.0031	-0.0692	0.0125	-0.0248	-0.0424	0.0724	0.2540	-2.9420	0.5878	-2.8063
55						-0.0069	0.0064	0.0010		0.0041	0.0258	-0.0551	0.0243	0.1953	-2.8063	0.5498
56							-0.0120	0.0259		0.0023	-0.0122	0.0228	-0.0311	0.0318	0.2088	-2.8828
57								-0.0111				-0.0043	0.0121	-0.0225	0.0232	0.2098
58								-0.0018				-0.0042	0.0065	-0.0123	0.0511	-0.2661
59													-0.0012	0.0029	-0.0187	0.0512
60														-0.0017	0.0081	-0.0226
61															-0.0008	0.0121
64				-0.0031	-0.0133	-0.0157	0.0439	-0.0007	0.3187	-0.2555	0.1902	0.0447	-0.0286	0.0158	-0.0054	-0.0202
65				0.0020	-0.0143	-0.0173	0.0018	0.0360	-0.2556	0.2831	-2.9321	0.1864	0.0280	-0.0472	0.0186	0.0076
66					0.0041	0.0042	-0.0079	-0.0124	0.0440	0.0018	0.2318	-0.3023	0.0738	-0.0491	0.0210	-0.0274
67					-0.0049	0.0032	-0.0123	-0.0473	-0.0008	0.0360	-0.2268	0.1708	0.0701	0.0428	-0.0428	0.0742
68					0.0080	-0.0276	0.0736	0.0701	-0.0285	0.0279	0.2550	-2.8645	0.0653	-0.0222	0.0783	-0.2788
69					-0.0064	0.0223	-0.0488	0.0422	0.0158	-0.0472	0.0727	-0.1069	-0.0210	-2.8612	0.1905	0.0315
70							-0.0116	0.0269	-0.0003	-0.0021	0.0033	0.0317	-0.0624	0.0450	0.0523	0.2090
71						-0.0104	0.0209	-0.0426	-0.0054	0.0186	-0.0423	0.0720	0.0781	0.1898	-0.2476	-2.8789
72						-0.0016	0.0077	-0.0275		-0.0201	0.0247	-0.0549	0.0742	-0.2787	0.2092	0.2112
73								0.0116			-0.0122	0.0227	-0.0287	0.0514	0.0228	-0.0228
74												-0.0043	0.0022	0.0034	0.0086	-0.0122
75														-0.0058	0.0029	-0.0124
76														0.0023	0.0030	0.0065
77															-0.0012	-0.0016
78																
80					-0.0002	0.0006	0.0041	-0.0050	-0.0132	-0.0143	0.0568	-0.0163	0.0081	-0.0064	-0.0104	-0.0016
81					0.0006	-0.0003	0.0042	0.0032	-0.0156	-0.0174	0.0283	0.0572	-0.0277	0.0223	0.0010	
82							-0.0023	0.0055	0.0038	0.0096	-0.0258	-0.0116	-0.0017	0.0027	-0.0010	-0.0122
83							0.0016	-0.0073	-0.0008	0.0025	-0.0078	-0.0269	0.0179	-0.0082	0.0086	0.0260
84						0.0003	0.0017	0.0231	0.0003	-0.0149	0.0421	0.0341	-0.0536	0.0206	-0.0350	-0.0304
85							-0.0027	-0.0084		0.0105	-0.0287	0.0496	0.0055	0.0512	0.0098	0.0225
86											0.0102	-0.0253	0.0050	-0.0243	-0.0049	-0.0284
87											0.0004	0.0049	-0.0025	0.0228	-0.0062	0.0501
88								-0.0077			0.0038	-0.0227	0.0221	-0.0384	-0.0236	0.0229
89								0.0030			-0.0020	0.0095	-0.0044	-0.0071	-0.0011	0.0121
90														-0.0009		-0.0041
91															-0.0011	0.0064
92																-0.0013
93																
96											0.0024	-0.0053	0.0011			
97										0.0021	0.0082	0.0040				
98									-0.0031	-0.0028	-0.0018	0.0018				
99									0.0010		0.0009	-0.0033				
100										-0.0011	0.0040	0.0096	-0.0044	-0.0073	-0.0022	0.0023
101											-0.0092	0.0115	-0.0003	0.0050	0.0028	-0.0121
104												0.0005		-0.0079		0.0120
105																-0.0107

Table 6: Second part of the defect parameters of the Flower defect with atoms as numbered in Figure 22.

A.4 Silicon interstitial

	0	1	2	3	8	9	10	11	16	17	20
0	0.2561	-2.9520	0.2426	0.0231	0.2351	-0.2891	0.0543	-0.0101	-0.0154	-0.0152	0.0026
1	-2.9520	0.2540	-2.9855	0.2241	-0.2806	0.1978	0.0255	0.0583	-0.0122	-0.0183	-0.0225
2	0.2426	-2.9855	0.2284	-2.9380	0.2578	-2.9593	0.2568	-0.2928	0.0496	0.0041	0.0534
3	0.0231	0.2241	-2.9380	0.1929	0.0265	0.2063	-0.2493	0.0924	-0.0001	0.0310	0.0743
4	0.0447	-0.2758	0.2535	-3.0779	-0.0291	0.0286	0.0511	0.0614	0.0003	-0.0170	-0.0420
5	-0.0179	0.0565	0.0055	0.2755	0.0108	-0.0224	-0.0161	0.0452	0.0025	0.0036	-0.0101
6	0.0022	-0.0132	0.0509	-0.2675	0.0005	-0.0010	-0.0318	0.0300	-0.0019	0.0089	0.0828
7	-0.0002	0.0033	-0.0167	0.0450	0.0011	-0.0013	0.0135	-0.0265		-0.0040	-0.0110
8	0.2351	-0.2806	0.2578	0.0265	0.2255	-3.0406	0.2027	0.0511	0.2659	-0.2704	-0.0377
9	-0.2891	0.1978	-2.9593	0.2063	-3.0406	0.1956	-2.9949	0.1084	-0.2661	0.2634	0.0646
10	0.0543	0.0255	0.2568	-0.2493	0.2027	-2.9949	-0.0175	-2.5336	0.1553	-2.8061	0.1829
11	-0.0101	0.0583	-0.2928	0.0924	0.0511	0.1084	-2.5336	-2.0806	0.0375	0.2214	-2.8628
12	-0.0223	0.0139	0.2743	-3.0251	0.0497	-0.2449	0.1768	0.2419	-0.0376	0.0559	0.1730
13	0.0089	-0.0137	-0.0009	0.2627	-0.0165	0.0312	0.0465	-0.1788	0.0100	-0.0272	-0.4108
14	-0.0047	0.0080	-0.0209	0.0199	-0.0031	0.0102	-0.0039	0.0301	-0.0066	0.0196	0.1816
15		-0.0034	0.0096	-0.0251	0.0013	-0.0015	-0.0063	0.0375	0.0035	-0.0095	0.0685
16	-0.0154	-0.0122	0.0496	-0.0001	0.2659	-0.2661	0.1553	0.2214	0.2023	-2.9950	0.0869
17	-0.0152	-0.0183	0.0041	0.0310	-0.2704	0.2634	-2.8061	-0.1797	-2.9950	0.2019	-0.4208
18	0.0023	0.0095	-0.0206	0.0089	0.0426	0.0130	-0.1787	0.0351	0.1506	-2.8076	0.1776
19	-0.0015	-0.0006	-0.0017	-0.0540	-0.0023	0.0286	0.1829	-2.8628	0.0381	0.2249	-2.8680
20	0.0026	-0.0225	0.0534	0.0743	-0.0377	0.0646	0.0932	0.0127	0.0869	-0.4208	1.8861
21	0.0036	0.0015	-0.0036	0.0295	0.0156	-0.0515	-0.0786	0.0899	-0.0204	0.0463	-2.8315
22			-0.0070	-0.0066	-0.0049	0.0253	0.0259	-0.0522	-0.0063	0.0190	0.1760
23			0.0043	-0.0005		-0.0056			0.0032	-0.0090	0.0669
24											
25	0.0019	-0.0033	0.0079	-0.0003	-0.0125	-0.0198	0.0126	0.0291	-0.2650	0.2648	0.0680
26			-0.0029	0.0043	0.0044	0.0078	-0.0206	-0.0028	0.0479	0.0046	0.0550
27			0.0045	-0.0053	-0.0047	-0.0009	0.0102	-0.0528	0.0013	0.0290	0.0697
28		0.0049	-0.0083	0.0259	0.0017	-0.0046	-0.0066	0.0915	-0.0376	0.0545	0.1736
29			0.0003	-0.0095	0.0036	-0.0091	0.0190	0.0490	0.0101	-0.0281	-0.4187
30				0.0034		0.0033	-0.0055	-0.0217	-0.0019	0.0095	0.0871
31							0.0064	-0.0009		-0.0042	-0.0113

Table 7: Defect parameters of the Silicon interstitial with atoms as numbered in Figure 21.

References

[1] K. S. Novoselov, A. K. Geim et. all. *Electric field effect in atomically thin carbon films.*. Science, 306:666, 2004.

[2] A. Castro Neto, F.Guinea et. all. *The electronic properties of graphene* RevMod-Phys. 81, 109, 2009.

[3] W. Cal, A. Moore, et. all. *Thermal Transport in Suspended and Supported Mono-layer Graphene Grwon by Chemical Vapor Deposition* Nano Lett, 10(5), pp 1645-1651, 2010.

[4] A.K. Sood, I. Lund et. all. *Review of graphene technology and its applications for electronic devices* in Graphene - New Trends and Developents, Intech, 2015.

[5] W. Han *Perspectives for spintronics in 2D materials* APL Mater. 4, 032401, 2016.

[6] C. Stampfer, E. Schurtenberger et. all. *Tunable graphene single electron transistor* Nano Lett., 8(8), pp 2378-2383, 2008.

[7] F. Banhart, J. Kotakoski and V. Krasheninnikov *Structural Defects in Graphene* ACS Nano, 5 (1), pp 26-41, 201, 2011.

[8] J. Robinson, J. Burgess et. all. *Properties of Fluorinated Graphene Films* Nano Lett. 10, 3001-3005, 2010.

[9] D. Teweldebrhan and A. Balandin *Modification of graphene due to electron-beam irradiation* Appl. Phys. Lett. 94, 013101, 2009.

[10] V. Pereira, J. Lopes dos Santos, et all. *Modeling disorder in graphene* Phys. Rev. B 77 115109, 2008.

[11] V. Pereira, J. Lopes dos Santos et. all. *Modeling disorder in graphene* Phys. Rev. B 77, 115109, 2008.

[12] E. Cockayne, G. M. Rutter et.all. *Grain Boundary Loops in Graphene* Phys. Rev. B 83, 195425, 2011

[13] H. Park, V. Skakalova et.all. *Growth and properties of chemical modified graphene* Phys. Status Solidi B 247, 2915, 2010.

[14] J. Wang, G. Zhang et.all. *Electronic transport through graphene nanoribbons with Stone-Wales reconstruction at edges and interfaces* Reviewing available via: DOI: 10.5772/61316, 2015.

[15] F. Libisch, S. Rotter, J. Burgdörfer *Disorder scattering in graphene nanoribbons* Phys. Status Solidi B 248, 2598-2603, 2011.

[16] J. Kotakoskim, C. Mangler et. all. *Imaging atomic-level random walk of a point defect in graphene* Nat. Comm. 10.1038/ncomms4991, 2014.

[17] F Eder, J. Kotakoski et. all. *Probing from Both Sides: Respaheing the Graphene Landscape via Face-to-Face Dual-Probe Microscopy* Nano Lett. 13 (5), pp 1934-1940, 2013.

[18] P. Hohenberg, W.Kohn *Inhomogeneous Electron Gas* Phys. Rev. 136, B864 - Nov. 1964.

[19] T. Chachiyo *Simple and accurate uniform electron gas correlation energy for the full range of densities.* Chem. Phys. 145, 021101, 2016.

[20] R.Parr, Y. Weito *Density-Functional Theory of Atoms and Molecules* International series of monographs on Chemistry. Oxford University Press, 1994.

[21] G. Wannier *The Structure of Electronic Excitation Levels in Insulating Crystals* Phys.Rev. 52, 191, 1937.

[22] N. Marzari, A. Mostofi et.all. *Maximally localized Wannier functions: Theory and applications* Rev. Mod. Phys. 84, 1419, 2012.

[23] N. Mazari, D. Vanderbilt *Maximally localized generalized Wannier functions for composite energy bands* Phys. Rev.B 56, 12847, 1997.

[24] I. Souza, N. Mazari et. all. *Maximally localized Wannier functions for entangled energy bands* Phys. Rev. B 65, 035109, 2001.

[25] S. Datta *Electronic Transport in Mesoscopic Systems* Cambridge University Press, 1995.

[26] F. Libisch *Electronic structure and transport in mesoscopic devices* PHD thesis, TU-Vienna, 2008.

[27] D. Fisher, P. Lee *Relation between conductivity and transmission matrix* Phys. Rev. B, Vol. 23, 12, 1981.

[28] F. J. Dyson *The S Matrix in Quantum Electrodynamics* Phys. Rev. 75 1736, 1949.

[29] S. Rotter *A Modular Recursive Green's Function Method for Quantum Transport.* Diploma thesis, TU-Vienna, 1999.

[30] P. R. Wallace *The Bandtheory of Graphite* Phys. Rev. 71, 622, 1947.

[31] R. Reiter *Advanced tight-binding descriptions of graphene* Diploma Thesis, TU Vienna, 2014.

[32] K. Bolotin, K. Sikes et. all. *Ultrahigh electron mobility in suspended graphene* Solid State Communications 146,9-10, pp 351-355, 2008.

[33] K. Levenberg *A Method for the Solution of Certain Non-Linear Problems in Least Squares* Quarterly of Applied Mathematics. 2: 164-168, 1944.

[34] D. Marquardt *An Algorithm for Least-Squares Estimation of Nonlinear Parameters* SIAM Journal on Applied Mathematics. 11 (2): 431-441, 1963.

[35] G. Kresse, J. Hafner et.all. *Ab initio molecular dynamics for liquid metals.* Phys. Rev. B, 47:558, 1993.

[36] G. Kresse, J. Hafner et. all. *Ab initio molecular-dynamics simulation of the liquid-metal-amorphous-semiconductor transition in germanium.* Phys. Rev. B, 49:14251, 1994.

[37] G. Kresse, J. Furthmüller et. all. *Efficiency of ab-initio total energy calculations for metals and semiconductors using a plane-wave basis set.* Comput. Mat. Sci., 6:15, 1996.

[38] G. Kresse and J. Furthmüller. *Efficient iterative schemes for ab initio total-energy calculations using a plane-wave basis set.* Phys. Rev. B, 54:11169, 1996.

[39] A. A. Mostofi, J. R. Yates et.all. *Wannier90: A Tool for Obtaining Maximally-Localised Wannier Functions* Comput. Phys. Commun. 178, 685, 2008.

[40] E. McCann, K. Kechedzhi et.all. *Weak-Localization Magnetoresistance and Valley Symmetry in Graphene* Phys. Rev. Lett. 97, 146805, 2006.

[41] D. Basko *Effect of anisotropic band curvature on carrier multiplication in graphene* Phys. Rev. B 87, 165437, 2013.

[42] L. Linhart *Scattering at lattice defects in graphene* Projectwork, TU-Vienna, institute of theoretical physics, 2016.

[43] F. Libisch, A. Kliman et.all. *Transport through graphene nanoribbons: Suppresion of transverse quantization by symmetry breaking* Phys. Status Solidi B, 1-7, 2016.

[44] S. Reich, J. Maultzsch et. all. *Tight-binding description of graphene.* PRB, 66:035412, 2002.

[45] V. Pereira, R. Ribeiro et. all. *Optical Properties of Strained Graphene* DOI: 10.1209/0295-5075/92/67001, 2010.

[46] F. Schwabl *Quantenmechanik, eine Einführung* Springer Berlin, ISBN 978-3-540-73674-5, 7. Auflage.

[47] D. M. Basko *Effect of anisotropic band curvature on carrier multiplication in graphene* PhysRevB.87.165437.

[48] A. Grüneis, C. Attaccalite et. all. *Tight-binding description of the quasiparticle dispersion of graphite and few-layer graphene* PhysRevB.78.205425.

[49] L.A. Chizhova, F.Libisch et. all *High-harmonic generation in graphene: interband response and the harmonic cut-off* Phys.Rev.B.94.075412, 2016.